ARL 70-0074
APRIL 1970

Aerospace Research Laboratories

A NUMERICAL MODEL FOR A COMBUSTION-DRIVEN SPHERICAL IMPLOSION WAVE

A. ELSENAAR
UNIVERSITY OF TORONTO
INSTITUTE FOR AEROSPACE STUDIES
TORONTO, CANADA

Contract No. AF33(615)-5313
Project No. 7065

OFFICE OF AEROSPACE RESEARCH
United States Air Force

92

NOTICES

When Government drawings, specifications, or other data are used for any purpose other than in connection with a definitely related Government procurement operation, the United States Government thereby incurs no responsibility nor any obligation whatsoever; and the fact that the Government may have formulated, furnished, or in any way supplied the said drawings, specifications, or other data, is not to be regarded by implication or otherwise as in any manner licensing the holder or any other person or corporation, or conveying any rights or permission to manufacture, use, or sell any patented invention that may in any way be related thereto.

Agencies of the Department of Defense, qualified contractors and other government agencies may obtain copies from the

Defense Documentation Center
Cameron Station
Alexandria, Virginia 22314

This document has been released to the

\- - - - - - - - -

CLEARINGHOUSE
U.S. Department of Commerce
Springfield, Virginia 22151

for sale to the public.

Copies of ARL Technical Documentary Reports should not be returned to Aerospace Research Laboratories unless return is required by security considerations, contractual obligations or notices on a specified document.

300 - June 1970 - CO455 - 122-2673

BLANK PAGE

ARL 70-0074

A NUMERICAL MODEL FOR A COMBUSTION-DRIVEN SPHERICAL IMPLOSION WAVE

A. ELSENAAR
INSTITUTE FOR AEROSPACE STUDIES
UNIVERSITY OF TORONTO
TORONTO, CANADA

APRIL 1970

Contract No. AF33(615)-5313
Project No. 7065

AEROSPACE RESEARCH LABORATORIES
OFFICE OF AEROSPACE RESEARCH
UNITED STATES AIR FORCE
WRIGHT-PATTERSON AIR FORCE BASE, OHIO

FOREWORD

This interim report was prepared at the Institute for Aerospace Studies, University of Toronto, Toronto, Canada under Contract No. AF 33(615)-5313 for the Aerospace Research Laboratories, Office of Aerospace Research, United States Air Force. This research was accomplished under the technical cognizance of Mr. Kenneth F. Stetson of the Fluid Dynamics Facilities Research Laboratory.

I should like to thank Dr. G. N. Patterson for providing the opportunity to study at the Institute for Aerospace Studies.

I should also like to thank Dr. I. I. Glass for giving me the opportunity and the stimulus for this work.

I wish to acknowledge the discussions, critical comments and helpful suggestions given by my colleagues, in particular W. O. Graf, Dr. A. K. Macpherson, Jean-Claude Poinsot and Dr. D. E. Roberts.

The computer time provided by the Institute of Computer Science of the University of Toronto, and the help of T. LaBrash are acknowledged with thanks.

The research reported herein was partially supported by the National Research Council of Canada.

ABSTRACT

A study is made of a combustion-driven spherical implosion wave inside a hemispherical cavity, using a finite difference method to integrate the one-dimensional Lagrangian gasdynamic equations, combined with an artificial pressure term to represent the shocks and a realistic equation of state for the stoichiometric hydrogen-oxygen mixture. The application of this technique is studied in some detail.

Special care is given to the flow close to the origin in order to predict the performance of the UTIAS Implosion-Driven Hypervelocity Launcher. Experimental results on average temperatures at the origin and initial projectile velocities compare favorably with the results of the numerical calculations.

The numerical results are also compared with some analytical solutions for the implosion wave and the subsequent reflection from the centre. The pressure ratio of the imploding wave compares favorably with the analytical expressions. The increase in pressure due to the reflection, however, is an order of magnitude lower than the self-similar, strong-shock solution indicates and the pressure drop is much steeper.

A parametric study of explosive-driven implosion waves is made based on some analytical expressions and an impulsive loading of the projectile. The result of this indicates that a driver gas with a low γ and a low sound speed is preferable to obtain a long duration of the pressure pulse for an implosion-driven hypervelocity launcher. The use of air as a driver gas instead of the combustion products of a hydrogen-oxygen mixture may improve the performance by a factor of 2, providing the driving shell of explosive could be initiated instantly and simultaneously by some other techniques such as using light-sensitive explosives.

TABLE OF CONTENTS

LIST OF ILLUSTRATIONS

(Illustrations, cont'd)

NOTATION

A	barrel area
a,b	constants in stability conditions (Eq. 3.5)
C	constant in artificial viscosity term
c	sound speed
c_o	sound speed in front of implosion wave
c^*	characteristic sound speed for converging blast (Eq. 5.3)
E	energy in finite difference equations
E_o	explosive energy
F	burn factor in finite difference equations
$f(z)$	function in W-C-C-rule (Appendix C)
j	subscript for space dependence, finite difference equations
M	Mach number; molecular weight
M_b	shock Mach number at the radius of the barrel
M_s	shock Mach number
m_j	mass of zone j in finite difference equations
m	projectile mass
N	total number of zones in finite difference equations
n	m_j/m_{j-1}, mass ratio in finite difference equations; subscript for time dependence, finite difference equations; similarity exponent for strong shock solution (Appendix D)
P	pressure in finite difference equations
p	pressure
p_b	absolute pressure at the barrel radius for imploding shock
p_i	initial pressure in chamber
p_o	pressure in front of implosive wave

P_D	pressure behind detonation wave
P_S	pressure behind imploding shock
Q	artificial viscosity pressure, finite difference equations
R	Eulerian co-ordinate, finite difference equations
R_b	radius of the barrel
R_c	radius of the chamber
$\mathcal{R}$	universal gas constant
r	distance from the origin
r_D	radius of detonation front
r_S	radius of shock front
r^*	r/R_c, distance with respect to chamber radius
r^*_s	r_S/R_c, position of the shock with respect to chamber radius
S	entropy
t	time
t^*	characteristic time for imploding blast waves (Eq. 5.1)
t^{**}	characteristic time for implosion wave (Eq. 5.11)
Δt	time step in finite difference calculations
U	flow velocity in finite difference equations
u	flow velocity
u_S	shock velocity
V	specific volume finite difference equations
V_{CJ}	Chapman-Jouguet volume
v	projectile velocity
x	Lagrangian co-ordinate in finite difference equations
Δx	zone width in finite difference equations
x_S	position of shock for converging blast waves (Eq. 5.2)

$\dot{x}_s$	shock velocity for converging blast waves (Eq. 5.4)
z	pressure ratio in W-C-C-rule (Appendix C)
z_b	pressure ratio at the barrel radius for imploding shock
α	geometrical constant; $\alpha = 0$ planar, $\alpha = 1$, cylindrical $\alpha = 2$, spherical (Appendix D)
γ	isentropic index
δ	similarity exponent for pressure in the strong shock solution (Appendix D)
η	r/r_D or r/r_s, distance with respect to the detonation front or shock
μ,ν	non-dimensional variables (Appendix D)
ξ	variable relating r and t in similarity transformation (Appendix D)
π	p/p_D, pressure ratio behind the detonation wave
ρ	density
ρ_o	initial density in the chamber
φ	u/u_s, velocity with respect to the shock velocity
χ	characteristic impulse(Eq. 5.12)
χ_2,χ_3	non-dimensional variables (Appendix D)

BLANK PAGE

1. INTRODUCTION

The interest in spherical implosion waves is related to the UTIAS Implosion-Driven Hypervelocity Launcher. The principle of this device, to accelerate small projectiles to velocities of 30,000 ft/sec and higher, was first suggested by Dr. I. I. Glass, in 1959 (Ref.1). The high pressure, high temperature region behind a reflected spherical implosion wave is applied to drive a projectile down a barrel. In its simplest mode of operation an implosion wave is formed after reflection from the outer wall of a hemispherical cavity of a spherical detonation wave in a $2H_2 + O_2$ gas mixture. To generate much stronger implosion waves a layer of explosive at the outer wall of the cavity is initiated by the detonation wave. This is illustrated in Fig.1. A more complete description of this device can be found elsewhere (Ref.2).

In this report we are mainly concerned with a theoretical analysis of the Launcher to show some of the basic properties of implosion waves and to predict the Launcher performance. Two different approaches are possible. One can isolate the different stages in the launching process as there are the outgoing spherical detonation, the reflection from the wall or initiation of a layer of explosive, the implosion wave, and finally the reflection of the implosion wave at the centre. If we are able to match these different solutions a complete analytical description of the wave process can be obtained. The most serious limitation to this approach is that as yet not very much is known about the propagation and reflection of spherical implosion waves of moderate strength. Also, when more than one shock is generated at the explosive interface, an analytical solution becomes increasingly complex.

A more general approach is obtained by intergrating the equations for hydrodynamic motion in a finite difference form. The presence of shocks in the flow field represents a serious difficulty, since they appear as boundaries that cannot be known in advance. The use of an artificial pressure term as first proposed by von Neumann and Richtmyer (Ref.3) removes this limitation and resulted in a widely used technique for the calculation of nonstationary flow and impact phenomena. Based on this approach several computer programs were developed in the past at UTIAS. This technique seemed at first quite attractive. The finite difference equations are relatively simple. There are no limitations in the equation of state that can be used and, given enough computer time, results are readily obtained. However, one has to be very critical in interpreting the results. The introduction of an artificial pressure in the flow field can generate disturbances that can completely alter the results. In fact, this technique gives only an approximation of the exact solution and in each particular case the validity of the approximation has to be proven. This in itself is not easy since in most cases exact solutions are not available. One must often rely on experience and common sense. A minimum requirement is that the solution has to converge for decreasing stepsize.

Unfortunately, some of these limitation are not realized to the full extent in developing the codes describing the launching process. The comparison with experimental results is poor and more important, the results of the calculations appear to be highly dependent on the initial zoning scheme.

A more critical study of the applicability and limitations of the finite difference technique in spherical geometry was therefore necessary and is presented in this report. Only the problem of a spherical implosion wave, formed after reflection of a detonation wave in a spherical cavity was considered in detail. The results were tested as to convergence and where possible they were compared with analytical solutions. The results are also compared with the available experimental data for this particular case. Finally, a parametric study of the launcher, operating in the explosive mode was made.

2. THE ARTIFICIAL VISCOSITY TECHNIQUE

2.1 General Description

Hydrodynamic flow in one dimension is governed by the equations of motion of mass, momentum and energy and an additional equation of state. The equations of motion can be written in an Eulerian or a Lagrangian form, whatever is the most convenient for the solution of a particular problem.

A set of equations has to be completed with a set of boundary conditions as there are the initial values, the values at the physical boundaries and the shock wave relations. This last condition causes the major difficulty for integrating the system of equations, because the shocks are a consequence of the flow itself and neither the properties at the shock front nor its position can be known in advance.

To overcome this difficulty von Neumann and Richtmyer proposed the method of artificial viscosity for the use in finite difference equations (Ref.3). The pressure in the conservation equations are replaced by a form (P + Q) where, Q is given by the expression:

$$\left.\begin{aligned} Q &= -\frac{(\rho_o C\Delta x)^2}{V}\frac{\partial V}{\partial t}\left|\frac{\partial V}{\partial t}\right| \quad \text{if } \frac{\partial V}{\partial t} < 0 \\ Q &= 0 \qquad\qquad\qquad\qquad\quad \text{if } \frac{\partial V}{\partial t} \geq 0 \end{aligned}\right\} \qquad (2.1a)$$

or by

$$\left.\begin{aligned} Q &= -\frac{(C\,\Delta x)^2}{V}\frac{\partial U}{\partial x}\left|\frac{\partial U}{\partial x}\right| \quad \text{if } \frac{\partial U}{\partial x} < 0 \\ Q &= 0 \qquad\qquad\qquad\qquad\quad \text{if } \frac{\partial U}{\partial x} \geq 0 \end{aligned}\right\} \qquad (2.1b)$$

Herein C is a constant that determines the number of zones over which the shock is spread; C is of the order of unity.

The equations of motion can then be written as:

$$\rho_o \frac{\partial V}{\partial t} = \frac{\partial U}{\partial x} \qquad (2.2a)$$

$$\rho_o \frac{\partial U}{\partial t} = - \frac{\partial (P + Q)}{\partial x} \qquad (2.2b)$$

$$\frac{\partial E}{\partial t} + (P + Q) \frac{\partial V}{\partial t} = 0 \qquad (2.2c)$$

$$E = E (P, V) \qquad (2.3)$$

in Lagrangian co-ordinates.

The effect of Q is qualitatively the same as the effect of viscosity as can be seen from (Eq. 2.1b). Quantitatively, Q is orders of magnitude greater. Where a realistic viscosity should spread the shock over a number of mean free path lengths, the artificial viscosity will spread the shock over a few zones in the finite difference scheme. A real viscosity does not influence the Rankine-Hugoniot relations as long as the viscosity can be neglected outside the shock region. The same applies, although with more limitations, to an artificial-viscosity shock. Outside the shock Q is small compared with its value inside the shock and it can be proven for a planar steady-state shock that the Rankine-Hugoniot relations are still obeyed. Outside the shock region Eqs. (2.2) reduce to the normal Lagrangian equations. A typical example of a planar steady state shock is shown in Fig.2, where a shock is generated by a piston moving with a constant velocity in an uniform channel. In this case the agreement with the exact solution is very good. The strength of the shock appeared to be independent of the number of zones and the constant C. However, it illustrates graphically how the shock wave is spread and the difficulty is geometrically positioning the shock front.

In the next sections we will study two cases where the flow is more complicated than for a planar, steady-state shock. As we will see, deviations from the exact solution occur, but they can be reduced if properly treated.

2.2 Reflection of a Planar Wave from a Wall

As finally we are interested in the reflection process of a spherical converging wave, it might be of interest to study first the reflection of a plane wave from a wall. A program is set up to describe the motion of a strong shock, generated by a piston moving with a constant velocity of 2.5 mm/μsec (shock Mach number 9.5) in a channel with constant cross-section. At the end of the channel the shock reflects from the wall and the resulting flow field is analyzed. Equations 2.2 combined with the equation of state for a perfect gas and $\gamma = 1.4$ are applicable to this problem. An artificial viscosity similar to Eq. 2.1b with C =2 is used. Figure 2 shows the pressure profile when the piston has moved halfway down the channel. The pressure agrees with the exact value for 25 and 50 zones, and the same applies to density and shock speed. Figure 3 shows the pressure at the end of the channel as function of time. The pressure rises slowly because of the finite width of the shock, overshoots its theoretical value by about 10% and converges finally to its ideal value. The density (Fig.4) also rises slowly, but remains constants at a value 40% lower than the theory predicts. This phenomenon is more clearly indicated in Fig.5, where the density profile behind the reflected shock is shown. There are serious disturbances near the wall

extending over about 12 zones. They remain unchanged in time. Therefore, the artificial viscosity technique fails to describe the reflection process properly. This example also shows an important feature of this technique. Large pressure differences between zones decay in time, in the planar case, but density differences are uneffected. This follows from Eq. 2.2. If the pressure in two adjacent zones is different, the interface will be accelerated till the pressure difference is eliminated. When the pressures are the same, but the density is different, there is no correcting mechanism. For the steady-state shock the correct pressure and density is obtained behind the shock. But in the case of a reflection a disturbance is generated. The reflection process is the analog to the head-on collision of two shock waves of equal strength, and related to the refraction problem where a shock is partly reflected and partly transmitted when it moves into a different medium. For this case, a similar experience is reported in Ref.4. Fox (Ref.5) also mentions these cases and states that the disturbances are caused by an incorrect representation of the entropy change, given by:

$$\frac{dS}{dV} = -\mathcal{R}\,\frac{Q}{P.V.} \qquad (2.4)$$

Only when Q has the correct value with respect to P and V is a good approximation obtained. The presence of a rigid boundary or a sudden change in density locally alters the action of Q. A local change in Q may alter the results favourably. This is also shown in Figs. 3,4 and 5, where a value of C = 2 is taken through the entire flow field, but is reduced close to the wall, (C = 1.5 and C = 1.0 for the last two zones respectively). The pressure overshoot at the wall and the density differences are greatly reduced and smaller than 5%. It must be noted however that the reduced values of Q are obtained by trial and error. The correct value is likely to be dependent on the shock Mach number, the zone size and the compressibility of the medium. No general rule for this correction can be given as yet.

2.3 The Case of an Imploding Spherical Piston

To what extent can the artificial viscosity technique be used in other than planar geometries? The hydrodynamic equations, .2.2, still hold but it is not clear which form of the artificial viscosity must be used. Locally, a spherical or cylindrical shock wave can still be regarded as a planar wave. The Rankine-Hugoniot relations are still valid and hence the artificial viscosity will represent a true shock, but only when the shock thickness is small compared with the local area change. Away from the shock the condition $Q \ll P$ must be satisfied. In other than planar geometries density or velocity gradients can be present outside the shock region. The artificial viscosity Q, will have in those regions a finite value, although small compared with its value inside the shock. But the action of Q is cumulative, as can be seen from Eq. 2.4, and it will influence the flow field after a large number of cycles. Latter (Ref.6) obtained an analytical solution for a spherical shock using an artificial viscosity similar to Eq. 2.1b. His conclusion is that the entire flow field depends upon the artificial viscosity term. Brode (Ref.7) mentions that if the spread of the shock is limited to a small region the effect on the remainder of the flow field will be very small. In any case, it is clear that the use of this technique is more restricted in other than planar geometries.

The technique has been used in other geometries. Brode (Ref.7)

treated a spherical blast wave and his results compare well with the exact solution when the shock is still strong. Payne (Ref. 8) applied a Lax-Wendroff scheme in Eulerian co-ordinates for the calculation of a cylindrical converging shock wave. His results also compare favourably with the available theory. He does not mention any effect of the artificial diffusion terms.

An additional problem in converging or diverging geometries is the choice of the initial zoning scheme. Since the length of a zone is not proportional to its mass a change in zone size or zone mass has to be accepted. If the zones are too long they are not acceptable as are great changes in mass since they cause severe oscillations. A possible alternative is the use of a great number of zones. (Payne used 50 to 100 zones). Brode makes use of a program where the flow-field is rezoned during the calculations. (Ref.9). The program then becomes very complicated.

To study the use of the artificial viscosity technique in a spherical converging geometry a program is set up to describe the motion of a perfect gas in front of a spherical imploding piston. Piston velocity and the state of the gas at rest are the same as in the case discussed in Sec.2.2. The initial zoning is obtained by allowing for a decrease in mass in such a way that the ratio between two adjacent masses is constant and defined by:

$$\text{mass ratio} \quad n = \frac{m_j}{m_{j-1}} \qquad (2.5)$$

with $1 < n < 0.85$ depending on the total number of zones N. This scheme is adopted to alter independently the total number of zones and the number of zones in the origin region (see Sec.3.3). Three different cases are investigated:

$$N = 25 \text{ and } n = 0.85$$

$$N = 50 \text{ and } n = 0.90$$

$$N = 75 \text{ and } n = 0.95$$

Figure 6 shows the pressure profile when the piston has moved half way into the chamber. The expressions for the artificial viscosity, Eqs. 2.1a and 2.1b, are compared for 25 zones with C = 2. As can be seen an artificial viscosity term based on the velocity gradient dU/dx gives a much lower value for the pressure than a Q-term based on the rate of compression, dV/dt. The reason is that in the latter case the action of Q is not restricted to the shock and will increase the pressure in the entire flow field, since the gas behind the shock is compressed ($dV/dt < 0$) as the flow moves into a converging geometry. A Q-term based on the velocity gradient dU/dx however acts only inside the shock since the velocity increases from the piston in the direction of the shock ($dU/dx > 0$). For this reason an artificial viscosity based on a velocity gradient is adopted throughout the calculations. Figure 7 shows the pressure profiles for 25,50 and 75 zones with C = 2.5. The results are, as can be seen, strongly affected by the number of zones, although the artificial viscosity is now only restricted to the shock region. For a large number of zones the shock is spread over a much smaller portion of the flow field than for a small number of zones. The disturbances introduced by the Q-term will then also be smaller for a large number of zones.

A decrease in the constant C has a similar effect. This is illustrated in Fig. 8, where C = 1.5. The difference between 50 and 75 zones is now smaller than 5%. A smaller value of C, however, increases the oscillations behind the shock as can be seen for N = 25, in the same figure. The results seem to converge to a lower bound for $N \geq 50$ and $C \leq 1.5$. Based on this experience a value C = 1 is used in the final calculations.

3. A NUMERICAL MODEL FOR AN IMPLOSION IN A SPHERE

3.1 Review of the work done at UTIAS

The first calculations on implosion waves in relation to the UTIAS Hypervelocity Launcher were performed by Brode and reported by Flagg (Ref.10). These calculations were made with a very general code, based on the artificial viscosity technique and describing nonstationary flow for a great number of different geometries. Only the detonation and subsequent implosion in a closed spherical chamber were considered. The details of this numerical program are unfortunately not reported. Flagg used these results (for three different cases, two of them with an explosive charge) to obtain some information on the behaviour of implosion waves and to compare these results with the available theory, a rather difficult task since the output of the numerical programs was very limited. The work reported here is similar to this but restricted to the case of a stoichiometric mixture of hydrogen and oxygen without explosive PETN. A more detailed output in the present calculations made a better comparison possible.

In order to predict projectile velocities for the UTIAS Implosion-Driven Hypervelocity Launcher there was a need to develop a code that could describe the projectile motion as a result of the wave dynamics inside the chamber. A method was adopted that would describe simultaneously the chamber and barrel processes. The numerical difficulty is to connect the finite-difference equations for a spherical geometry in the chamber with those for a planar geometry inside the barrel. Piacesi and Sevray (Ref.11) worked independently of each other on this problem. Their results differ appreciabl , the difference being caused by a different treatment of the transition at the origin between chamber and barrel. The programs as used by Flagg and Mitchell (Ref.12) for an optimization study, and by Poinssot (Ref.13) to investigate the application of the launcher chamber as a driver for a shock tube, are not fundamentally different from the set-up by Sevray. Only minor changes in initial zoning and the chamber-barrel transition were made, however, the results of these programs were often quite different. (see Appendix B of Ref.12).

Differences in the initial zoning scheme are not believed to be very critical as long as the mass of the zones varies smoothly and a sufficient number of zones is used. Sevray divided the chamber into three regions and sub-divided each of them into a number of zones with constant mass. Poinssot used the same scheme with 7 different regions that reduced the size of the zones near the origin. Flagg and Mitchell, not satisfied with the appreciable change in mass between two regions, adopted a more gradual change in zone mass. Both Sevray and Flagg and Mitchell used 20 zones in the gas region, a rather small number in view of the discussion in Sec.2.3, where a minimum number of 50 zones is recommended. The zone at the origin was also quite big, 0.2 of the chamber radius for Sevray, 0.1 for Flagg and Mitchell, as

compared with a barrel radius of 0.04.

The problem of transition between spherical and planar geometry is much more difficult to evaluate. In Lagrangian co-ordinates the zones move with the flow velocity towards the origin and follow the projectile inside the barrel. The shape of the zones changes then from a spherical geometry inside the chamber a planar geometry in the barrel as shown in Fig.9. The approach of Sevray was to program a gradual transition as indicated in Fig.9. An assumption had to be made regarding the shape of the zones in the transition region. They assumed that a spherical zone inside the chamber collapses till the radius of the barrel and changes then its shape gradually till a plane shape is reached at the entrance of the barrel. It must be emphasized that this is only correct if the boundaries of the zones represent surfaces in the physical process with equal pressure, density and velocity. For this reason this scheme may be a good approximation when a large mass flow is established in the barrel. In fact, assuming steady-state subsonic flow at the origin, the iso-surfaces can be calculated. However, for the first implosion, when the projectile is still located at the origin, the imploding wave "regards" the origin as a plane wall and the spherical geometry will be conserved for some time after the implosion when the gas flow inside the barrel becomes important.

Owing to the unsatisfactory results of these programs and because of the rather arbitrary treatment of the flow at the origin, a different approach was followed in the present program. Spherical geometry is maintained throughout the process and the base pressure on the projectile is calculated from the average pressure over the barrel area, (see Fig.9). This is clearly an approximation since the mass outflow is neglected. This approximation can be justified as long as the projectile has not moved a great distance away from the origin and the mass outflow is still relatively small. This will be the case for a heavy projectile during the first implosion-cycle (see Ref.29).

A more flexible initial zoning scheme is used to study the influence of the initial zoning on the results. Because the spherical geometry is maintained a comparison with analytical solutions is easier to make. The program is very limited in describing the complete launcher process since there is no provision for an addition of a layer of explosive (although this can be done) or for a detailed description of barrel processes. But the comparison with theory (Sec.4) and the available experimental results (Sec.5) provides a more reliable comparison concerning the validity of the numerical experiments and justifies the present approach.

3.2 Description of the Code

Consider a closed hemispherical chamber filled with a stoichiometric mixture of hydrogen and oxygen of arbitrary initial pressure. We assume instantaneous detonation of this mixture at the centre and we follow the resulting flow field in time.

This problem can be formulated in Lagrangian spherical co-ordinates. The conservation equations combined with an artificial viscosity term can then be expressed as:

$$\text{mass} \quad V = \frac{1}{\rho_o} \frac{R^2}{x^2} \frac{\partial R}{\partial x} \qquad 3.1a$$

momentum $$\frac{\partial U}{\partial t} = - \frac{1}{\rho_o} \frac{R^2}{x^2} \frac{\partial (P + Q)}{\partial x} \qquad 3.1b$$

energy $$\frac{\partial E}{\partial t} = - (P + Q) \frac{\partial V}{\partial t} \qquad 3.1c$$

The equation of state is expressed as:

$$E = E(P, V) \qquad 3.2$$

and is similar to the one used in previous work. It is a numerical fit to date from Moffat (Ref.14) and can be found in Appendix A.

The artificial viscosity term Q is defined by:

$$Q = - \frac{(C. \Delta x)^2}{V} \left(\frac{\partial U}{\partial x} \right)^2 \text{ if } \frac{\partial U}{\partial x} < 0$$

$$Q = 0 \qquad \text{if } \frac{\partial U}{\partial x} \geq 0 \qquad 3.3$$

following the discussion of Sec. 2.3.

The detonation wave is represented according to Ref.15. The pressure, as calculated from the equation of state is multiplied by the burn factor F, given by:

$$F = \frac{1 - V}{1 - V_{CJ}} \qquad 3.4$$

where, V_{CJ} represents the Chapman-Jouguet volume. Inside the detonation front a partial pressure is taken and this will spread the detonation wave over a number of zones in the finite difference scheme similar to the shocks in the artificial viscosity technique. The factor, F, can only increase and remains equal to 1 after the detonation wave is passed. During this process the artificial viscosity term is omitted. Equation 3.1 to 3.4 can be integrated using a finite-difference method. For this the hemisphere is divided into N zones. To each zone a value of the physical and computational quantities P,V,E,Q and F are assigned, and each interface has a velocity, position and area. The equations can now be integrated in small time steps, starting from an initial value (F = 1 in the zone at the origin) and subject to the boundary conditions. The complete set of finite-difference equations is given in Appendix A, in the notation of the computer program, for which the listing is given in Appendix B.

The finite difference equations are restricted to stability conditions that can be expressed as:

$$\text{time step } \Delta t \leq \frac{1}{3} \frac{1}{\sqrt{1/a^2 + 1/b^2}} \qquad 3.5$$

with

$$a = \frac{\Delta x}{c}$$, the Courant Condition

and

$$b = \frac{1}{2} \frac{V}{C^2 \Delta V}$$, the diffusion stability.

c is the speed of sound and ΔV the compression during a time step. This form is taken from Ref.16. Only C^2 is used in (b) rather than C, and proved to be useful for $C \geq 2.5$.

The boundary conditions are simple, that is, a zero velocity at the wall and in the centre. The last condition is only valid if we deal with a closed hemisphere, but it will still be a reasonable approximation for the configuration of the Hypervelocity Launcher as long as the projectile velocity is small and the projectile is close to the origin.

The smallest possible value is used for the constant C, in Eq, 3.3 (C = 1), to reduce the effect of the artificial viscosity on the flow field outside the shock. For a proper reflection at the origin C is reduced even further in the two zones nearest to the origin and taken as 3/4 and 1/4 respectively (see Sec. 2.2).

For the case of the Hypervelocity Launcher we can calculate the projectile motion from the pressure at the origin averaged over the barrel area (Fig.9). If the projectile is close to the origin and its velocity is still low, this pressure will be equal to the base pressure on the projectile. For higher velocities, we should use the equations for an infinitely chambered gun (Ref.17) to allow for the expansion behind the projectile.

To allow for a decrease in zone mass towards the origin a constant decrease in mass as defined by the mass ratio n (Sec.2.3) is used. For a total number of zones N = 50, and a mass ratio n = 0.9, 14 zones are a distance smaller than 1/4 of the chamber radius away from the centre. For comparison, we note that in the final calculations of Sevray with 20 zones, this number was only 2, resulting in a loss of detail around the origin. A smaller value of n will shift more zones in the direction of the centre. This allows us to alter the definition of the flow near the centre for a constant number of zones. The final calculations were done with N = 50 and n = 0.875. This choice will be explained in Sec.3.3.

Finally we note that the finite difference equations, Eq. 3.1 to 3.4, are essentially the same as used in previous work at UTIAS. This main differences in the present code are:

- a spherical geometry is maintained at the origin
- a finer zoning scheme
- a simpler treatment of the stability criteria

3.3 Results of the Numerical Experiments

Some of the results of the computer program are presented in this section. A case corresponding to the actual Launcher geometry is calculated:

radius of the chamber, R_c = 105. mm

radius of the barrel, R_b = 4 mm

initial gas pressure, p_i = 200 psi, although pressures of 100, 400 and 600 psi are used also for comparison with experimental values (Sec.5).

These initial values are taken to enable a comparison with the available experimental data (see Sec.5.1). In Sec.4 details of the results will be compared with analytical solutions. The complete process however cannot be described in a consistent non-dimensionalized way as two characteristic length-scales are involved. These are the chamber radius during the initial stage of the implosion and the shock-radius in the final stage. The results are therefore in this section presented with their actual physical values of time, distance and pressure. Figure 10 shows an X-t diagram in which the particle paths are also drawn. We see a detonation wave running from left to the right, an implosion wave moving after reflection in the direction of the centre and a reflected wave. Figures 11, 12 and 13 show for each of these phases the pressure profiles at 5 μsec intervals. The pressure behind the detonation wave falls off rapidly. At the reflection from the outer wall an increase in pressure is noticeable, but the pressure behind the incoming shock drops slightly till the shock is halfway the chamber. Then a small pressure rise is observed, and only very close to the centre we see a sharp increase in pressure. The reflection of the implosion wave from the centre increases the pressure in this region by an order of magnitude but decreases rapdily as the shock moves away from the centre. An exact solution of the implosion would yield an infinite pressure at the origin at the moment of reflection and afterwards. The pressure, averaged over a finite area around the origin will still be finite (see Appendix D). For this reason the pressures will always remain finite in a finite difference scheme. This is illustrated in Fig.14 where the average pressure on the barrel area is plotted together with the pressure in the last zone at the origin. For 50 zones the pressure in the last zone exceeds the average pressure by a factor of 2. This will be higher for a finer zoning scheme and only in the limit of an infinite number of zones an infinite pressure will be reached. However, the effect of the last zone will decrease since its area decreases faster than the pressure rises. This is essential for the performance calculations of the Hypervelocity Launcher, since the base pressure on the projectile is directly related to the average pressure at the origin. If this average pressure does not converge for an increasing number of zones the performance calculations are of limited value. (NOTE: Convergence does not really occur in the calculations done by Sevray, Poinssot and Flagg and Mitchell, as a consequence of the zoning scheme they adopted at the origin. A greater number of zones will also increase the pressure in the last zone at the origin. The area over which this pressure acts is constant and equal to the barrel-area. Hence an increase in the number of zones will increase the projectile velocity). We will therefore discuss this point in more detail.

In Sec.2.3 we already discussed the effect of the artificial viscosity and the number of zones on the results. It was concluded that a minimum number of 50 zones and a value of C close to one was required. However, very close to the origin the situation is more complex. A great number of runs were made with 24 and 50 zones. In these runs we studied the effect

of a greater number of zones near the origin by varying the value of the mass ratio n. Figure 15 shows the number of zones that collapse at the moment of implosion to a radius less than the barrel radius. If the last zone is greater than the barrel radius the average pressure will be too small. This is the case for $n > 0.9$, if $N = 50$, and $n > 0.8$, if $N = 24$, and provides an upperbound to the value of n as shown in Fig.15. There is also a lower bound for the value of n. If n is small a large number of zones are shifted towards the origin. The number of zones outside the origin region is now strongly reduced and this will affect the incoming shock as we have seen in Sec.2.3 where the pressure behind the shock increases when the number of zones is made smaller than a certain critical value. The incoming shock will then be too strong and the average pressure on the barrel area too high. This is also shown in Fig.15. Consequently, there is a lower and an upper bound to the value of n, depending on the total number of zones N. These are approximately shown in Fig.16. To the left of the line a-a' the last zone at the origin is not small enough, and hence the average pressure is too small. To the right of the line b-b' the mass ratio is too small, the incoming shock is too strong and the pressure at the origin is too large. As can be seen from this figure and from Fig.15, convergence can never be achieved with 24 zones. For decreasing n, the average origin pressure continues to increase. For 50 zones the situation is already different. For $0.9 > n > 0.85$ the average pressure at the origin is constant within 5%, although the number of zones over which the average pressure is calculated increases from 2 till 12 (see Fig.15). Another point inside the region of convergence, $N = 75$ and $n = 0.9$., shows an average pressure still within 5% of the "ideal value" although 12 zones have collapsed inside the barrel radius. The region of convergence is very small and this situation is not quite satisfactory. The problem is that we want very detailed information in a small region from a program that gives only an approximate solution to the entire flow field. We must realize however, that this discussion is only restricted to a region very close to the origin. Outside this region the conditions for convergence are much less severe.

Based on this study we finally adopted a zoning scheme with $N = 50$ and $n = 0.875$.

4. COMPARISON WITH ANALYTICAL SOLUTIONS

4.1 The Detonation Process

In the numerical experiments a Chapman-Jouguet detonation is assumed. This represents only an approximation of the real physical process, but it is acceptable since we are mainly interested in the implosion wave. The results can be compared with the theoretical calculations of Benoit (Ref.18) of the properties of a Chapman-Jouguet detonation in a $2H_2 + O_2$ mixture, as the pressure and velocity at the detonation front are independent of the geometrical configuration. Only the flow field behind a detonation wave will be different for different geometries. Benoit calculated a detonation wave velocity of 3.00 mm/μsec for the present initial conditions (200 psi $2H_2 + O_2$). The numerical experiment gives a lower value of 2.52 mm/μsec. The peak pressure in the detonation wave agrees reasonably well with the ideal value (295 bar, or a pressure ratio of 20.5), as can be seen from Fig.11, although the finite zone size limits a good comparison. The pressure drops extremely rapidly just behind the detonation front and falls off more slowly till a constant value of about 65 bar is reached.

If the pressure in front of the detonation wave can be neglected, the results have to be self-similar with respect to the detonation pressure

p_D and the distance relative to the shock front ($\eta = r/r_D$). For p_D, the ideal value of 295 bar is used; r_D is defined as the position inside the detonation front where the pressure has reached half of the value p_D. A plot of $\pi(p/p_D)$ against η is shown in Fig.17 for different times after ignition. During the first 10 μsec the detonation wave is not yet established in the finite difference scheme, but the results appear to be self-similar afterwards. In the same figure the ideal solution for a "perfect" gas ($\gamma = 5/3$) is indicated (Ref.19). The numerical experiment shows a much faster drop in pressure behind the detonation front. It is not clear if this difference is caused by real gas effects and the lower value for γ (since for the detonation products of a $2H_2 + O_2$ mixture $\gamma \sim 1.2$) or is due to a computational effect.

There are unfortunately no analytical solutions available for the reflection of a spherical detonation wave in this case. Stanyukovich (Ref.20) treats the planar reflection case and following the same approach, an analytical expression for the reflection process in the neighbourhood of the wall does not seem impossible. The numerical results show a gradual decay in peak pressure till halfway in the chamber. Then the pressure starts increasing. The shock strength itself remains fairly constant at a pressure ratio of 2.5.

From Fig.17 we can see that the pressure in the region $0 \leq \eta \leq 0.5$ remains constant. The reflected detonation wave will first move into a non-uniform region. But when the shock is halfway in the chamber, it moves into a region with uniform pressure and density and zero velocity. This case of an imploding shock wave has been studied analytically and will be discussed in the next section.

4.2 The Implosion and the Reflection - some analytical solutions

The implosion of a spherical shock wave and its reflection from the center can be regarded as the most important part of the process. Most of the interest in implosion waves arises from the very high-temperature, high-pressure region that is left at the center after the reflection. In the UTIAS Implosion-Driven Hypervelocity Launcher, this gas is used to drive a projectile. An analytical approach to the implosion and reflection problem is extremely difficult due to the complexity of the non-linear partial differential equations and its boundary conditions. Guderley (Ref.21) obtained in 1942 a similarity solution for the implosion and reflection in spherical and cylindrical geometry. His solution is still today the only solution that describes the flow field after the reflection. His basic assumptions are:

- a strong shock during the implosion phase so that the pressure in front of the shock can be neglected
- a region close to the origin
- a perfect gas

In this solution the position of the shock can be expressed as:

$$r_s = (\mp t)^n \qquad (4.1)$$

the pressure as $p \alpha (r)^{2-2/n}$ or $p \alpha r^{-\delta}$ (4.2)

and the velocity as $v \alpha (r)^{1-1/n}$ or $v \alpha r^{-\delta/2}$ (4.3)

The exponent n is a constant, depending on γ, and is equal to 0.7571 for $\gamma = 1.2$. The strength of the incoming shock increases towards the origin and will be infinite for r = 0. The gas behind the imploding shock flows in the direction of the origin and will be compressed due to the converging geometry. The reflected shock moves into this compressed region with a constant and finite Mach number, giving an additional increase in pressure. The pressure drops afterwards. (see Fig. 20 and the figures of Appendix D). Guderley's solutions will always be obtained very close to the origin as long as spherical symmetry is maintained. It therefore provides a limit for other approximate solutions. In Appendix (D) this solution is evaluated for different values of γ and some properties are discussed in more detail.

The increase in strength of an imploding shock of arbitrary strength can be expressed using the analyses of Chester (Ref.22), Chisnell (Ref.23) and Whitham (Ref.24). Chester analyzed the defraction of a shock around a corner and generalized these results for arbitrary area changes. Chisnell calculated the increase in shock strength as a small area change in a uniform channel was encountered. He calculated also the corrections for re-reflected waves and found that they were extremely small. Whitham formulated a very simple rule for the propagation of shock waves. This rule states that to a first approximation the increase in strength of a shock, propagating into a non-uniform region is only dependent on the local conditions at the shock front. The influence of the flow field behind the shock can then be neglected. This rule includes the expressions of Chester and Chisnell and we will refer to it as the W-C-C-rule. For spherical geometry it can be expressed as:

$$r_s^2 f(z) = \text{constant}$$

f(z) is a complicated function of the shock strength z and γ, and is given in Appendix C. Although this rule is only an approximation, it turns out to be a very good approximation. For very strong shocks ($z \to \infty$) the difference with Guderley's solution is very small:

W-C-C-rule $z \alpha R^{-0.652}$

Guderley $z \alpha R^{-0.641}$

for $\gamma = 1.2$. This rule is however of limited use since it does not give any information on the flow field behind the shock.

Lee (Ref.25) studied extensively the flow field behind imploding shocks of moderate strength. His quasi-similar solution is based on the assumption that pressure, density and velocity are weakly dependent on a change in shock Mach number but strongly dependent on their position behind the shock front. He obtained solutions of the flow field behind the imploding shock for different shock Mach numbers. In his paper only the cylindrical case is treated in detail so that unfortunately the results of the present numerical results cannot be compared with his theory.

4.3 The Implosion and the Reflection - Comparison with Numerical Experiment

We will now compare the results of the numerical experiment with

some of the analytical solutions discussed in the previous section. We assume the region in front of the imploding shock to be at constant pressure and density and at rest. Further, we assume $\gamma = 1.2$ for the detonation products (Ref.18). We must also keep in mind that the gas is not perfect, as it is assumed in all the analytical expressions.

The distance can be non-dimensionalized in two different ways. We distinguish $r^* = r/R_c$ if the position is expressed relative to the chamber radius and $\eta = r/r_s$ if the position is taken relative to the shock front position. The pressure is non-dimensionalized with respect to the pressure in front of the imploding shock, p_o. Only in Guderley's solution, where the pressure in front of the shock is neglected, the pressure just behind the incoming shock p_s is used (see Appendix D).

The pressure ratio of the imploding shock, p_s/p_o, as a function of the distance, r_s^*, the position of the shock relative to the chamber radius, is shown in Fig. 18, and compared with the strong shock solution of Guederley and the W-C-C-rule. The difference between the numerical results and the W-C-C-rule is less than 10%. For the larger values of r_s^* the pressure increases slower and for the smaller values of r_s^* the pressure rises more rapidly. At the barrel radius ($r_s^* \sim 0.04$) the pressure ratios are approximately the same. The shock Mach number, $M_s = 1.5$ at $r_s^* = 0.5$, increases and $M_s = 3.3$ at the barrel radius, $r_s^* = 0.038$. The differences with the strong shock solution are larger, but considering the very moderate Mach numbers, are still rather small. This does not mean, however, that the strong shock solution will also give a fair approximation of the flow field behind the shock. The flow behind the shock depends upon the shock strength, but also on the geometry behind the shock. This is illustrated in Fig.19 for the velocity. The velocity is non-dimensionalized with respect to the shock velocity ($\phi = u/u_s$) and the distance with respect to the shock radius ($\eta = r/r_s$). The velocity will be zero at the outer wall. This is the case for $\eta = 2.3$ if $r_s^* = 0.44$ ($M_s = 1.57$) and for $\eta = 9.1$ if $r_s^* = 0.11$ ($M_s = 2.26$). In the same figure the strong shock solution is indicated as computed by Flagg (Ref.10), where, $\phi \to 0$ as $\eta \to \infty$, and this is only possible if $r_s^* \to 0$. In other words, the entire flow field can only be described by the strong shock solution in the limit of $r_s^* \to 0$. An analytical solution of the flow behind the shock for an implosion in a sphere has to take into account both the effect of moderate shock strength and the influence of the wall. In the theory of Lee only the moderate shock strength is accounted for. His solution therefore is restricted to a region close to the shock (η of order one).

A very illustrative graph of the effect of the reflection is obtained if we plot the pressure as a function of time at a fixed distance from the origin. We will first discuss the strong shock solution. Since this solution is self-similar, the distance from the origin, the pressure and the time can be chosen arbitrarily. As the unit of pressure, the pressure (p_o) behind the imploding shock is used and as the unit time the time (t_{imp}) the shock needs to move to the origin is used. This pressure profile is shown in Fig. 20 for $\gamma = 1.2$. Similar plots for other values of γ can be found in Appendix D. The gas is first shock-compressed by the imploding shock and this is followed by an adiabatic compression as the flow behind the shock takes place in the direction of the origin into a converging geometry. At the time of the arrival of the reflected shock the pressure is increased due to the adiabatic compression by a factor of 22. The flow is then shock-compressed by the

reflected shock with a pressure ratio of ~ 6. The reflected shock reverses the flow direction and the pressure will fall off afterwards. The reflected shock is about 6.4 times slower than the incoming shock.

Similar plots are made for the implosion in a sphere. In this case we have used the actual values of pressure and time. Pressure profiles are plotted for distances of r* = 0.5, 0.2, 0.1 and 0.038 (the barrel radius). For r* = 0.5 the pressure decreases slowly after the incoming shock. The reflected shock is very weak. For r* = 0.2, some adiabatic compression is noticeable after the incoming shock. This is more pronounced for r* = 0.1 and r* = 0.038. The strength of the reflected shock is almost constant. Table 4.1 shows the increase in pressure due to the incoming shock, the adiabatic compression, and the reflected shock for each of these cases and for the strong shock solution. The increase in strength is expressed as a pressure ratio.

TABLE 4.1

Distance r*	Mach number M_s	Pressure ratio of: impl.shock	adiab.compr.	refl.shock
0.5	1.5	2.5	0.8	1.5
0.2	1.9	3.8	1.3	1.9
0.1	2.3	5.9	2.0	2.0
0.038	3.5	~12.9	~3.2	~2.1
$r_s \rightarrow 0$	∞	$\alpha r_s^{-0.641}$	22.0 (strong shock solution)	5.95

In all cases the difference between the strong shock solution is quite appreciable. The main reasons are that the flow in the direction of the origin, necessary to maintain the similarity solution of Guderley, is restricted because of the wall influence and the moderate values of M_s. As a consequence both the adiabatic compression and the strength of the reflected shock are far below their "strong shock" value. The absolute value of the pressure at the reflected wave drops much faster than the "strong shock" solution indicates. (see footnote). This is shown in Fig.22 where the pressure at the reflected shock is compared with the pressure calculated from the strong shock solution. The pressure after reflection is more than an order of magnitude smaller than the ideal value in the range $0.04 \leq r^* \leq 0.5$. The ideal values might be obtained for values of $r^* < 0.01$, or for a 8" dia. chamber at a distance less than 1 mm away from the origin. We conclude that the pressure ratio of the incoming shock agrees reasonably well with the available theory. The flow behind incoming shock can only be treated analytically if the effect of the outer wall is taken into account. Although the reflection process behaves qualitatively Roberts (Ref.26) did some approximate calculations of projectile velocity in the gas case. He assumed the 'classical behaviour' of the strong shock solution for the imploding and the reflected wave, using a value for the similarity exponent n derived from the experimental implosion wave trajectory. He also assumed for the pressure ratio over the reflected wave the classical value 3.3, valid only for $\gamma = 1.4$, but did not account for any adiabatic compression. The total pressure ratio upon reflection obtained from the numerical experiments is ~6., the drop in pressure for the reflected wave is much stronger than the classical model indicates. The two effects are opposite and for this rather fortunate reason are the velocities he calculated in reasonable agreement with the measurements.

similar to the strong shock solution, the actual values are more than an order of magnitude lower.

5. THE APPLICATION OF IMPLOSION WAVES FOR HYPERVELOCITY LAUNCHER

5.1 Comparison of the Numerical Model with Experiments

The measurements at UTIAS on spherical detonations and implosions are restricted to the particular geometry of the UTIAS Implosion-Driven Hypervelocity Launcher. Watson (Ref.28) measured with pressure and ionization gauges points on the detonation and implosion wave trajectories. More recently Roberts (Ref.26) studied the implosion phase by photographic and spectroscopic means, looking into a 1" dia. quartz observation window at the origin. Velocity measurements in the barrel by Elsenaar (Ref.29) during the first 300 μsec after ignition provided an indication of the total pressure pulse at the origin. Watson measured a time of 35 μsec between ignition and the arrival of the detonation front at the wall of the hemispherical cavity. The numerical experiment gives a time of 42 μsec for the same initial pressure of 200 psi. Both Watson and Roberts measured an implosion time of 76 μsec, as compared with 89 μsec from the numerical calculations. The difference is appreciable only a part of it can be attributed to an incorrect representation of the initial detonation process in the numerical experiments, since the detonation wave will be over-driven in its initial stage.

Roberts observed different degrees of collapse of the implosion wave. The temperature he measured represents an average temperature over the area of collapse, typically about 6 mm in diameter, although higher values were observed. The temperature was also a function of the degree of collapse. Peak temperatures between 4000 and 5500 ^{o}K were observed. There was no clear trend of temperature with respect to initial gas pressures (100, 200 and 400 psi). Before and after the implosion a constant temperature of 3000 ^{o}K was observed.

The idealized theory will give an infinite temperature at the origin. But as was the case for the pressure, a temperature averaged over a finite area will still be finite, and arbitrary large, depending on the area. In the numerical program spherical geometry is maintained throughout the implosion process and the program does not allow for a finite degree of collapse as observed in the experiments. The program will therefore not describe the actual physical process at the implosion but a comparison with the experimental values may still be useful. For this the temperature is arbitrarily averaged over the barrel area (8 mm dia) similar to the procedure for the pressure. Since in the computations the molecular weight of the oxygen-hydrogen mixture was fixed at a value of 12, the temperatures had to be corrected for the change in molecular weight. The equilibrium data for a H_2-O_2-He system as a function of pressure and temperature by Benoit (Ref.27) are used for this correction. Figure 23 shows the measured and calculated temperature profiles. The difference in peak temperature is in view of the previous remarks acceptable. The calculated value is ~ 25% higher than the measurements indicate. More difficult to explain is the fast drop in the measured temperature after the peak temperature is reached. The calculated temperature falls off much slower. It is not clear what the reason is.

Measurements of projectile velocity inside the barrel were done by Elsenaar, using a microwave-Doppler method. When the projectile is still near

the origin and its velocity is small compared with the value of the escape speed of the gas at the origin, the base pressure on the projectile will be equal to an averaged pressure at the origin. For this case we can calculate the velocity profile from an average pressure over the barrel area in the numerical calculations. Measured and calculated velocity profiles for the first implosion are shown in Fig.24 for 400 psi and in Fig.25 for 600 psi initial pressure. The agreement is acceptable. The velocity after the first implosion is approximately 1.25 m/sec times the initial pressure in psi. The muzzle velocity in these cases was much higher, due to subsequent implosions. For a more detailed analysis of these measurements see Ref.29.

5.2 Parametric Study of the Launcher Performance

The application of combustion-driven implosion waves is of limited value for hypervelocity launchers. Velocities obtained in this way with an 8" dia. chamber at UTIAS are of the order of 5000 ft/sec and a large part of this velocity can be contributed to pressure pulses due to subsequent implosions (see Ref.29). The reason is that the implosion wave is weak; the Mach number halfway in the chamber is 1.5; at the barrel radius 3.3. A considerable increase in shock strength can be obtained by "coating" the hemispherical wall with a layer of explosive. The detonation wave is now used primarily to initiate the detonation of the explosive, typically PETN. This will generate a strong blast wave that will gradually transform into a strong implosion wave because of the converging geometry. It is hoped that in this way projectile velocities in excess of 30,000 ft/sec can be obtained.

Optimization studies of an 8" dia. chamber are made for this case by Sevray (Ref.11) and for even larger diameters (20" and 30") by Flagg and Mitchell (Ref.12) using a finite difference technique. The calculated projectile velocities are about double the actual velocities obtained experimentally. It is as yet difficult to say if this is caused by losses for which no provision is made in the calculations, or that these calculations overestimate an ideal lossless performance. It is likely that losses will be important for the very extreme conditions at the origin. But the small number of zones used in the calculations and the treatment of the flow at the origin indicates an overestimation by the theory (see Section 2.3 and the Note in Section 3.3). Calculations for the explosive case, similar to the one presented in this report for the gas case, may give an answer to this question.

A disadvantage of the finite difference technique is that no analytical expression for the launcher performance can be obtained. Optimization studies require a comparison between a great number of cases and even then it is difficult to estimate which parameter is the most critical. The complexity of the flow forces one to simplify the problem greatly in order to obtain an analytical expression but such an expression may still be useful. An attempt in this direction is made by combination of three different theories, describing respectively the detonation of the explosive, the flow towards the origin and the reflection at the origin.

Bach and Lee (Ref.30) treated the problem of a converging spherical or cylindrical blast wave using a series-expansion technique. The first order approximation is the planar blast wave and higher approximations are subsequently obtained taking into account the converging geometry. The pressure in front of the blast wave is neglected and instantaneous release of energy at

the wall is assumed. This theory describes the flow field over a large part of the chamber but breaks down near the origin as can be expected. The shock Mach number reaches a minimum at approximately halfway of the chamber and then starts increasing in the direction of the origin. A characteristic time:

$$t^* \equiv \sqrt{\frac{\rho_o \, 2\pi \, R_c^5}{3 \, E_o}} \qquad \text{for a hemispherical chamber,} \quad (5.1)$$

a characteristic distance:

$$x_s = \frac{r_s - R_c}{R_c} \qquad (5.2)$$

and a characteristic sound speed:

$$c^* = \frac{t^* \, c_o}{R_c} \qquad (5.3)$$

are used to describe the problem. ρ_o is the initial density, in front of the blast, c_o the sound speed, and E_o the explosive energy. A solution for the shock speed $\dot{x}_s$, is defined as $dx_s/dt/t^*$ is obtained and can be expressed as:

$$\dot{x}_s^{\,2} = \frac{1}{x_s} \sum_{n=0}^{\infty} F_n \, x_s^{\,n} \qquad (5.4)$$

The coefficients F_n are, till fourth order, given for $\gamma = 1.4$ by:

$$\begin{aligned} F_1 &= -0.27494 \\ F_2 &= 0.33705 + 2.14334 \, c^{*2} \\ F_3 &= -0.34409 - 0.52417 \, c^{*2} + 4.94771 \, c^{*4} \\ F_4 &= 0.33910 + 0.59577 \, c^{*2} + 1.69620 \, c^{*4} + 44.0491 \, c^{*6} \end{aligned} \qquad (5.5)$$

For small c^* $\dot{x}_s \sim 1$ halfway the chamber. From $\dot{x}_s$ the shock Mach number follows from:

$$M_s = \frac{\dot{x}_s}{c^*} \qquad (5.6)$$

and the Rankine Hugoniot pressure ratio

$$Z_b = p_s/p_o = \frac{2\gamma}{\gamma+1} \, M_s^{\,2} - \frac{\gamma-1}{\gamma+1} \qquad (5.7)$$

The procedure we follow is to calculate the minimum value of M_s and its position

x_s, approximately halfway the chamber. From this point we proceed with the W-C-C-rule. This rule gives a fairly good approximation for the increase in shock strength in the direction of the origin, as was shown in Sec. 4.3. This rule can be expressed as:

$$r_s^2 \, f(z) = \text{constant} \tag{5.8}$$

The function f(z) is given in Appendix C. The pressure ratio β_b of the shock at the barrel radius can then be calculated from:

$$f(Z_b) = \left[\frac{(rs)_{min}}{R_b} \right]^2 f(z_{min}) \tag{5.9}$$

where, $(r_s)_{min}$ and $(z)_{min}$ follow from x_s and p_s/p_o where M_s is a minimum. Only for very strong shocks and in the absence of an outer wall is Guderley's solution applicable to the final implosion and reflection. As shown in Sec. 4.3 the pressure at the origin for $M_b = 3.3$ is more than an order lower than the strong-shock solution predicts, and the drop in pressure after the reflection is much faster mainly because of the influence of the outer wall. This difference will be much smaller for higher Mach numbers but it is as yet not possible to give a quantitative expression. Such an expression has to take into account both the effects of finite Mach number and of the wall. For a fixed value of the barrel radius, (R_b) the Mach number at the barrel radius is the only important parameter. A detailed study of the influence of M_b on the pressure at the origin should be extremely useful in this regard.

The velocity of the projectile can be approximated by:

$$v = \frac{A}{m} \int p_{base} \, dt \tag{5.10}$$

if we use for p_{base} the average pressure over the barrel area. The average pressure is in Guderley's solution proportional to the absolute pressure, p_b at the radius of the barrel behind the imploding wave (see Appendix D). The time is proportional to the implosion time, that is the time the shock needs to move from the barrel radius to the center. This time is given by (Appendix D):

$$t^{**} = n \frac{R_b}{M_b \, c_o} \tag{5.11}$$

The product of p_b and t** can be used as the scale factor for the total impulse given to the projectile. A high value of t** and a low value of p_b will mean a broad pressure pulse. A small value of t** and a high value of p_b indicates a very sharp pulse. The total pressure pulse however may still be the same in these cases. We therefore define a characteristic impulse:

$$\chi = Z_b \, p_o \, t^{**} = p_b \, t^{**} \tag{5.12}$$

For the ideal strong shock solution the impulse on the projectile will be proportional to χ (see Appendix D). In the actual case, when the shock is not

strong but increases in strength towards the center, the velocity will also be a function of the Mach number M_b at the barrel radius. Although we can as yet not say how this will influence the total impulse (Fig.22 indicates that the increase for $M_b \to \infty$ will be of the order of 10), we can say that an increased value of M_b will increase the performance. Based on M_b and χ a limited comparison is therefore possible. If both M_b and χ increase, the projectile velocity will increase; but if χ increases and M_b decreases the comparison is inconclusive. We will now see how a change in the parameters E_o, ρ_o, R_c and c_o will affect the values of χ and M_b.

I. Variation of explosive energy E_o.

From (5.1) we see that:

$$t^* \alpha \sqrt{\frac{1}{E_o}} \quad , \qquad c^* \alpha \sqrt{\frac{1}{E_o}}$$

Since $\dot{x}_s \sim 1$ halfway the chamber, the shock Mach number at this position is:

$$M_s \alpha \frac{1}{c^*} \alpha \sqrt{E_o}$$

As a good approximation, the Mach number at the barrel radius, M_b, is proportional to M_s,

$$M_b \alpha M_s$$

using Eq. (5.7):

$$Z_b \alpha M_s^2 \alpha E_o$$

and

$$t^{**} \alpha 1/M_s \alpha 1/\sqrt{E_o}$$

or

$$\chi = Z_b \cdot p_o \cdot t^{**} \alpha \sqrt{E_o}$$

and

$$M_b \alpha \sqrt{E_o}$$

The increase in projectile velocity will be at least proportional to $\sqrt{E_o}$. Flagg (Ref.12) found that the velocity was proportional to $\sqrt{E_o}$ for a wide range of explosive energies. Table 5.1 shows the calculated values of M_b and χ for explosive weights of PETN between 50 and 250 g.

TABLE 5.1

Properties of the Detonation Products of $2H_2 + O_2$ in Front of the Implosion Wave:

p_o = 65 bar, for initial pressure p_i = 200 psi

$\rho_o = 0.461 \times 10^{-2}$ g/cm^3

$c_o = 1.25.10^5$ cm/sec

$\gamma = 1.4$ for blast wave

$\gamma = 1.2$ for implosion wave

$R_o = 10$ cm

1 g PETN is equivalent to 1.235 kcol.

Explosive weight (g)	t* (μsec)	M_b	Z_b	$p_b = Z_b . p_o$ (kilobar)	t** (μsec)	$\chi = p_b . t^{**}$ (kilobar.μsec)
50	19.18	10.82	127.7	8.3	0.224	1.86
100	13.56	14.82	239.6	15.6	0.164	2.56
250	11.07	17.94	351.1	22.8	0.135	3.08
200	9.59	20.59	462.3	30.0	0.118	3.54
250	8.57	22.94	574.0	37.3	0.105	3.92

II. Variation of initial chamber pressure p_i.

If p_i is increased, the pressure and density in front of the imploding wave will be increased in the same ratio. Hence;

$$p_o \alpha p_i$$

$$\rho_o \alpha p_i$$

$$t^* \alpha \sqrt{\rho_o} \alpha \sqrt{p_i}$$

$$c^* \alpha t^* \alpha \sqrt{p_i}$$

$$M_b \alpha M_s \alpha 1/c^* \alpha 1/\sqrt{p_i}$$

$$t^{**} \alpha 1/M_b \alpha \sqrt{p_i}$$

$$Z_b \alpha M_b^2 \alpha 1/p_i$$

$$p_b = Z_b . p_o \alpha 1$$

We find that $M_b \alpha 1/\sqrt{p_i}$ and $\chi \alpha \sqrt{p_i}$.

An increase in initial pressure does not influence the absolute pressure

at the barrel radius, but since the shock moves slower, the pressure acts over a longer time and will tend to increase the velocity. The decrease in M_b has an opposite effect and it is not possible to say what the total effect on the projectile velocity will be. Sevray found a decrease in velocity with increasing initial pressure. This was less pronounced in the calculations of Flagg and Mitchell for larger diameters. Table 5.2 shows the values of M_s and χ for initial pressures of 200, 400 and 600 psi and 100 g PETN.

TABLE 5.2

p_i (psi)	p_o (bar)	ρ_o (g/cm^3)	t^* (μsec)	M_b	Z_b	$p_b = Z_b . p_o$ (kilobar)	t^{**} (μsec)	$\chi = p_b . t^{**}$ (kilobar μsec)
200	65.	$0.461.10^{-2}$	13.56	14.82	239.6	15.6	0.164	2.56
400	130.	$0.922.10^{-2}$	19.18	10.82	127.5	16.6	0.223	3.70
600	195.	$1.383.10^{-2}$	23.49	9.10	90.2	17.6	0.267	4.70

III. Variation of chamber radius R_c.

If we increase all the dimensions by the same factor, the final performance will be the same:

$$E \alpha R_c^3$$

$$t^* \alpha R_c$$

$$c^* \alpha 1$$

$$M_b \alpha 1$$

$$Z_b \alpha 1$$

$$t^{**} \alpha R_c$$

$$v \alpha \frac{A.t^{**}}{m} \quad Z_b \quad p_o \alpha \frac{R_c^2 R_c}{R_c^3} = 1$$

Flagg found a small increase with chamber diameter, although not very pronounced. The performance will increase if we enlarge the chamber but hold the projectile size on a fixed value. Recent investigations with a program similar to the one used in Ref.12, to study the effect of the chamber radius for a fixed projectile size, have shown a decreasing velocity for decreasing chamber radii. The decrease in velocity is however much less pronounced than can be expected from this simple analysis. This may be caused by non-linear effects in the wave process but the calculations itself give also cause to some concern.

IV. The effect of the driver gas.

In the present mode of operation a detonation wave is used to initiate the explosive layer of PETN. The blast wave formed by the explosive will move into the detonation products of the combustible gas. It may be of interest to see what affect the gas properties have on the performance. These properties are determined by the density ρ_o, speed of sound c_o and γ. A smaller value of γ gives higher pressures on reflection (see Appendix D). A variation in ρ_o and c_o can be studied with this simple model:

$$t^* \alpha \sqrt{\rho_o}$$

$$c^* \alpha t^* \; c_o \alpha \sqrt{\rho_o} \; c_o$$

$$M_b \alpha M_s \alpha \frac{1}{c^*} \alpha 1/ \sqrt{\rho_o} \; c_o$$

$$t^{**} \alpha 1/M_b \; c_o \alpha \sqrt{\rho_o}$$

$$Z_b \alpha 1/M_b^2 \alpha 1/ \rho_o \; c_o^2$$

$$\chi \alpha Z_b \; p_o \; t^{**} \alpha p_o/\sqrt{\rho_o} \; c_o^2$$

$$M_b \alpha 1/\sqrt{\rho_o} \; c_o$$

This is an interesting result. From the theory of hypervelocity launchers (Ref.17) it can be shown that for conventional drivers a low acoustic impedance ρc is required for an optimal performance. A lower acoustic impedance gives a more efficient conversion of thermal energy into kinetic energy inside a rarefaction wave. This will still be true for the rarefaction wave formed behind the projectile in an implosion-driven launcher. But to obtain the maximum absolute pressure and duration of the pressure pulse at the origin a low value of $\sqrt{\rho_o} . c_o^2$ is preferable. This difference in behaviour may be better understood if we realize that the analysis for conventional drivers is based on a steady-unsteady flow analysis (i.e., steady nozzle flow and unstead expansion waves). The present analysis is based on the impulse loading of the projectile, emphasizing the importance of the time scale. The two requirements are opposite, and a compromise will have to be found, e.g., the ratio of acoustic impedances for air and hydrogen is 3.64, the ratio of the quantities $\sqrt{\rho_o} c_o^2$ is 0.124 (initial pressure 200 psi, room temperature). Since the influence of the sound speed is so pronounced it is worthwhile to compare two cases of a 'cold' gas (hydrogen and air) with the 'hot' case formed by the detonation products of oxygen and hydrogen. This is done in Table 5.3 for an initial pressure of 200 psi and 100 g explosive PETN. Note that the pressure in the hydrogen-oxygen mixture is increased because of the foregoing detonation process.

TABLE 5.3

p_i = 200 psi, 100 g PETN

$2H_2 + O_2$: $\rho_o = 0.461.10^{-2}$ g/cm^3 $c_o = 1.25.10^5$ cm/sec
after detonation

$\gamma = 1.4$ for the blast wave

$\gamma = 1.2$ for the implosion wave

H_2: $\rho_o = 0.112.10^{-2}$ $c_o = 1.37.10^5$

air: $\rho_o = 1.615.10^{02}$ $c_o = 0.347.10^5$ room temperature

$\gamma = 1.4$ during the whole process

gas	p_o (bar)	t* (μsec)	M_b	Z_b	$p_b = Z_b \cdot p_o$ (kilobar)	t** (μsec)	$\chi = p_b \cdot t^{**}$ (kilobar. sec)
$2H_2 + O_2$	65.	13.56	14.82	239.6	15.6	0.164	2.56
H_2	13.8	6.68	28.92	976.0	13.5	0.074	1.00
air	13.8	25.38	30.04	1052.6	14.5	0.291	4.22

Hydrogen, with a very high sound speed is not very attractive since M_b increases but χ decreases. The situation for air is quite different. Both M_b and χ are approximately doubled and an increase in performance of at least a factor of two can be expected. However, if a cold gas is used as a driver, another way of initiating the explosive layer will have to be found. It may be possible to use a layer of light-sensitive explosive on top of the layer of PETN. The free choice of a driver gas in that case will be quite attractive for optimization.

It is worthwhile to compare finally a case with explosive and one without explosive on the basis of M_b and χ. In the gas case, for an initial pressure of 400 psi we found (Sec.4.3) $M_b = 3.3$, $c_o = 1.25.10^5$ cm/sec and $p_b = 1.5$ kilobar. Under these conditions $t^{**} = 0.74$ and $\chi = 1.1$. In the explosive case (100 g PETN, 400 psi $2H_2 + O_2$, Table 5.2) we have $\chi = 3.7$ and $M_b = 10.82$. M_b and χ are both increased by a factor of 3.3 and the velocity will also be increased by 3.3 at least. The measurements show an increase in muzzle velocity by a factor of 2.25. An increase based on the velocity after the first implosion will be between 2.25 and 6. (see Ref.29).

It must be emphasized that the analysis given above is only very approximate since we could not account properly for the effect of an increasing Mach number. Further we assumed a very ideal model:

- instantaneous release of the explosive energy
- the effect of the detonation wave is neglected
- the pressure drop at the origin because of the motion of the projectile is neglected

- the calculations are based on a perfect gas

The calculations, however, are useful in predicting trends for a change in the different parameters.

6. CONCLUSIONS

We have considered a hemispherical cavity, filled with a stoichiometric mixture of oxygen and hydrogen at relatively high pressures (typically 200 psi). A spherical detonation wave, initiated at the center moves outwards, reflects from the wall of the cavity and propagates subsequently as an implosion wave in the direction of the origin where it leaves after reflection a region of high-temperature, high-pressure gas. The resulting flow field is studied in a numerical experiment, using a finite difference method for the integration of the one-dimensional Lagrangian equations combined with an artificial pressure term to represent the detonation wave and the shocks. A reasonably realistic equation of state is used. The application of this technique to this problem is studied in some detail, in particular with respect to the reflection of a shock from a wall and with respect to a converging spherical geometry. It is shown that during the reflection, the artificial viscosity can lead to appreciable errors in the density, but that a local change in the magnitude of this artificial pressure term can reduce this effect. An artificial viscosity term based on a velocity gradient may be used in a converging geometry, provided that enough zones are used in the finite difference approximation. If the number of zones is too small, the pressure will be overestimated.

Pressure profiles at different instants of time are shown for the detonation, the implosion, and the reflection phase of the process. The detonation increases an initial pressure of 14.5 bar (200 psi) to an average pressure of approximately 65 bar. The temperature rises from 300°K initial to 3000°K after the detonation. A peak pressure at the origin, averaged over an area of 0.5 cm^2 ~ 6000 bar is reached just after the reflection of the implosion wave and falls off rapidly afterwards. A pressure of 3000 bar persists over a length of time of ~ 2.5 μsec. A peak temperature of 5500°K is reached in this case. The temperature falls off much slower than the pressure.

The results are also compared with some analytical solutions. The detonation wave was found to be self-similar with respect to the position of the detonation front. The pressure ratio of the implosion wave, formed some time after reflection of the detonation wave from the wall of the cavity is in reasonable agreement with the analytical expression of Chester, Chisnell and Whitham. Even the difference with the strong shock solution of Guderley never exceeds 20%. The pressure ratio of the reflected wave, however, is more than an order of magnitude lower and the pressure drop much faster than can be expected from the strong shock solution although the results are qualitatively very similar. These differences can be attributed to the very moderate shock Mach numbers in this case (M_s ~ 3.5 at a distance of 1/25 of the chamber radius) and to the restrictive influence of the wall, limiting the flow of mass in the direction of the origin, necessary to maintain the self-similar solution of Guderley.

This program is also used to calculate the initial projectile velocities if the high-pressure, high-temperature region at the origin is applied to accelerate a projectile-mass (the case of the UTIAS Implosion-Driven Hypervelocity

Launcher). For this the pressure at the origin is averaged over the barrel area. The present program is different in this respect from previous calculations at UTIAS, where the spherical geometry was not maintained at the origin in order to allow for the flow of mass into the barrel. The present results were tested for convergence. However, it does not seem very attractive from the numerical point of view to derive detailed information on the conditions at the origin from a program that gives only an approximate description of the entire flow field inside the chamber. Nevertheless, the experimental results for the case of temperature at the origin and initial projectile velocities compare favorably with the numerical results.

A parametric analysis, based on analytical expressions for an imploding blast wave to describe the detonation of the explosive, the strong-shock solution for the final implosion and reflection and the rule of Chester, Whitman and Chisnell for the intermediate region, is made for the case of explosive-driven implosion waves. The greatest limitation of this approach is that the implosion and reflection of shocks of moderate strength is still very much of an unknown. Although the present work gives some indication of the differences between the moderate and strong shock, a detailed study of the effect of variation in shock strength and the influence of the wall could not be made. A further study of this point, considering not only the implosion but also the reflection process, should be one of the first objectives for further theoretical work. The result of a qualitative analysis, however, seems to indicate that a driver gas with a low value of γ and a low sound speed would be favorable for this type of impulsive driving.

If air is used as a driver gas instead of the detonation products of a hydrogen-oxygen mixture, the predicted performance of the UTIAS Implosion-Driven Hypervelocity Launcher can be improved by a factor of 2 at least. Light-sensitive explosives would have to be used in this case to initiate the layer of explosive. It is possible that other gas combinations may be even better.

REFERENCES

1. Annual Progress Report, Institute for Aerospace Studies, University of Toronto 1959.

2. Glass, I. I. — Research Frontiers at Hypervelocity. Canadian Aeronautics and Space Institute, Journal, 13, Nos. 8,9, 1967.

3. von Neumann, J. Richtmyer, R. D. — A Method for the Numerical Calculation of Hydrodynamic Shocks. Journal of Applied Physics, p. 232, Vol.21, March 1950.

4. Cameron, I. G. — An Analysis of the Errors Caused by Using Artificial Viscosity Terms to Represent Steady State Shock Waves. Journal of Computational Physics. Vol.1. No.1, 1966.

5. Fox, L. — Numerical Solution of Ordinary and Partial Differential Equations. Pergamon Press, Oxford, 1962.

6. Latter, R. — A Similarity Solution for a Spherical Shock Wave. The Rand Corp. RM-1435, February 1955.

7. Brode, H. L. — Numerical Solutions of Spherical Blast Waves. The Rand Corp. RM-1363-AEC, September 1954.

8. Payne, R. B. — A Numerical Method for a Converging Cylindrical Shock. Journal of Fluid Mech. 2, p.185 (1957).

9. Brode, H. L. et al. — A Program for Calculating Radiation Flow and Hydrodynamic Motion. The Rand Corp. RM-5187-PR, April 1967.

10. Flagg, R. G. — The Application of Implosion Wave Dynamics to a Hypervelocity Launcher. UTIAS Report No. 125, 1967.

11. Sevray, P. A. L. — Performance Analysis of UTIAS Implosion Driven Hypervelocity Launcher. UTIAS Tech. Note No. 121, 1968.

12. Flagg, R. F. Mitchell, G. P. — An Optimization Study of the UTIAS Implosion Driven Hypervelocity Launcher MK II, UTIAS Tech. Note No. 130, November 1968.

13. Poinssot, J. C. — A Preliminary Investigation of a UTIAS Implosion-Driven Shock Tube. UTIAS Tech. Note No. 121, 1968.

14. Moffat, W. G. — The Thermodynamic and Electrical Properties of Dissociated Combustion Gases. Magnetogasdynamics Laboratory, MIT, Report. 61-5, 1961.

15. Wilkens, M. L. — Calcul de Detonation Mono - et Bidimensionelles. Colloques Internationaux du Centre National de la Recherche Scientifique, No.109, "Les Ondes de Detonation", 1962.

16. Berni Alder, et al. Methods in Computational Physics, Vol.3, Academic Press, 1964.

17a. Glass, I. I. Hypervelocity Launchers, Part I: Simple Launchers, UTIAS Review 22, 1963.

17b. Glass, I. I. Hypervelocity Launchers, Part II: Compound Launchers-Driving Techniques, UTIAS Review 26, 1965.

18. Benoit, A. Properties of Chapman-Jouguet Detonation in Stoichiometric Hydrogen-Oxygen Mixtures Diluted with Helium and Hydrogen. UTIAS Tech. Note No. 104, Dec 1966.

19. Sedov, L. I. Similarity and Dimensional Methods in Mechanics, Academic Press, 1959.

20. Stanyukovich, K. P. Unsteady Motion of Continuous Media. Pergamon Press, 1960.

21. Guderley, G. Strong Spherical and Cylindrical Shock Waves in the Neighbourhood of the Center of the Sphere or the Axis of the Cylinder. Luftfahrtforschung, Vol. 19, No.9, pp 302-312, 1942.

22. Chester, W. The Propagation of Shock Waves in a Channel of Non-uniform Width. Quarterly Journal of Mechanics and Applied Mathematics. Vol. VI, Pt. 4, 1953.

23. Chisnell, R. F. The Motion of a Shock Wave in a Channel, with Application to Cylindrical and Spherical Shock Waves. Journal of Fluid Mechanics. 2, p.286, 1957.

24. Whitham, G. B. On the Propagation of Shock Wave Through Regions of Non-uniform Area of Flow. Journal of Fluid Mechanics, 4, p.337 (1958).

25. Lee, B. H. K. Non-Similar Solutions of Imploding Shocks and Detonations. Gasdynamics Research Laboratory, Dept. of Mechanical Engineering, McGill University, Feb, 1966.

26. Roberts, D. E. A Spectroscopic Investigation of Combustion Driven Spherical Implosion Waves. UTIAS Tech. Note No.140, September 1969.

27. Benoit, A. Equilibrium Termodynamic Data for the H_2-O_2-He System UTIAS Tech. Note No.128, August 1968.

28. Watson, J. D. Implosion Driven Hypervelocity Launcher Performance Using Gaseous Detonation Waves. UTIAS Tech. Note No. 113, 1967.

29. Elsenaar, A. Microwave Measurements of Projectile Motion in the Barrel of the UTIAS Implosion-Driven Hypervelocity Launcher, UTIAS Tech. Note No. 145, 1969.

30. Bach, G. G.
Lee, J. H.

Initial Propagation of Impulsively Generated Converging Cylindrical and Spherical Shock Waves. Paper presented at the Canadian Congress of Applied Mechanics, Laval University, Quebec, Canada, May 1967.

NOTE: See also references after Appendix D.

APPENDIX A: Equations Used in the Program

To integrate Eqs.3.1 and 3.2 combined with Eqs. 3.3 and 3.4, in a finite difference scheme, the hemispherical chamber is divided into N zones (Fig.A-1). The boundaries of these zones are numbered from J = 1 at the outer wall till JLAST at the center, and using the properties at these boundaries accordingly. The properties inside a zone are characterized by $J-\frac{1}{2}$ or $J+\frac{1}{2}$, depending on which side of the interface is being considered. The mass is attached to an interface and it is composed of half of the mass of the adjacent zones. The subscript N refers to the time dependence. The location of each of the variables in the time-position space is shown in Fig.A-2. A set of centered difference equations is thereby obtained, with the exception of Q. Since Q is zero in nearly the entire flow field this situation is acceptable.

The difference equations can be written in the notation of the computer program (see Appendix B) as follows:

$$\text{DUDT} = (\text{PPLUS}_{J-\frac{1}{2}} - \text{PPLUS}_{J+\frac{1}{2}}) \cdot \text{ARFA}_J / (\text{HALFM}_{J-\frac{1}{2}} + \text{HALFM}_{J+\frac{1}{2}})$$

$$U_J^{N+\frac{1}{2}} = U_J^{N-\frac{1}{2}} + \text{DUDT} \cdot \text{DT2}$$

$$X_J^{N+3} = X_J^N + U_J^{N+\frac{1}{2}} \cdot \text{DT1}$$

$$R_J = \text{RADIUS} - X_J^{N+1} \qquad (R_J = \text{CUBRT}_J)$$

$$\text{AREA}_J = 2.\pi R_J^2$$

$$\text{VOLUM}_{J-\frac{1}{2}} = \frac{2}{3}\pi (R_{J-1}^3 - R_J^3)$$

$$V_{J-\frac{1}{2}}^{N+1} = \text{VOLUM}_{J-\frac{1}{2}} \cdot \text{ROZER}/2. \text{HALFM}_{J-\frac{1}{2}}$$

$$Q_{J-\frac{1}{2}} = \frac{C^2 \, (U_{J-1}^{N+\frac{1}{2}} - U_J^{N+\frac{1}{2}})^2 \cdot \text{ROZER}}{\frac{1}{2}(V_{J-\frac{1}{2}}^{N+1} + V_{J-\frac{1}{2}}^{N})} \quad \text{if } U_J^{N+\frac{1}{2}} < U_{J-1}^{N+\frac{1}{2}} \text{ and } F_{J-\frac{1}{2}}^{N+1} = 1$$

$$Q_{J-\frac{1}{2}} = 0 \quad \text{if } U_J^{N+\frac{1}{2}} \geq U_J^{N+\frac{1}{2}} \text{ or } F_{J-\frac{1}{2}}^{N+1} < 1$$

$F_{J-\frac{1}{2}}^{N+1} = (1-V_{J-\frac{1}{2}}^{N+1})/(1-V_{CJ})$; F can only increase till the value 1 is reached and remains unchanged afterwards.

$$E1 = E_{J-\frac{1}{2}}^N - (P_{J-\frac{1}{2}}^N + Q_{J-\frac{1}{2}}) \cdot (V_{J-\frac{1}{2}}^{N+1} - V_{J-\frac{1}{2}}^N)/\text{ROZER}$$

$P1 = P1\,(E1, V_{J-\frac{1}{2}}^N, V_{J-\frac{1}{2}}^{N+1})$ from the equation of state

$$E^{N+1}_{J-\frac{1}{2}} = E1 - (PI.F^{N+1}_{J-\frac{1}{2}} - P^{N}_{J-\frac{1}{2}}).(V^{N+1}_{J-\frac{1}{2}} - V^{N}_{J-\frac{1}{2}})/ ROZER$$

$$P1 = P1\ (E^{N+1}_{J-\frac{1}{2}}\ ,\ V^{N}_{J-\frac{1}{2}},\ V^{N+1}_{J-\frac{1}{2}})$$ from the equation of state

$$P^{N+1}_{J-\frac{1}{2}} = PI.\ F^{N+1}_{J-\frac{1}{2}}$$

$$PPLUS_{J-\frac{1}{2}} = P^{N+1}_{J-\frac{1}{2}} + Q_{J-\frac{1}{2}}$$

The basic variables (P,V and E) are now calculated and the square of the speed of sound, the temperature and the total energy follow from:

$$CSQ_{J-\frac{1}{2}} = (V^{N+1}_{J-\frac{1}{2}} / ROZER).\ \frac{PI + (\partial E/\partial V)}{(\partial E/\partial P)_V}$$

$$THETA_{J-\frac{1}{2}} = P^{N+1}_{J-\frac{1}{2}}\ \frac{V^{N+1}_{J-\frac{1}{2}}}{ROZER}\ \frac{M}{R}$$

$$EINT = \sum_J E^{N+1}_{J-\frac{1}{2}} . 2. HALFM_{J-\frac{1}{2}}/ROZER$$

$$EKIN = \sum_J \tfrac{1}{2} (U^{N+\frac{1}{2}}_J)^2 (HALFM_{J-\frac{1}{2}} + HALFM_{J+\frac{1}{2}})$$

$$ETOT = EINT + EKIN$$

We can now proceed with the next cycle after using the stability conditions to calculate the new time-step:

$$T1_{J-\frac{1}{2}} = (X^{N+1}_J - X^{N+1}_{J-1})/\sqrt{CSQ_{J-\frac{1}{2}}}$$

$$T2^2_{J-\frac{1}{2}} = \frac{1}{4.C^2} . (V^{N+1}_{J-\frac{1}{2}} + V^{N}_{J\ \frac{1}{2}})/(V^{N}_{J-\frac{1}{2}} - V^{N+1}_{J-\frac{1}{2}})$$

$$TMIN = \frac{1}{3} . \frac{1}{\sqrt{1/T1^2_{J-\frac{1}{2}} + 1/T2^2_{J-\frac{1}{2}}}}$$

If the previous time step was DTOLD then:

if TMIN < 1.1 DTOLD → DT1 = TMIN

if TMIN $\geq$ 1.1 DTOLD $\rightarrow$ DT1 = 1.1 DTOLD

DT2 = (DT1 + DTOLD) / 2

We can now calculate a new value of DUDT etc.

The equation of state for a stoichiometric mixture of oxygen and hydrogen is given by (Ref.11)

$$e = 6.57\ pv + \frac{974.0\ (pv)^2}{1140.0\ (pv)^4} + \alpha[0.101 \times 10^{-3} \ln \frac{p}{1.013.10\text{-}3} - 0.2325 \times 10^{-3}]$$

where, $\alpha = 0$ if $pv \leq 1.0465$

$= 8600\ pv - 9000$ if $1.0465 < pv \leq 3.488$

$= 21.0 \times 10^3$ if $3.488 < pv$

These data are valid in the region:

$0.01 < p < 1000$ bar

$1600 < T < 6000^{o}K$

APPENDIX B: Listing of the Computer Program

The computer program, written in Fortran IV consists of a MAIN program and 4 SUBROUTINES. Most of the basic calculations are performed in the MAIN program, the equations of which can be found in Appendix A. The SUBROUTINE SETUP reads the input data, calculates the zoning scheme and assigns the initial values. The SUBROUTINE STATE calculates the pressure and energy from its previous values and the new density, using the energy equation and the equation of state. The SUBROUTINE PROMO calculates the projectile motion by integrating the pressure at the origin over the barrel area. It can be left out without consequences for the remainder of the calculations. Finally the SUBROUTINE OUT is called for the output of the results after a specified time interval.

APPENDIX C: The Function f(z) in the W-C-C-Rule

The function f(z) in the W-C-C rule is given by (Ref.23):

$$f(z) = z^{1/\gamma}(z-1)\left(z+\frac{\gamma-1}{\gamma+1}\right)^{-\frac{1}{2}}\left[\frac{1+\left\{1+\frac{(\gamma+1)}{(\gamma-1)z}\right\}^{-1/2}}{1-\left\{1+\frac{(\gamma+1)}{(\gamma-1)z}\right\}^{-1/2}}\right]^{\sqrt{\{(\gamma/2(\gamma-1)\}}} \times$$

$$\times \left[\frac{\left\{1+\frac{(\gamma+1)}{(\gamma-1)z}\right\}^{-1/2}-\left(\frac{\gamma-1}{2\gamma}\right)^{1/2}}{\left\{1+\frac{(\gamma+1)}{(\gamma-1)z}\right\}+\left(\frac{\gamma-1}{2\gamma}\right)^{1/2}}\right] \times$$

$$\times \exp\left[\left(\frac{2}{\gamma-1}\right)^{1/2}\tan^{-1}\left\{\frac{2}{(\gamma-1)}\left(\frac{\gamma z}{z+\frac{\gamma+1}{\gamma-1}}\right)^{1/2}\right\}\right] \qquad (2.14)$$

APPENDIX D: Some Notes on the Guderley Solution

The problem of converging cylindrical and spherical shocks has drawn the attention of several authors (Ref. D-1,2,3,4,5,6). A very detailed solution was given in 1942 by Guderley (Ref.D-1). In this appendix we will discuss only briefly some of the most important features of this solution. Implosion waves unlike explosion waves are strongly dependent on the isentropic index γ. The complete solution takes into account not only the implosion but also the subsequent reflection from the center. Guderley presents his results for $\gamma = 1.4$. Later Somon et al (Ref.D-4) treated the case for $\gamma = 5/3$. Several authors calculated the similarity exponent n for different values of γ (Ref. D-3,5) and very recently this exponent was calculated for a wide range of values of γ (Ref. D-6). The determination of the similarity exponent is only part of the solution and in this Appendix the results of the implosion and the reflection are shown for $\gamma = 1.2$, 1.4, 5/3 and 3.

The equations of motion are:

$$\text{mass} \qquad \frac{\partial(\rho u)}{\partial r} + \frac{\partial \rho}{\partial t} + \frac{\alpha \rho u}{r} = 0 \qquad \text{(D-1a)}$$

$$\text{momentum} \qquad \frac{1}{\rho}\frac{\partial p}{\partial r} + u\frac{\partial u}{\partial r} + \frac{\partial u}{\partial t} = 0 \qquad \text{(D-1b)}$$

$$\text{energy} \qquad u\frac{\partial}{\partial r}(p/\rho^{\gamma}) + \frac{\partial}{\partial t}(p/\rho^{\gamma}) = 0 \qquad \text{(D-1c)}$$

α=2 for spherical geometry

α=1 for cylindrical geometry

They have to be supplemented with the shock wave relations or, for strong shocks, the usual approximations. For a sufficiently small neighbourhood of the origin (defined as the point r = 0, t = 0 in the r-t plane) are ρ_0, the initial density and r_s, the shock wave radius (a function of time), the characteristic parameters. There is in the implosion problem no characteristic energy as is the case in the explosion problem. Close to the origin the motion will therefore be self-similar, of the "second class" (Ref. D-7). The set of partial differential equations (Eqs. D-1) can be reduced to a set of ordinary differential equations with the similarity transformation:

$$\xi = \frac{r}{(\mp t)^n} \qquad \text{(D-2)}$$

(the -sign appears if $t < 0$, the + sign if $t > 0$).

From the strong-shock relations and from general similarity considerations it then follows that along a space-time parabola ξ = constant:

$$p \alpha r^{2-2/n} \qquad \text{(D-3a)}$$

$$\rho \alpha r^{0} \qquad \text{(D-3b)}$$

$$u \alpha r^{1-1/n} \qquad \text{(D-3c)}$$

Two new variables, obtained from a dimensional analysis are introduced:

$$\mu = \frac{a}{n\,\xi^{1/n}} \qquad \text{with} \quad a^2 = \frac{\gamma \cdot p}{\rho} \qquad \text{(D-4a)}$$

$$\nu = \mp \frac{u}{n\,\xi^{1/n}} \qquad \text{(D-4b)}$$

The set of equations, Eq.D-1 can now be reduced to a set of three ordinary differential equations with the four non-dimensional variables μ, ν, $\ln \xi$ and $\ln \rho$:

$$d\nu + (\nu-1)\, d \ln \rho + \nu(1+\alpha)\, d \ln \xi = 0 \qquad \text{(D-5a)}$$

$$\gamma(\nu-1)d\nu + 2\,\mu d\mu + \mu^2\, d \ln\rho + \left[2\,\mu^2 + \gamma\nu\left(\nu - \frac{1}{n}\right)\right] d \ln\xi = 0 \qquad \text{(D-5b)}$$

$$2(\nu-1)\, d\mu + \mu(1-\gamma)(\nu-1)\, d \ln\rho + 2\mu\left(\nu - \frac{1}{n}\right) d \ln\xi = 0 \qquad \text{(D-5c)}$$

Applying Cramer's rule to these equations yields one additional differential equation in μ and ν:

$$\frac{d\mu}{d\nu} = \frac{\mu}{2(\nu-1)} \; \frac{2\mu^2\left[\gamma(\nu-1)+\left(1-\frac{1}{n}\right)\right]+\gamma(\nu-1)\left[-(2+(\gamma-1)\alpha)\nu^2+\left(\frac{3-\gamma}{n}+\gamma+1+(\gamma-1)\alpha\right)\nu-\frac{2}{n}\right]}{\mu^2\left[\gamma\nu(1+\alpha)+2\left(1-\frac{1}{n}\right)\right]-\gamma\,\nu\,(\nu-1)\left(\nu-\frac{1}{n}\right)} \qquad \text{(D-6)}$$

The similarity exponent n is not yet determined. The relation between μ and ν can be determined from (Eq. D-6) for different values of n. It appears that only one of these integral curves has a physical significance. (The curve that passes through a singular point). If the proper value of n is determined, Eq. D-6 can be integrated starting at initial values of μ and ν given by the strong shock relations:

$$\mu = \frac{\sqrt{2\gamma(\gamma-1)}}{\gamma+1}, \qquad \nu = \frac{2}{\gamma+1}$$

These integral curves are shown in Fig. D-1 in the μ-ν-plane for different values of γ. If we follow the curve for $\gamma = 1.2$, the integration starts at the point A. When $t \to 0$, $\xi \to \infty$ and μ and $\nu \to 0$, one obtains point B. This point corresponds to the flow field at the time when the imploding shock wave has reached the origin. The flow away from the orgin ($r \neq 0$)

is not affected by this and we can continue the integration, for reason of continuity in the flow parameters, assuming a mirror reflection on the μ axis. However, the complete solution cannot be obtained from a continuation of the integration along the integral curve, since neither the position of the reflected shock nor its strength are known. We can determine for each set of values μ_1 and ν_1 on the integral curve (the points C_1, C_2, C_3 etc) a corresponding set of values μ_2 and ν_2 (the points C_1, C_2, C_3 etc) as if the shock was located at that position. We use therefore the normal shock wave relations since the shock is not necessarily strong.

$$\nu_2 - 1 = \frac{2}{\gamma+1} \frac{\mu_1^2}{\nu_1 - 1} + \frac{\gamma-1}{\gamma+1} (\nu_1 - 1)$$

$$\mu_2^2 = \mu_1^2 + \frac{\gamma-1}{2} [(\nu_1-1)^2 - (\nu_2-1)^2] \qquad \text{(D-8)}$$

To determine which set of values μ_1, ν_1, μ_2 and ν_2 corresponds to the actual occuring solution Eq. D-6 must be integrated starting at a known point of the flow field behind the reflected shock. For this point the origin is used ($r = 0$). At the origin the flow velocity remains zero. For $r = 0$, $\xi \to 0$ and μ and ν (see Eq. A-4) cannot be determined. Another transformation is therefore necessary, defined by:

$$\chi_3 = \frac{1}{\mu} \quad , \quad \chi_2 = \frac{\nu}{\mu} \qquad \text{(D-9)}$$

The equations D-5 and D-6 have to be transformed accordingly and the integral curve behind the reflected shock can now be determined, starting the integration at $\chi_2 = 0$ and $\chi_3 = 0$ and in the direction:

$$\frac{d\chi_2}{d\chi_3} = \frac{2(1/n-1)}{\gamma (1+\alpha)} \qquad \text{(D-10)}$$

(Another direction would yield a physical not-significant solution). The result is an integral curve in the χ_2-χ_3 plane as shown in Fig. D-2. The position of the shock can now be determined. For each of the values μ_2 and ν_2 (the points C' in Fig.D-1) the corresponding values of χ_2 and χ_3 can be determined with Eq. D-9 (the points C" in Fig. D-2). We thus obtain two integral curves in the χ_2-χ_3-plane, the intersection of which (the point C" in Fig. D-2) determines the value of μ and ν for the reflected shock. The solution is now completely determined in the μ-ν plane or the χ_2-χ_3 plane. The values for ρ and ξ follow from the integration of Eq. D-5 starting at the front of the imploding shock. At the reflected shock ξ is continuous and ρ follows from:

$$\frac{\rho_2}{\rho_1} = \frac{\nu_1 - 1}{\nu_2 - 1} \qquad \text{(A-11)}$$

Starting at the reflected shock the transformed Eqs. D-5 (with χ_2 and χ_3 as variables instead of μ and ν) are used for the integration behind the reflected shock in the direction of $\chi_2 = 0$ and $\chi_3 = 0$. The values for p and u follow from D-4a and D-4b. The integration is performed for $\gamma = 1.2$, 1.4,

5/3 and 3, for the case of a spherical shock wave. A fourth-order Runga-Kutta method is used for the integration of Eq. D-6. The value of ρ and ξ are determined from an integration by Simpson's rule. The integral curves in the μ-ν -plane are shown in Fig. D-1 and in the χ_2-χ_3 plane in Fig. D-2. Pressure, density and particle velocity are shown at a fixed location in space in Figs. D-3, D-4 and D-5 and compared with the planar reflection ($\alpha = 0$) respectively. Pressure, density, and velocity are normalized with respect to their value behind the imploding shock. The time is normalized with respect to the implosion time. The results for $\gamma = 1.4$ and $\gamma = 5/3$ are in good agreement with Ref. D-1 and Ref. D-4.

The implosion and reflection behaves qualitatively very similar for the different values of γ. As can be seen the imploding shock is followed by a period of adiabatic compression till the pressure and density is increased discontinuously by the reflected shock. The reflected shock reverses the flow direction and the pressure and density falls-off afterwards. Qualitatively we note a very strong dependence on γ. The pressures and densities that are obtained increase for a decreasing value of γ . For example, the overall pressure ratio is ~ 130 for $\gamma = 1.2$ but only ~ 5.5 for $\gamma = 3$. The overall density ratio is $\sim$ 190 for $\gamma = 1.2$ and ~ 2 for $\gamma = 3$. The velocity of the reflected shock, relative to the imploding shock increases for an increasing value of γ. The reflected shock is ~ 6.4 times slower as the imploding shock for $\gamma = 1.2$ but ~ 1.4 times faster for $\gamma = 3$. Another interesting feature is that for $\gamma = 1.2$ the reflected shock brings the gas almost at rest (as is the case of the planar wave). But for $\gamma = 3$, the gas in front of the reflected shock is almost at rest, and the reflected shock accelerates the flow away from the center. This will affect the pressure drop behind the reflected wave, which is much more pronounced for the higher values of γ. Finally, we will make a few remarks relavent to the parametric study of the UTIAS Implosion-Driven Hypervelocity Launcher performance (see Sec. 5.2).

From Eq. D-2, we have:

$$\xi = \left(\frac{r}{t^n} \right) \qquad \text{(D-2)}$$

For the shock, when ξ is constant we can write:

$$r_s = a_n (-t)^n \qquad \text{(D-12)}$$

if r_s is the shock radius, and a_n a constant.

The shock velocity follows from:

$$u_s = \frac{d\, r_s}{dt} = - n\, a_n^{1/n}\, r^{1-1/n} \qquad \text{(D-13)}$$

On a certain distance from the origin, say R_b, the barrel radius, $u_s = u_b$ and a_n follows from Eq. D-13:

$$a_n^{1/n} = - \frac{1}{n} \frac{u_b}{(R_b)^{1-1/n}} \qquad \text{(D-14)}$$

The time for the implosion is:

$$t^{**} = R_b^{1/n} / a_n^{1/n}$$

$$= - R_b^{1/n} \frac{n}{u_b} R_b^{1-1/n} \qquad \text{(D-15)}$$

$$= - n \frac{R_b}{u_b}$$

Since R_b/u_b represents the time the shock should move over the distance R_b if it had a constant velocity u_b, the similarity exponent n is a measure how much faster the spherical imploding shock moves as compared with the planar shock. The time t^{**} is used as the unit time in the Figs. D-3, D-4 and D-5 and is called the characteristic implosion time (see Eq. 5.11). We can also integrate the pressures obtained from the strong shock solution over an area at the origin with radius R_b to calculate the total impulse set at the origin. This average pressure will always remain finite since the pressure increases as $r^{-\delta}$ ($\delta < 2$) but the area over which this pressure acts decreases as r^2. For the same reason the maximum of the average pressure, obtained as the reflected shock passes the radius R_b will remain finite. This means that the fine detail of the implosion for very small values of r is not very important with respect to the integrated pressure. In Fig. D-3 the pressure behind the imploding shock, p_b, and the implosion time, t^{**}, are used as characteristic dimensions. The integral of p.dt and the total impulse will therefore be proportional to $p_b.t^{**}$. This relation used in Eq. 5.12.

TABLE D-1 Values of n and δ for Spherical Shocks (Ref. D-6)

γ	n	δ
1.2	0.7571	0.6415
1.4	0.7172	0.7887
5/3	0.6884	0.9054
3	0.6364	1.1426

REFERENCES APPENDIX D:

D-1. Guderley, G. — Strong Spherical and Cylindrical Shock Waves in the Neighbourhood of the Center of a Sphere or the Axis of a Cylinder, Luftfahrtforschung, Vol.19, No.9, 1942.

D-2. Stanyukovich, K. P. — Unsteady Motion of Continuous Media, Pergamon Press, New York, 1960.

D-3. Butler, D. S. — Converging Spherical and Cylindrical Shocks, Armament Research Development Establishment, Report 54/54. 1954.

D-4. Somon, J. P. et al. — Contribution a la Theory des Chocs Convergents dans un Plasma, Nuclear Fusion: 1962 Supplement, Part 2.

D-5. Flagg, R. F. — The Application of Implosion Wave Dynamics to a Hypervelocity Launcher, UTIAS Report No. 125, 1967.

D-6. Goresh, J. W. Fettis, H. E. — Unpublished work of Aerospace Research Laboratories, Wright-Patterson Air Force Base, Ohio, 1968.

D-7. Zel'dovich, Ya. B. Raizer, Yu, P. — Physics of Shock Waves and High-Temperature Hydrodynamic Phenomena, Vol. II, Academic Press, 1967.

FIGURES APPENDIX D:

1. OUTGOING DETONATION WAVE

2. DETONATION WAVE REFLECTS AS SHOCK WAVE (INITIATES LINER, IF USED)

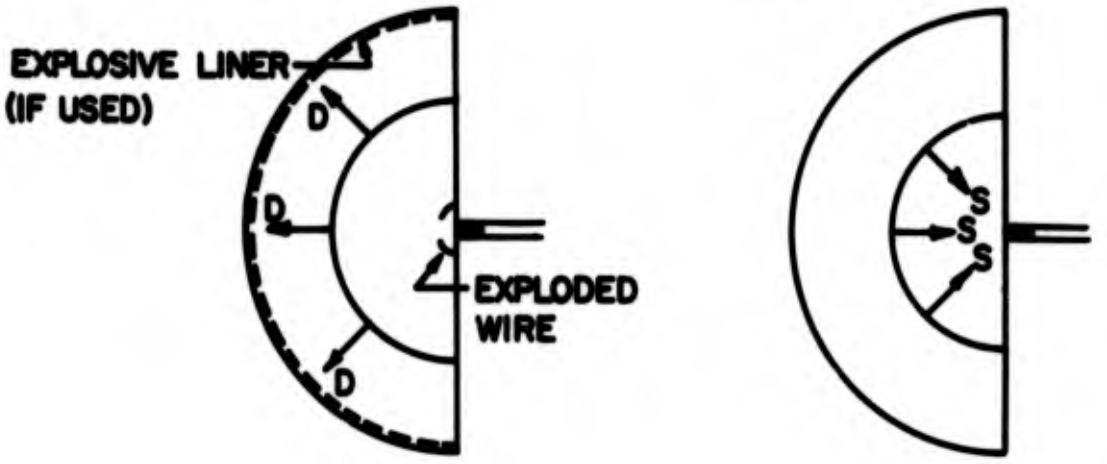

3. MAIN SHOCK CONVERGES ON ORIGIN, BECOMING VERY STRONG

4. SHOCK WAVE REFLECTS ON ORIGIN AND MOVES OUT AGAIN

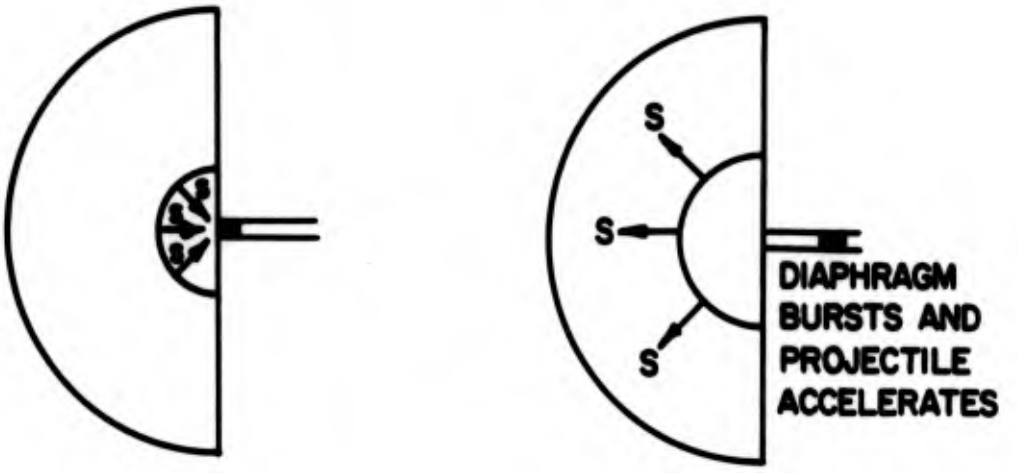

FIG. 1 SCHEMATIC OF IMPLOSION CHAMBER WAVE DYNAMICS (REPRODUCED FROM REF. 1)

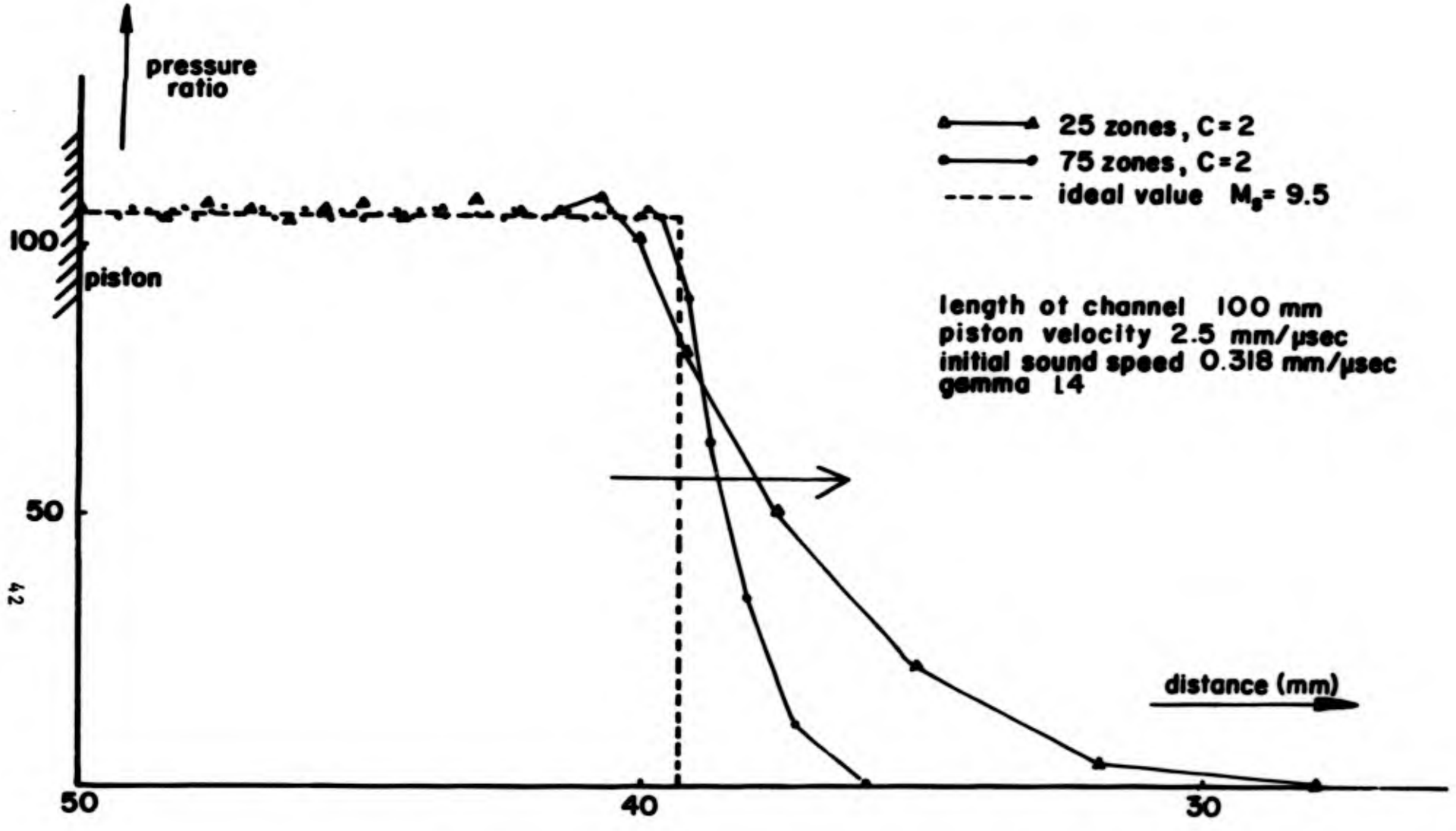

FIGURE 2 FLOW IN FRONT OF A PLANAR PISTON – PRESSURE PROFILES FOR A DIFFERENT NUMBER OF ZONES AFTER 20 μsec

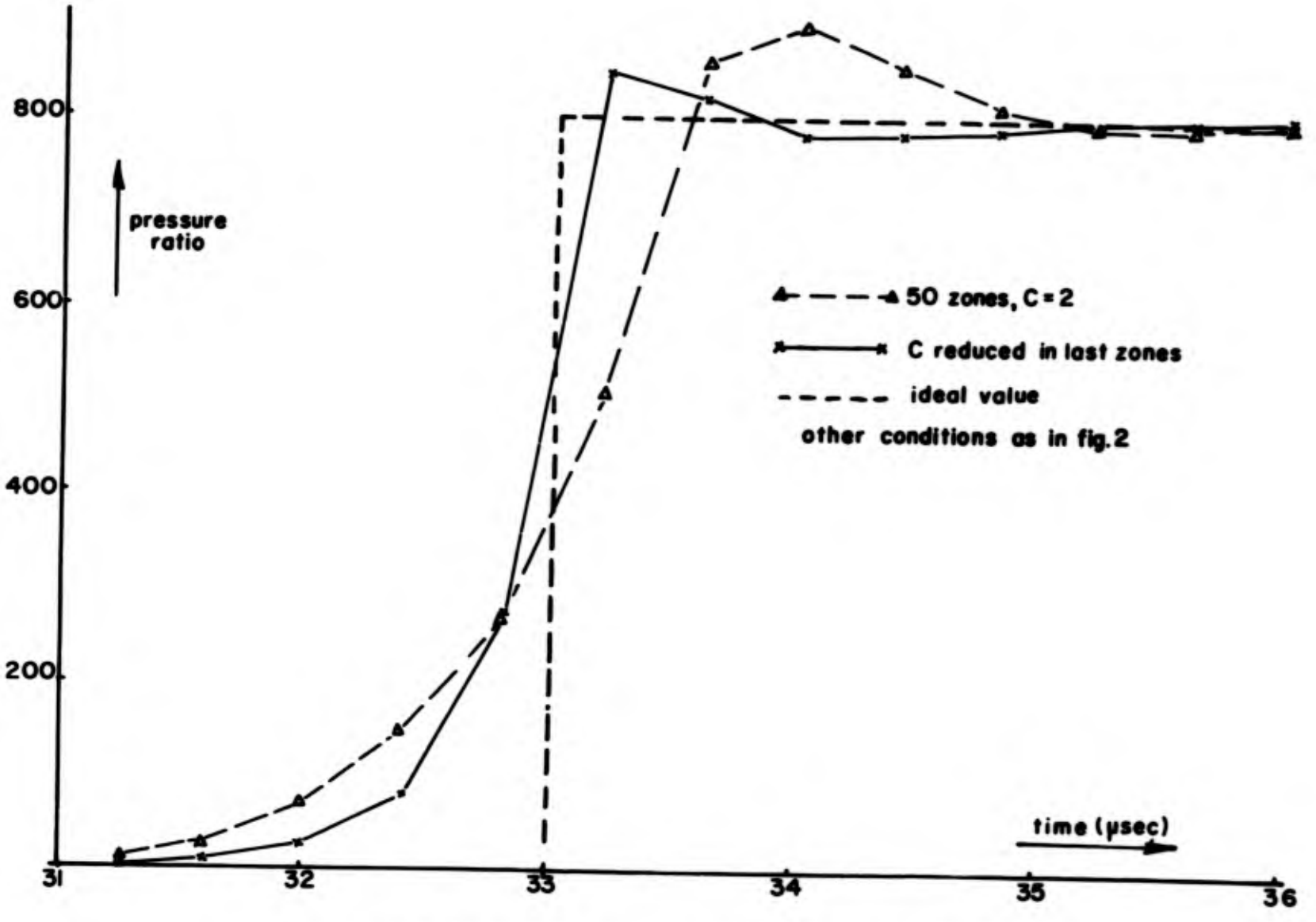

FIGURE 3 PLANAR PISTON CONT. - PRESSURE AT THE END OF THE CHANNEL DURING THE REFLECTION

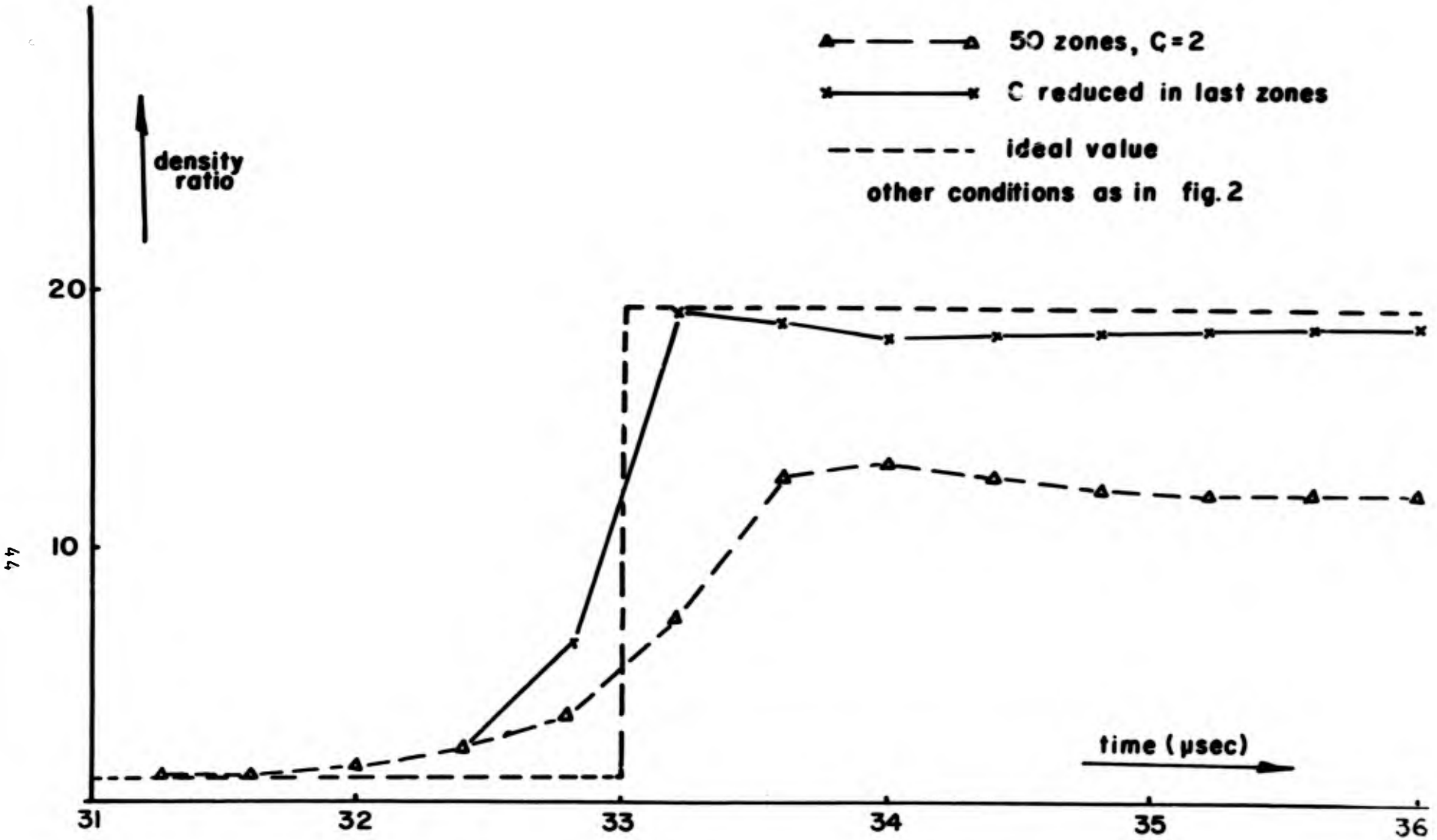

FIGURE 4 PLANAR PISTON CONT. - DENSITY AT THE END OF THE CHANNEL DURING THE REFLECTION

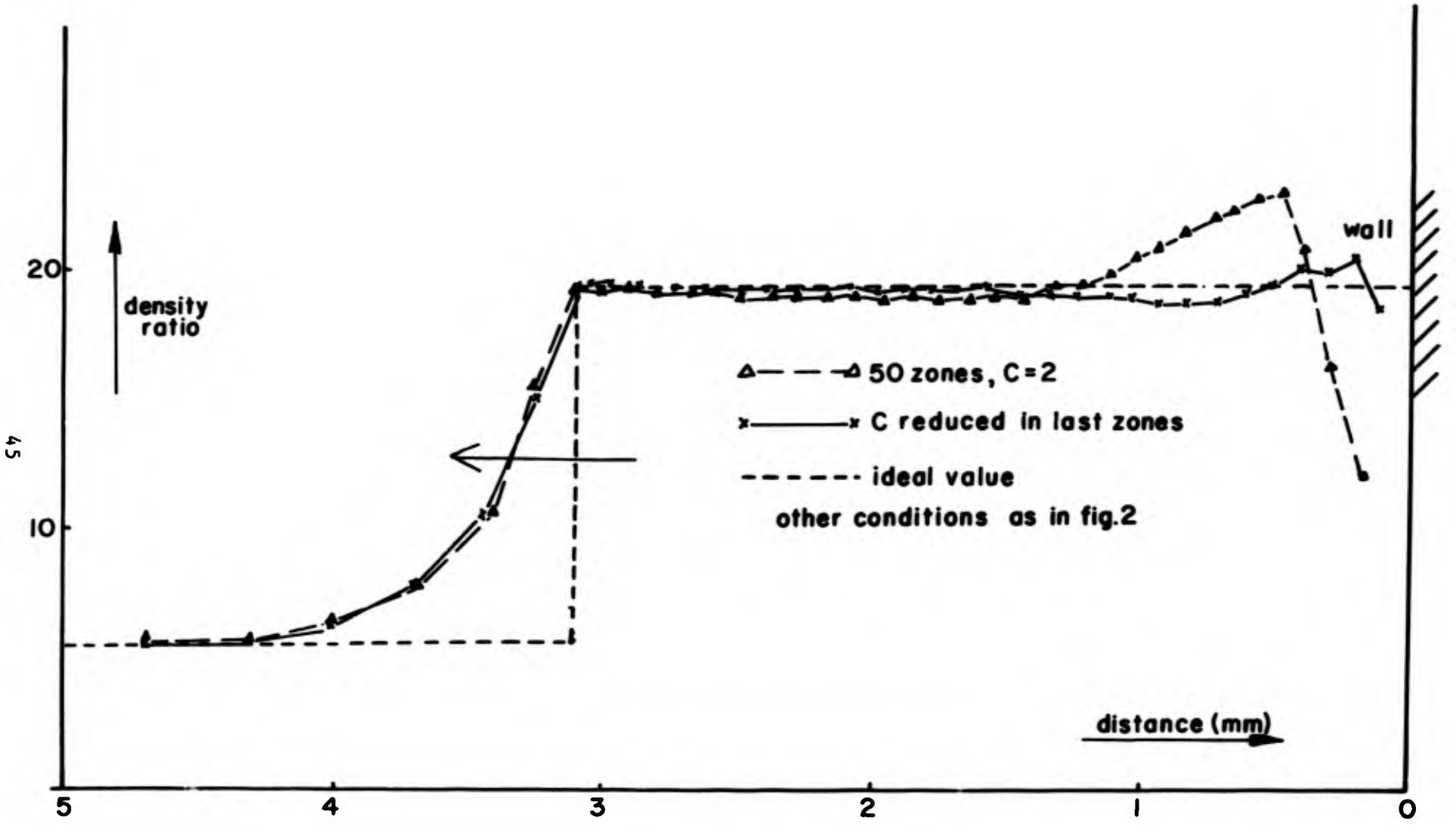

FIGURE 5 PLANAR PISTON CONT. - DENSITY BEHIND THE REFLECTED SHOCKWAVE AFTER 36 μsec

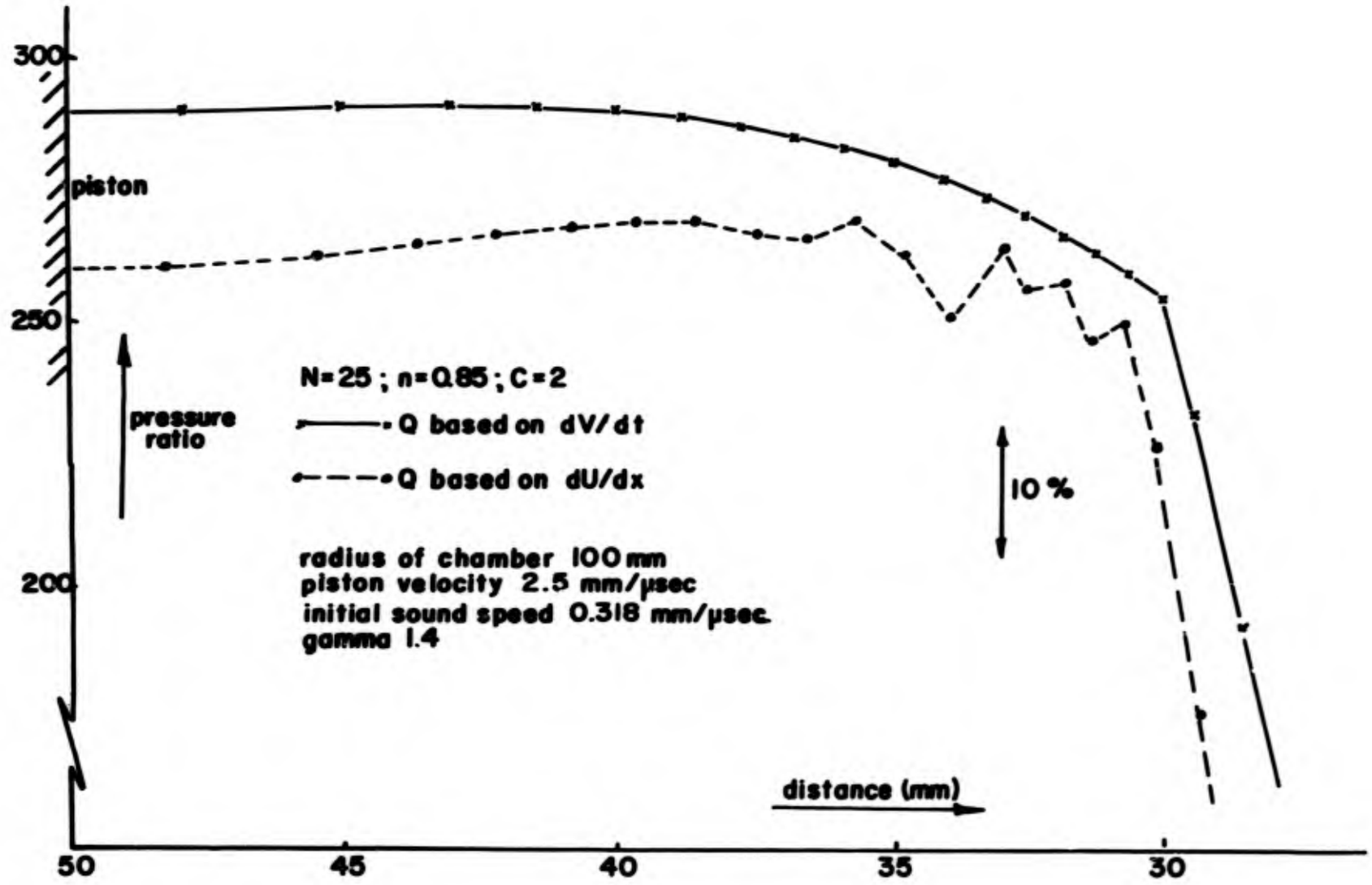

FIGURE 6 FLOW IN FRONT OF A SPHERICAL IMPLODING PISTON AFTER 20 μsec
THE INFLUENCE OF DIFFERENT FORMS OF Q

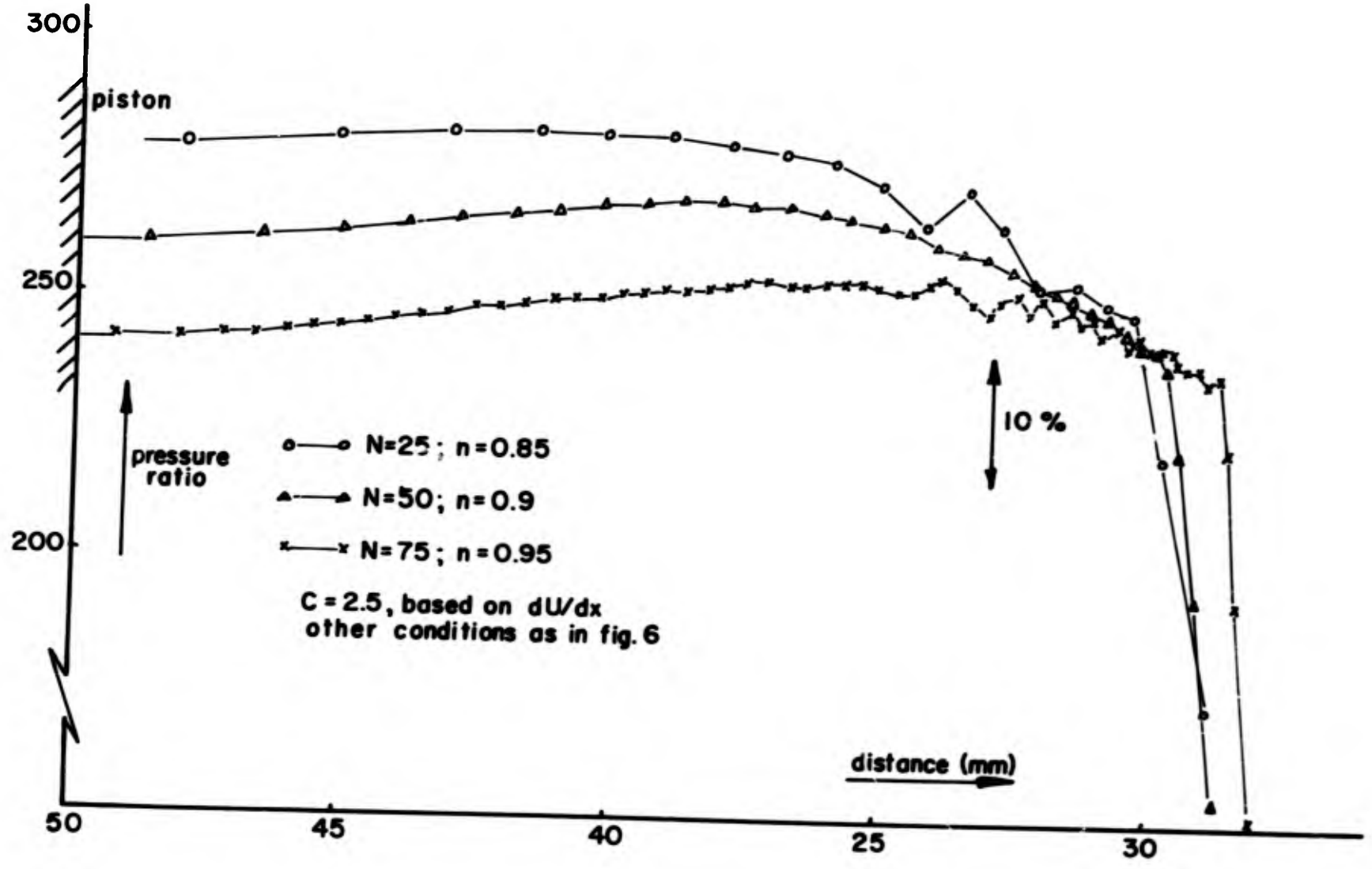

FIGURE 7 SPHERICAL PISTON CONT. - THE INFLUENCE OF THE NUMBER OF ZONES FOR C=2.5

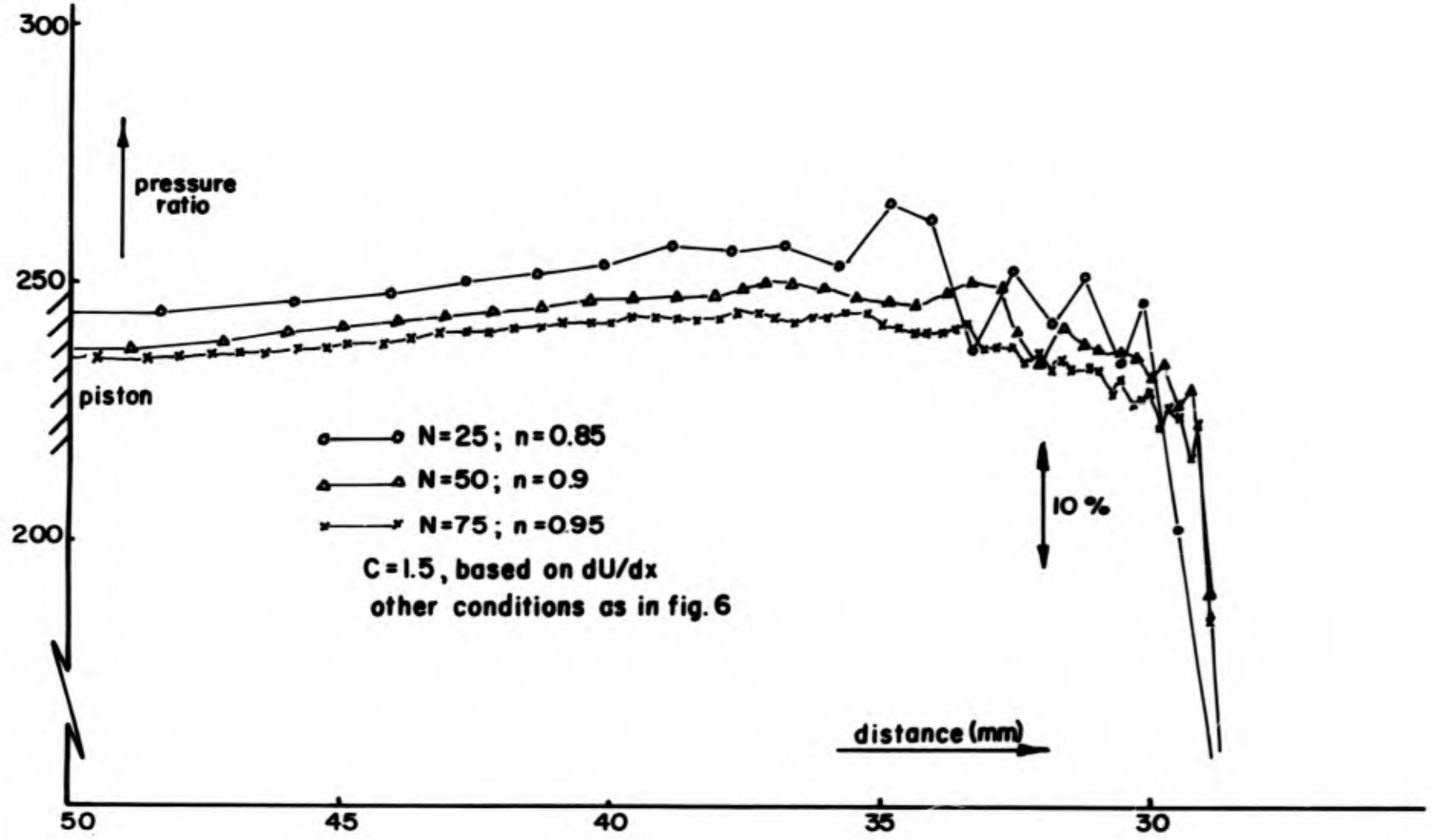

FIGURE 8 SPHERICAL PISTON CONT. - THE INFLUENCE OF THE NUMBER OF ZONES FOR C=1.5

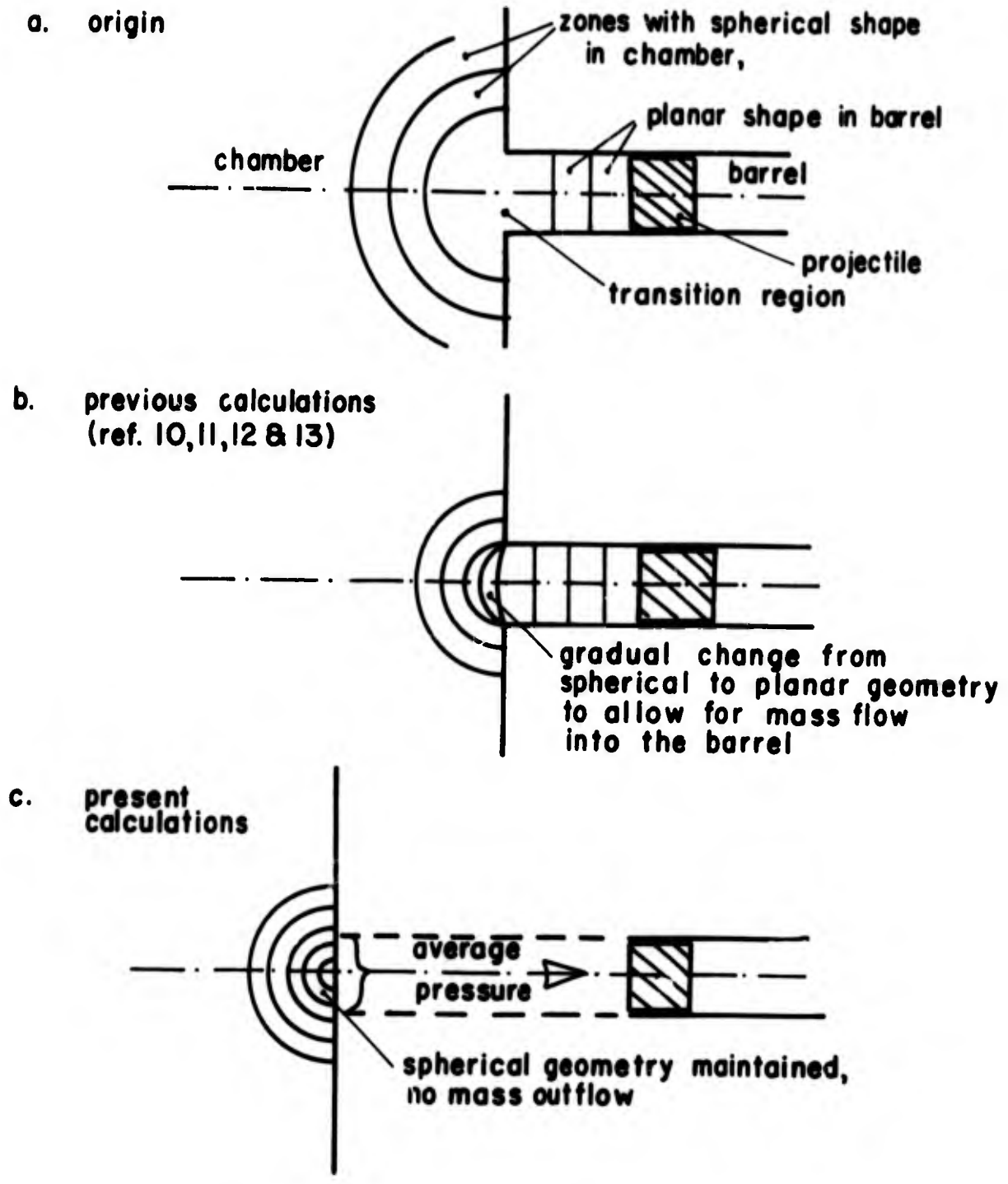

FIGURE 9 SCHEMATIC OF THE NUMERICAL TREATMENT AT THE ORIGIN

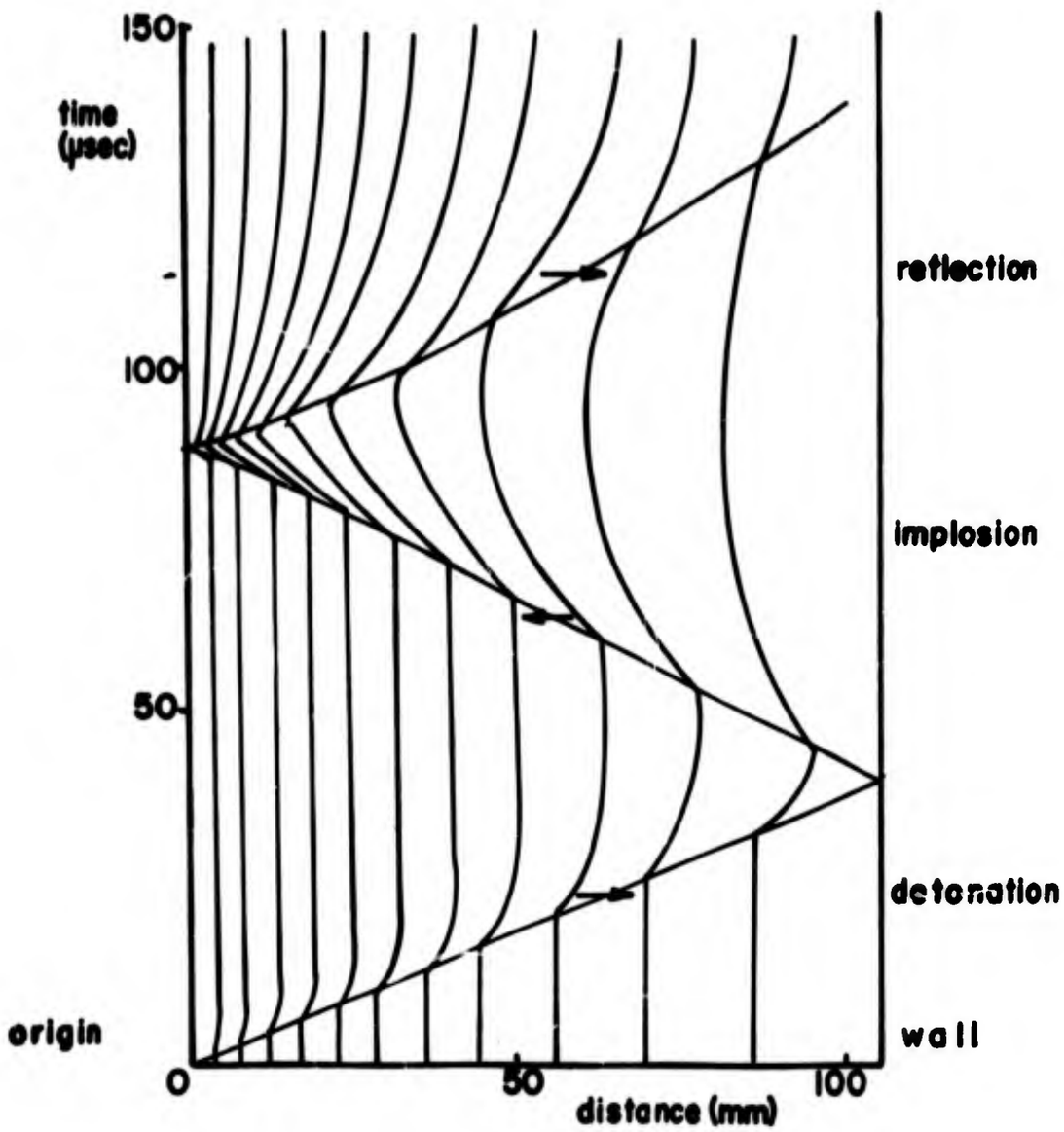

FIGURE 10 X-t DIAGRAM AND PARTICLE PATHS FOR A COMBUSTION DRIVEN SPHERICAL IMPLOSION WAVE (200 psi $2H_2 + O_2$)

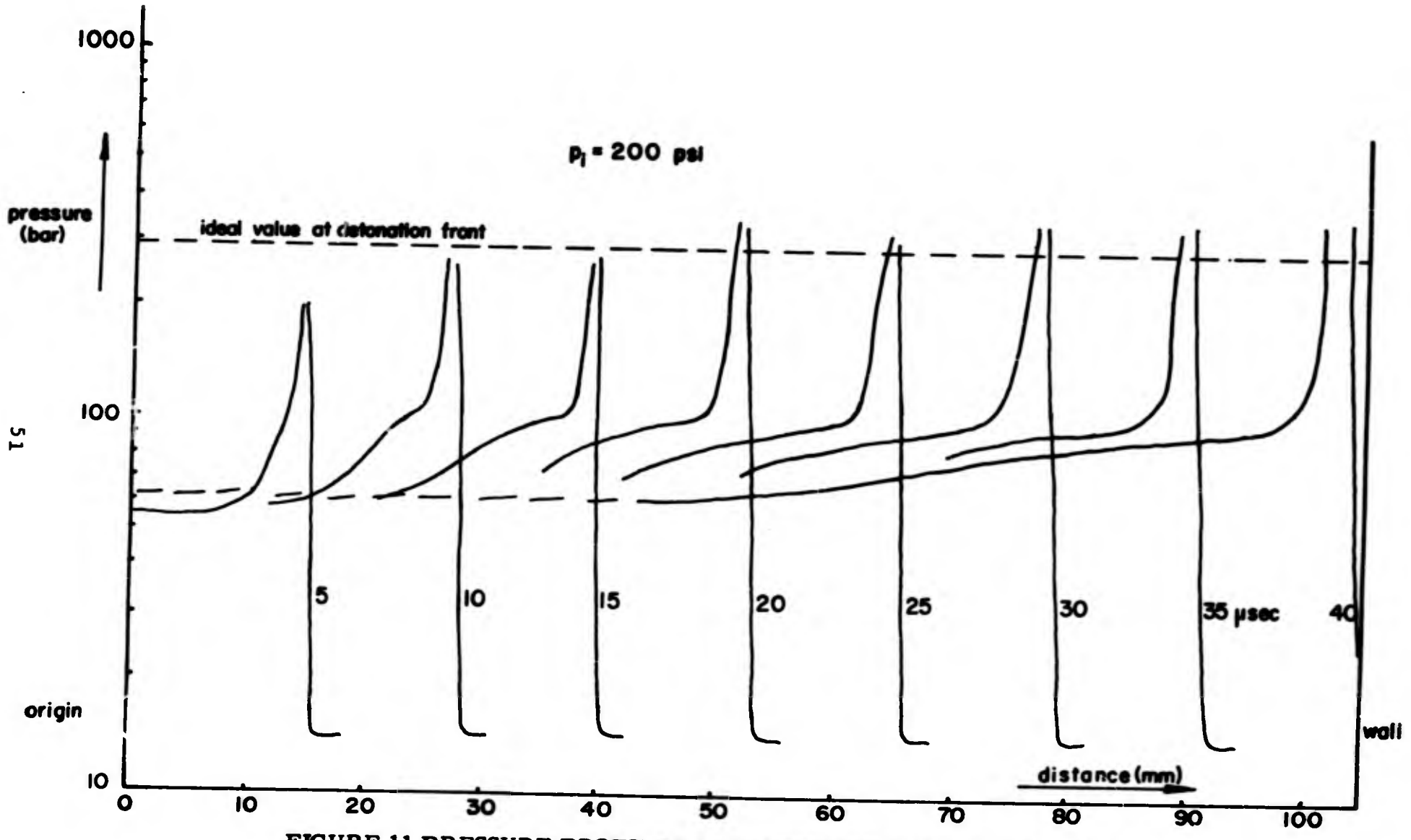

FIGURE 11 PRESSURE PROFILES AT DIFFERENT INSTANTS OF TIME FOR THE DETONATION WAVE

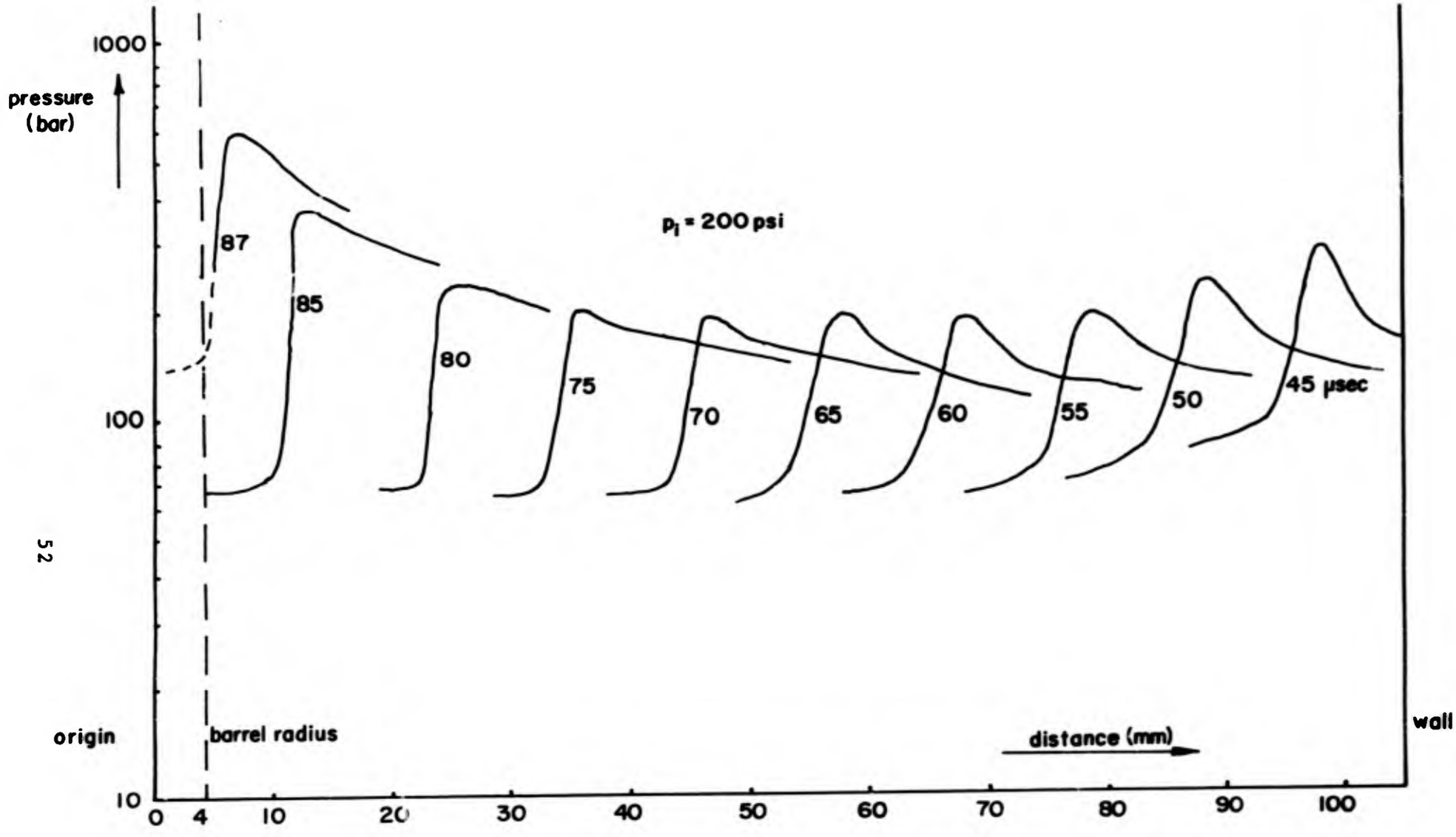

FIGURE 12 PRESSURE PROFILE AT DIFFERENT INSTANTS OF TIME FOR THE IMPLOSION WAVE

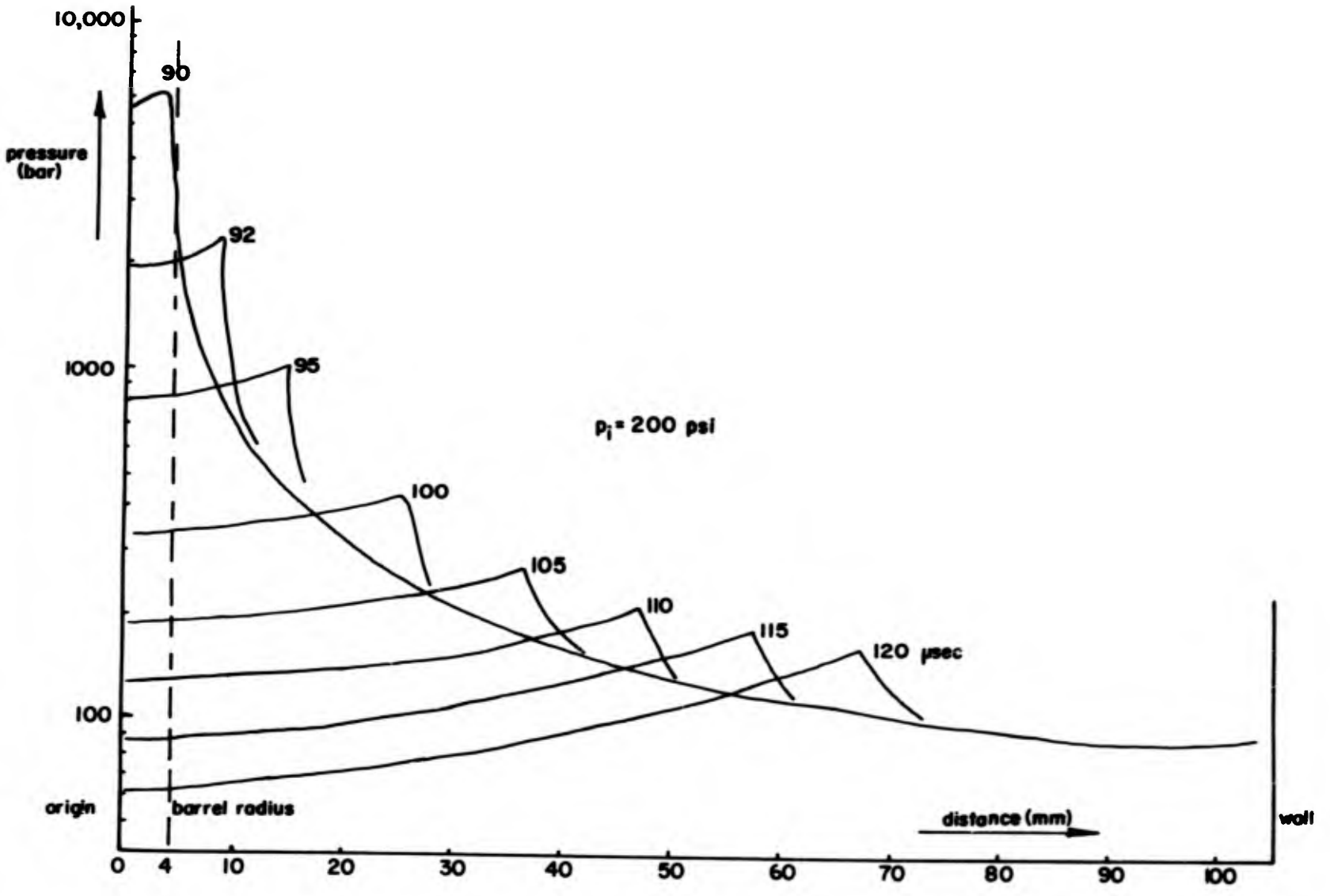

FIGURE 13 PRESSURE PROFILES AT DIFFERENT INSTANTS OF TIME FOR THE REFLECTED WAVE

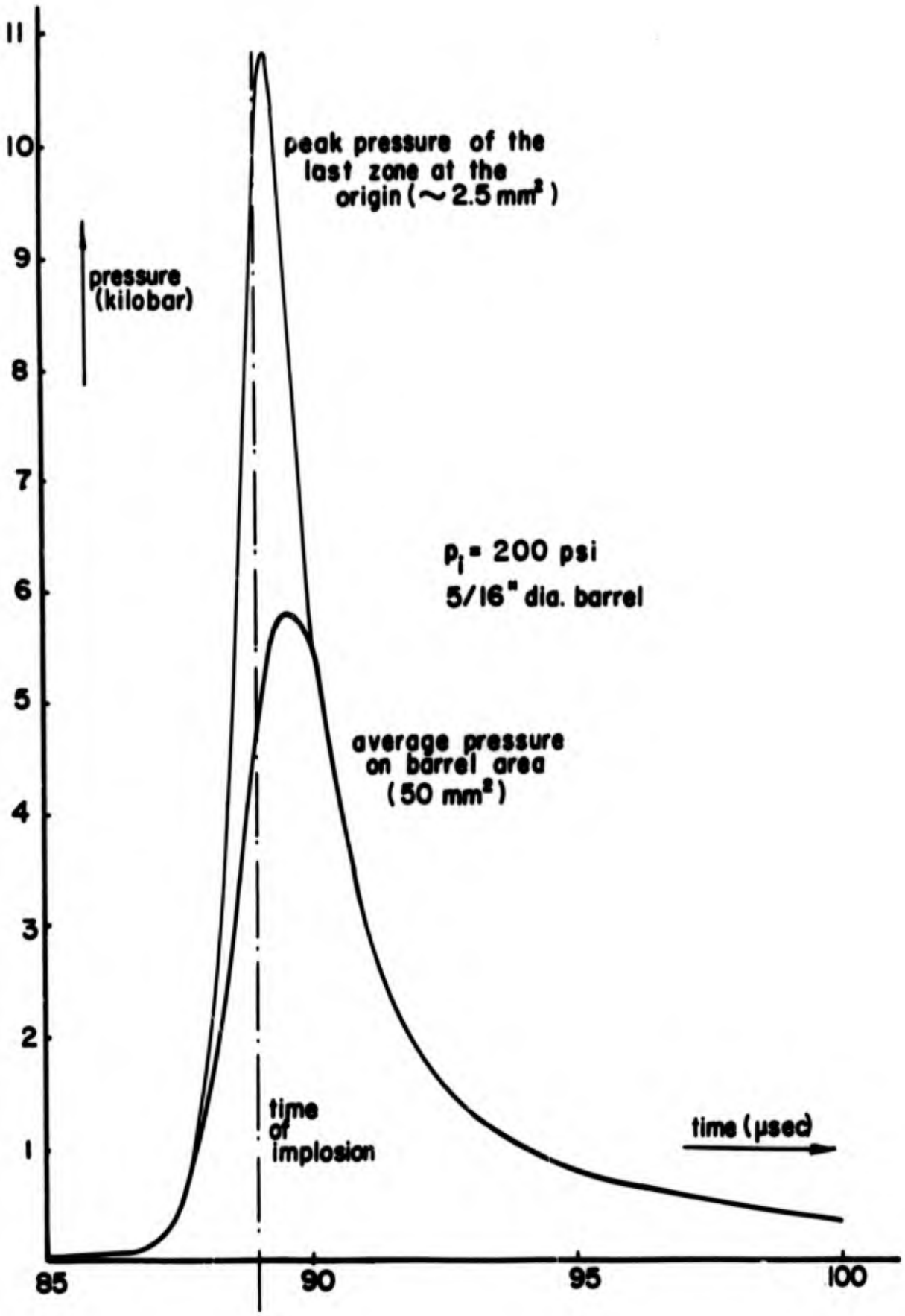

FIGURE 14 'PEAK' PRESSURE AND AVERAGE PRESSURE AT THE ORIGIN

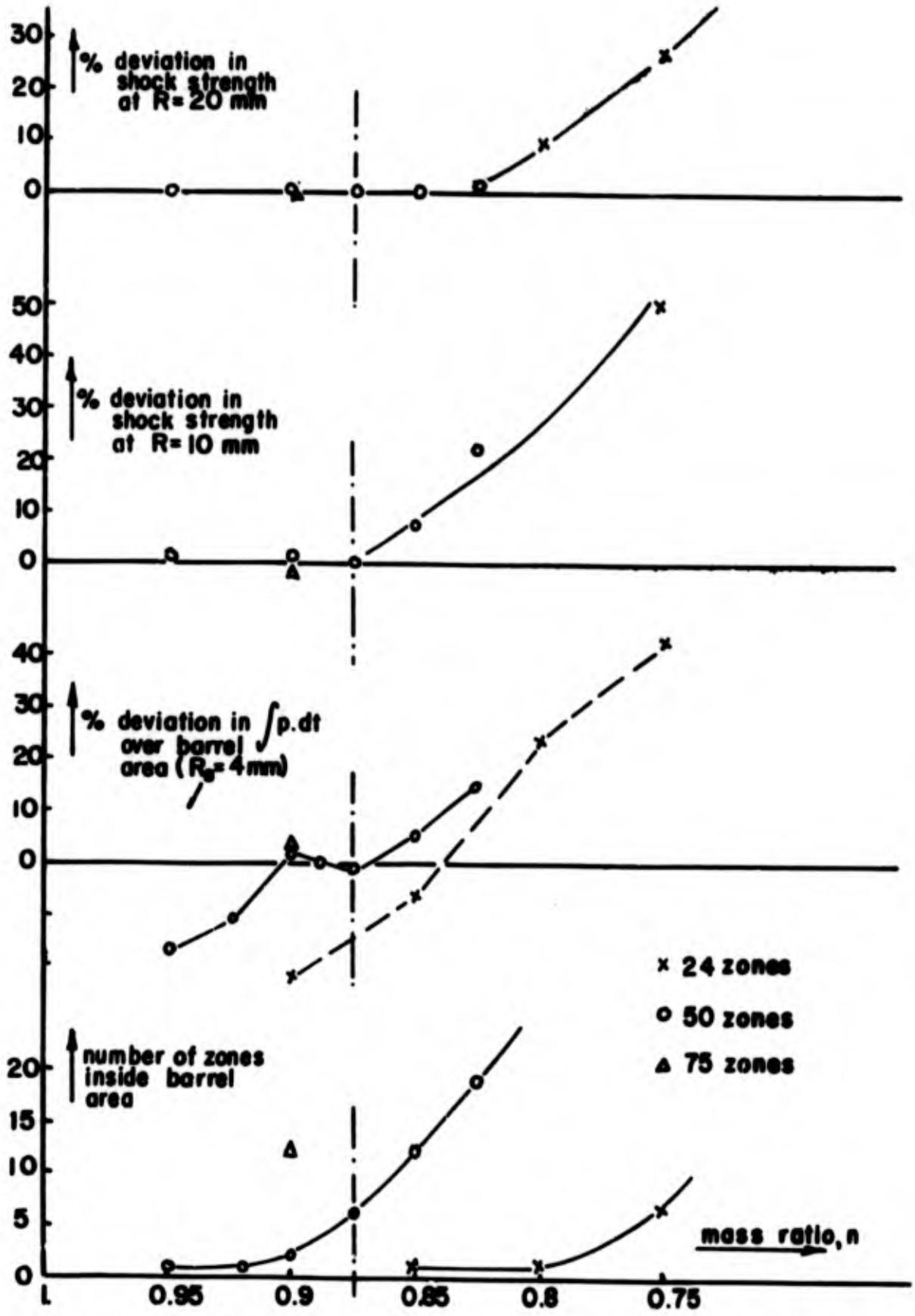

FIGURE 15 INFLUENCE OF ORIGINAL ZONING WITH RESPECT TO CONVERGENCE

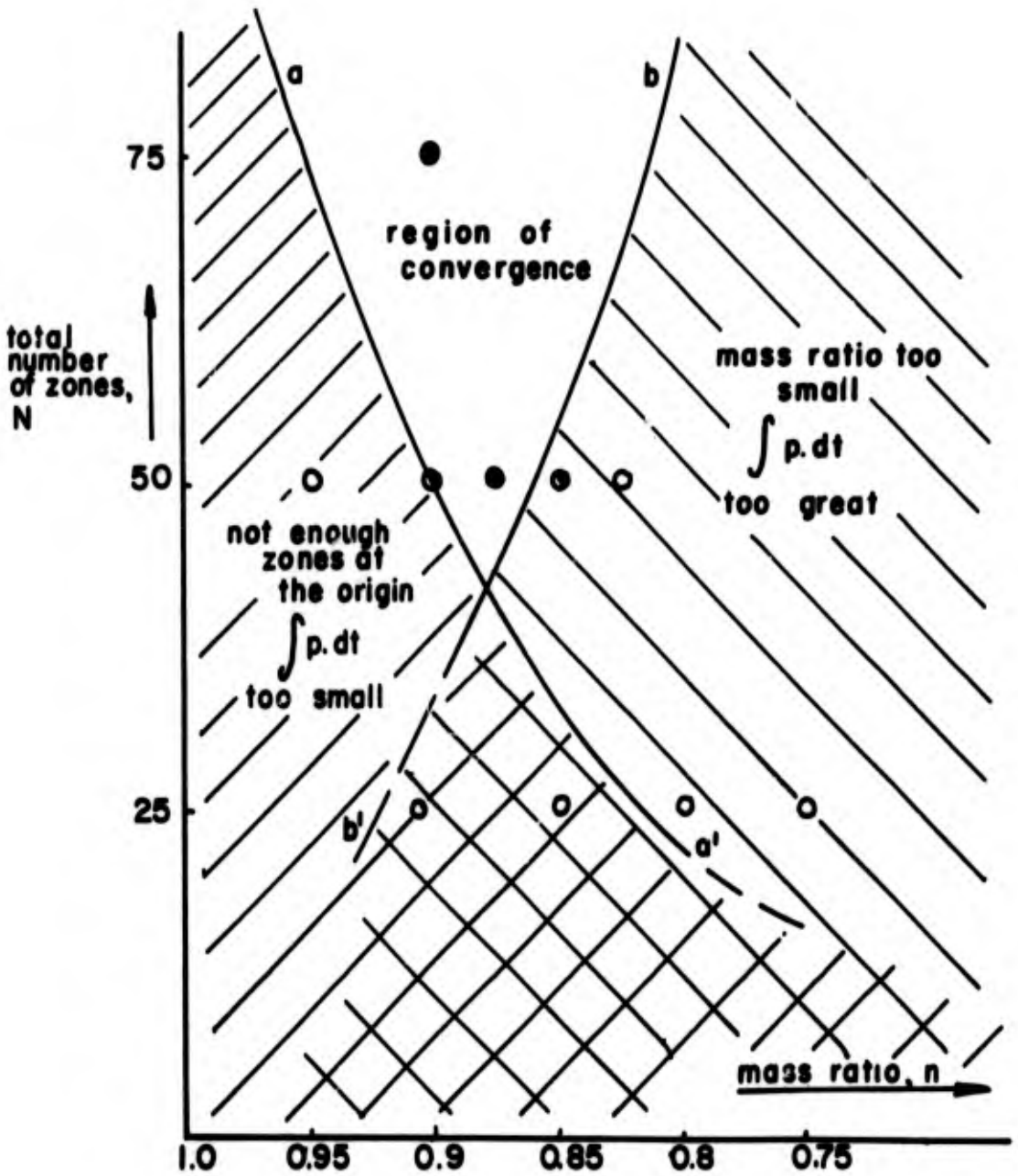

FIGURE 16 REGION OF CONVERGENCE IN THE NUMERICAL CALCULATIONS

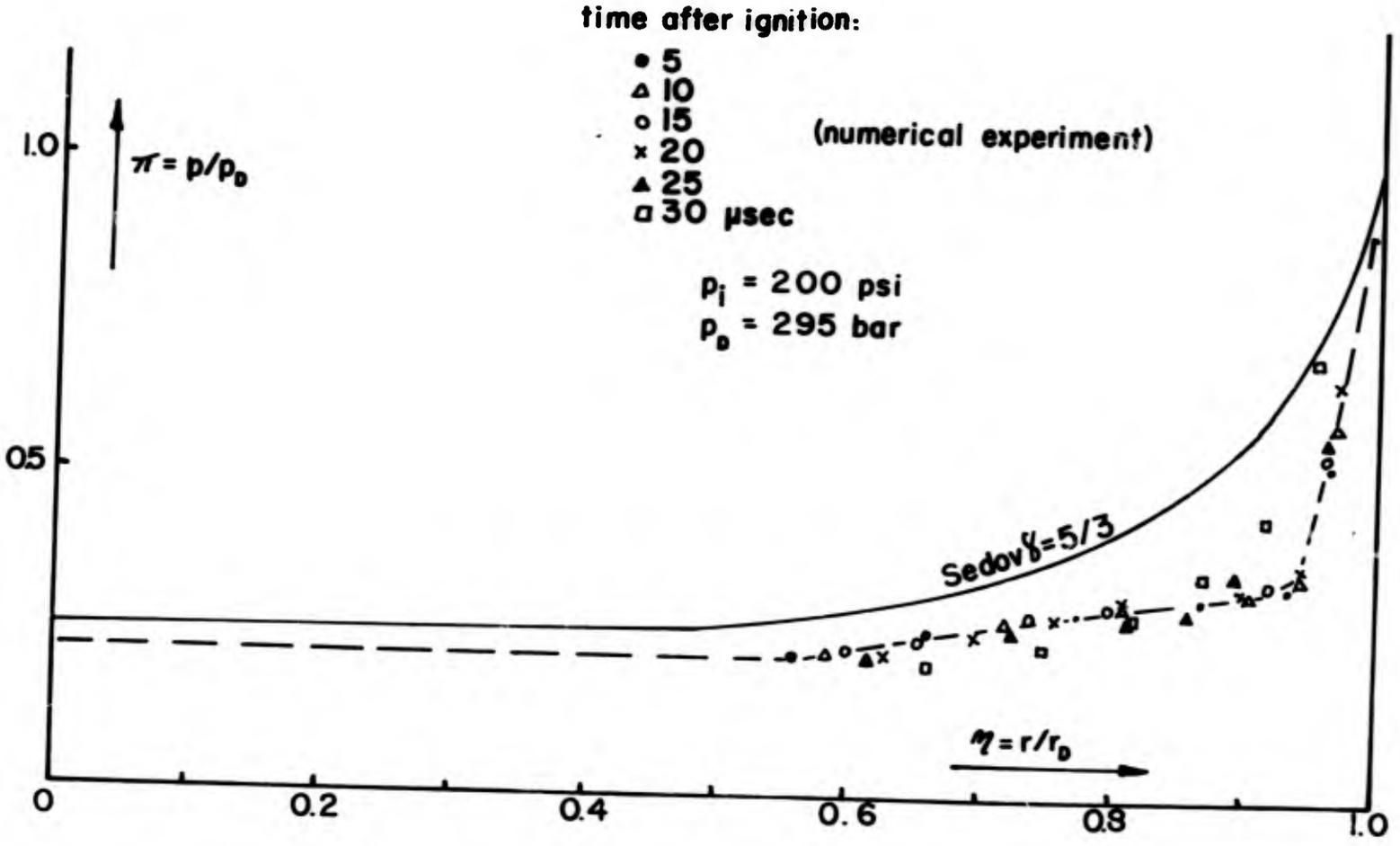

FIGURE 17 SELF-SIMILAR PRESSURE PROFILES FOR THE DETONATION

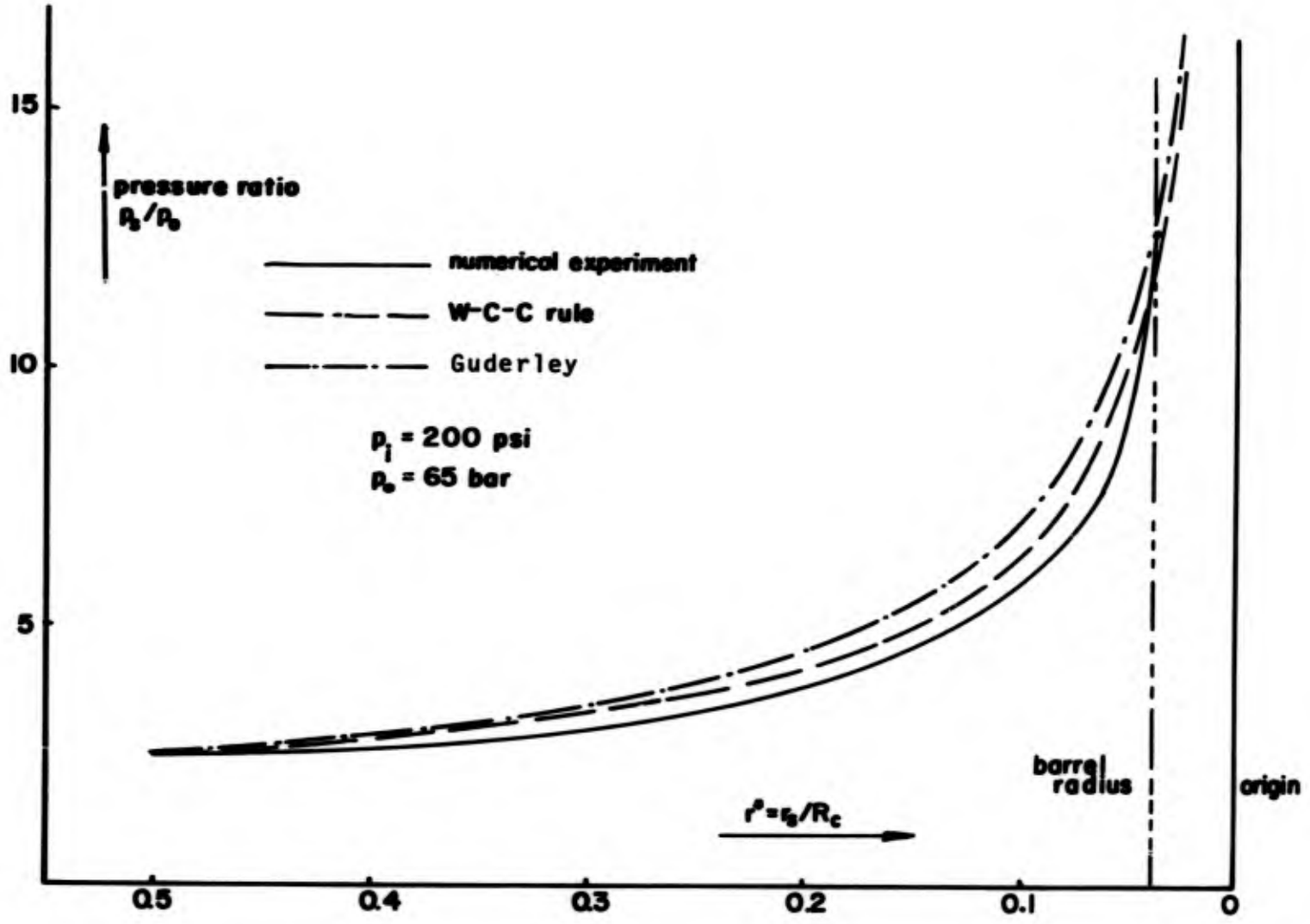

FIGURE 18 COMPARISON OF THE PRESSURE RATIO OF THE IMPLODING SHOCK WITH SOME ANALYTICAL SOLUTIONS

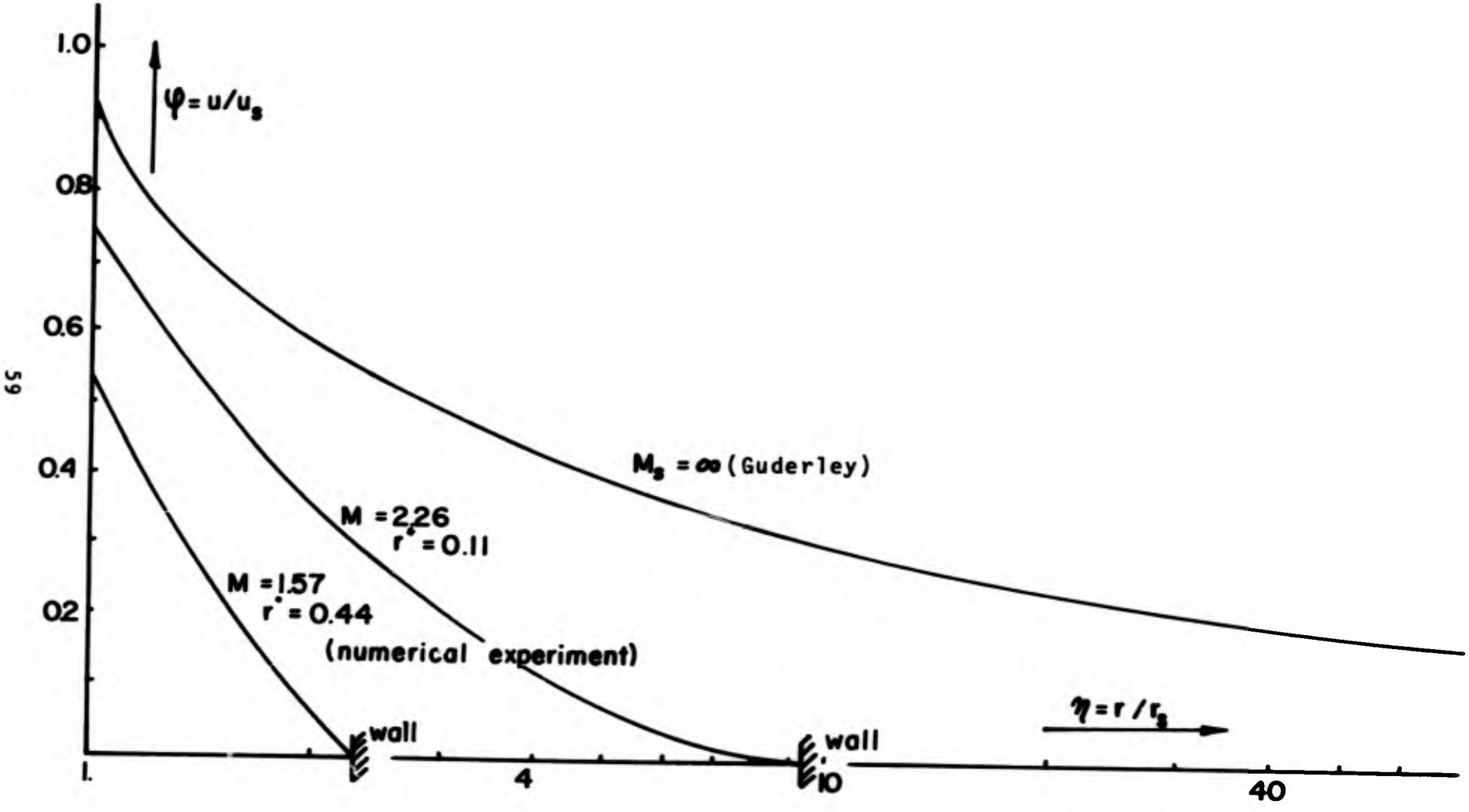

FIGURE 19 COMPARISON OF THE VELOCITY BEHIND THE IMPLODING SHOCK WITH THE STRONG SHOCK SOLUTION

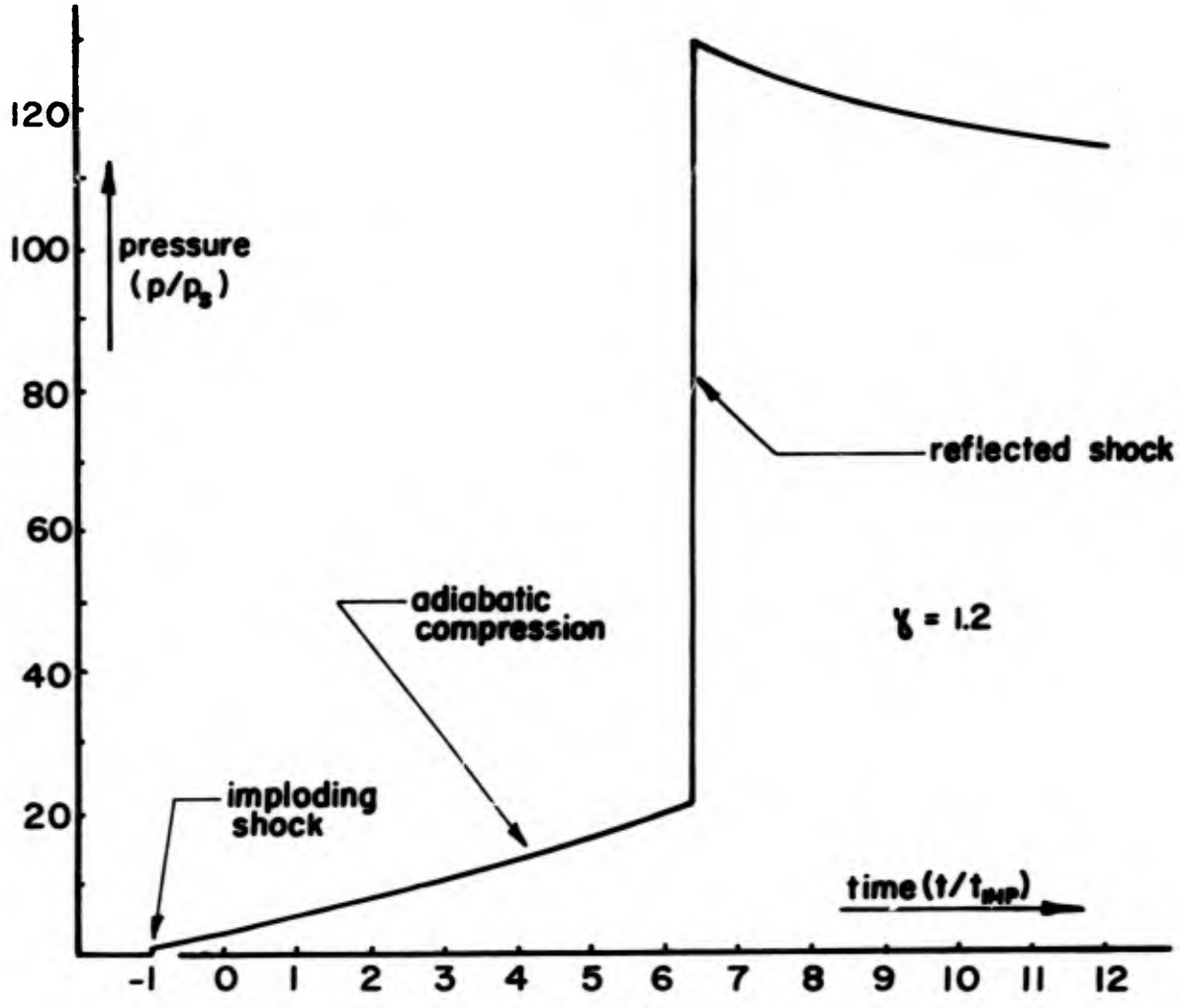

FIGURE 20 PRESSURE AT A FIXED DISTANCE FROM THE ORIGIN FOR THE STRONG SHOCK SOLUTION ($\gamma = 1.2$)

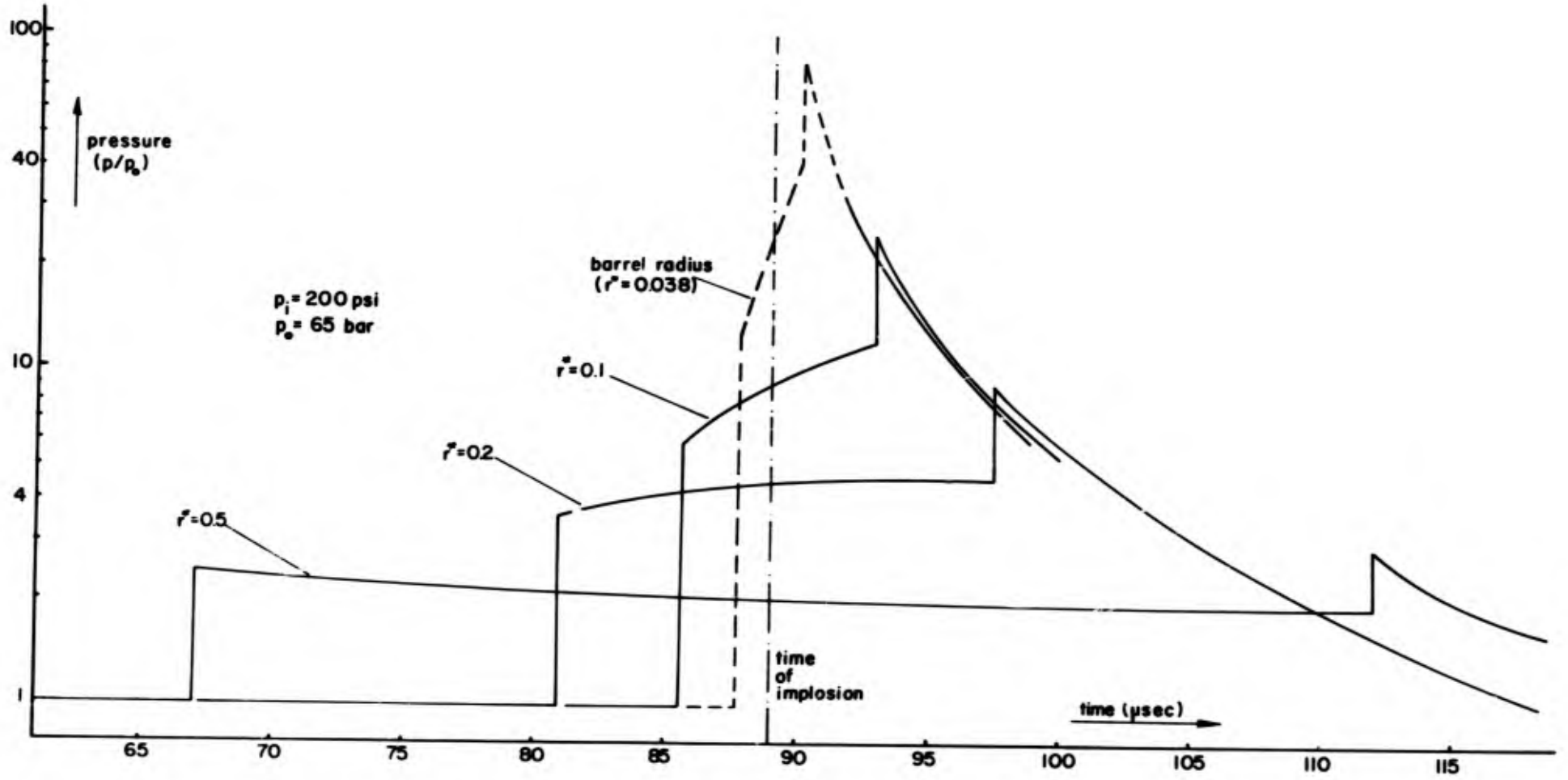

FIGURE 21 PRESSURE PROFILES AT DIFFERENT LOCATIONS IN THE NUMERICAL EXPERIMENT

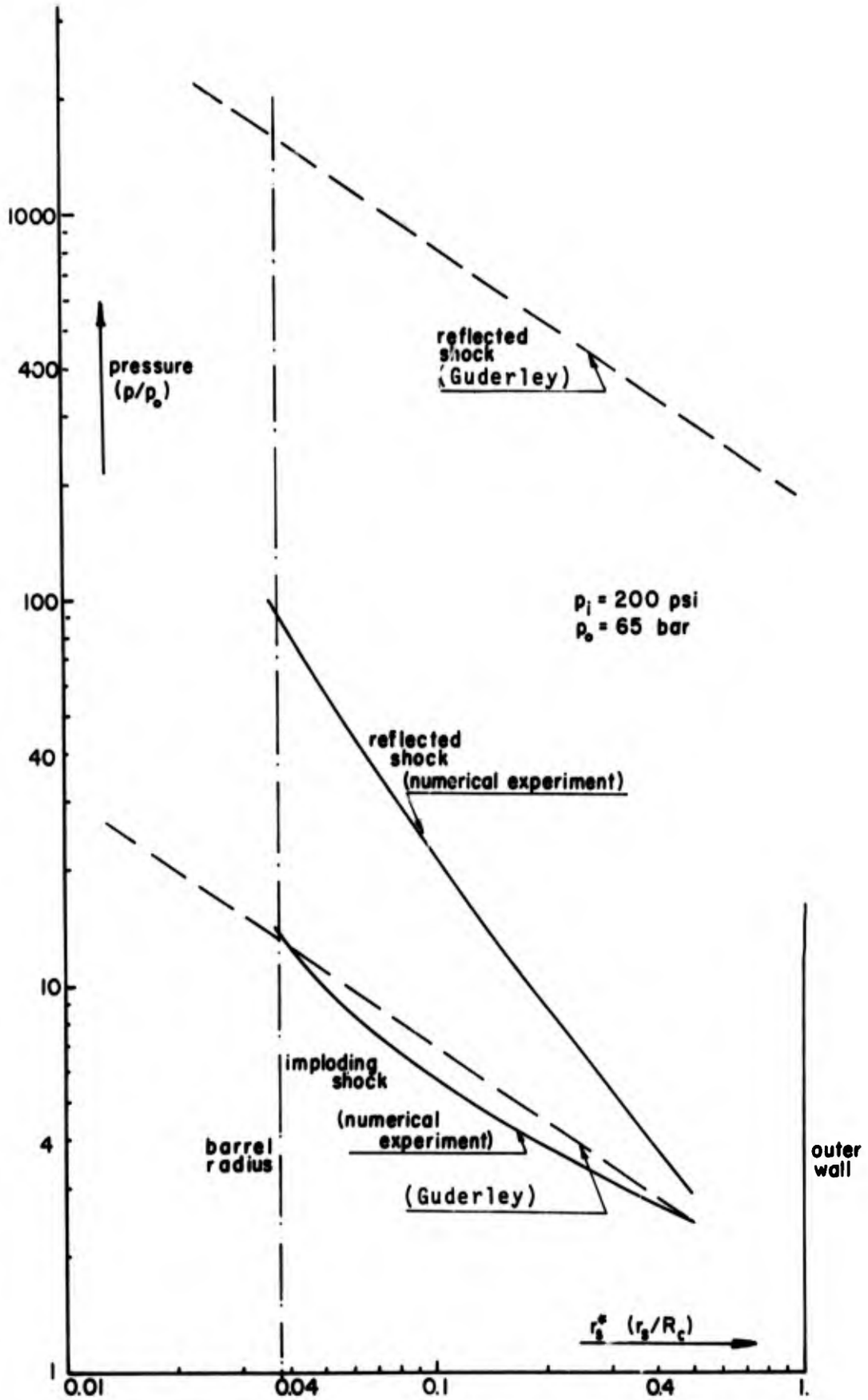

FIGURE 22 COMPARISON OF THE PRESSURE BEHIND THE IMPLODING AND REFLECTED SHOCK WITH THE STRONG SHOCK SOLUTION

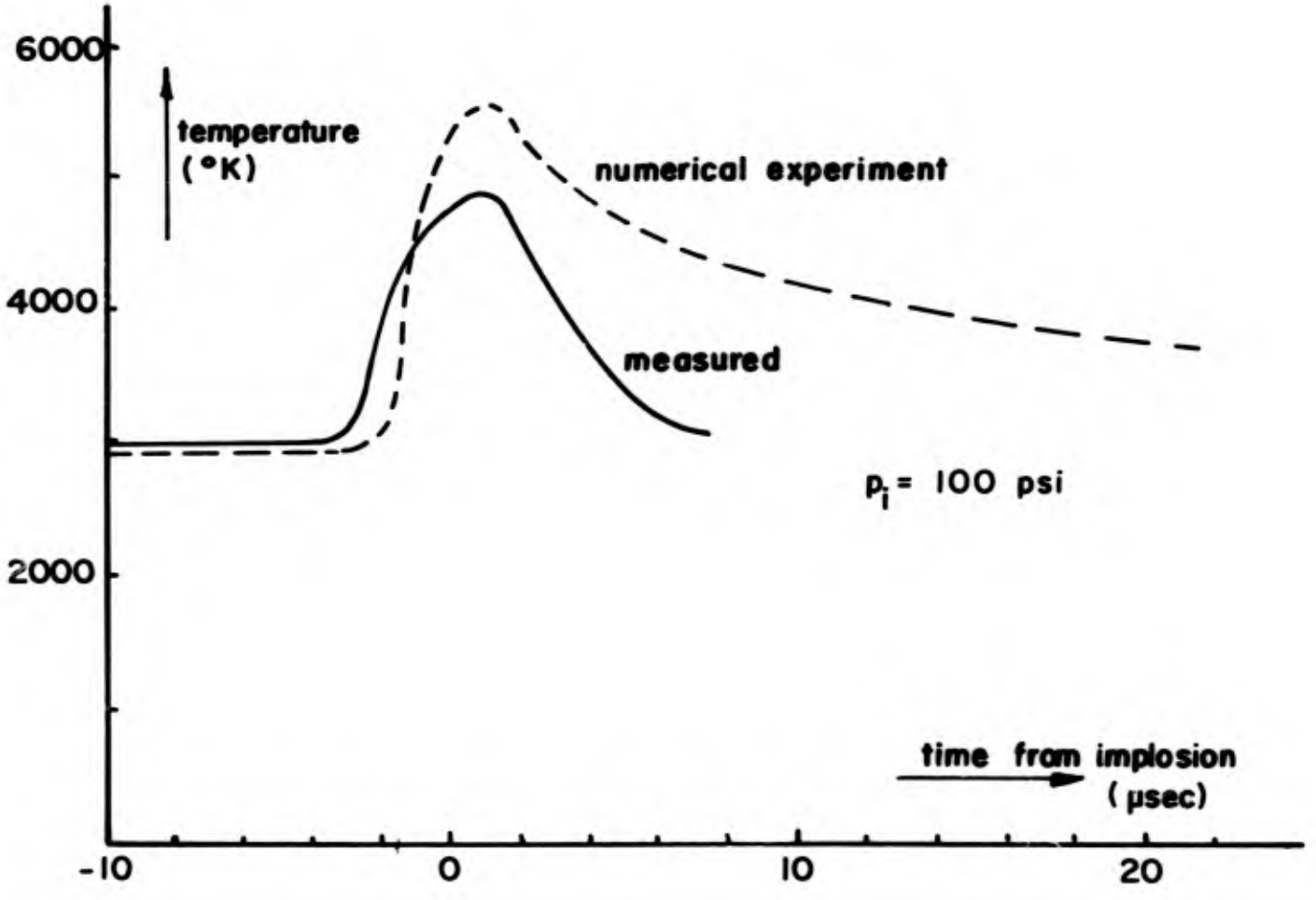

FIGURE 23 COMPARISON BETWEEN MEASURED (REF. 26) AND COMPUTED AVERAGE TEMPERATURES AT THE ORIGIN

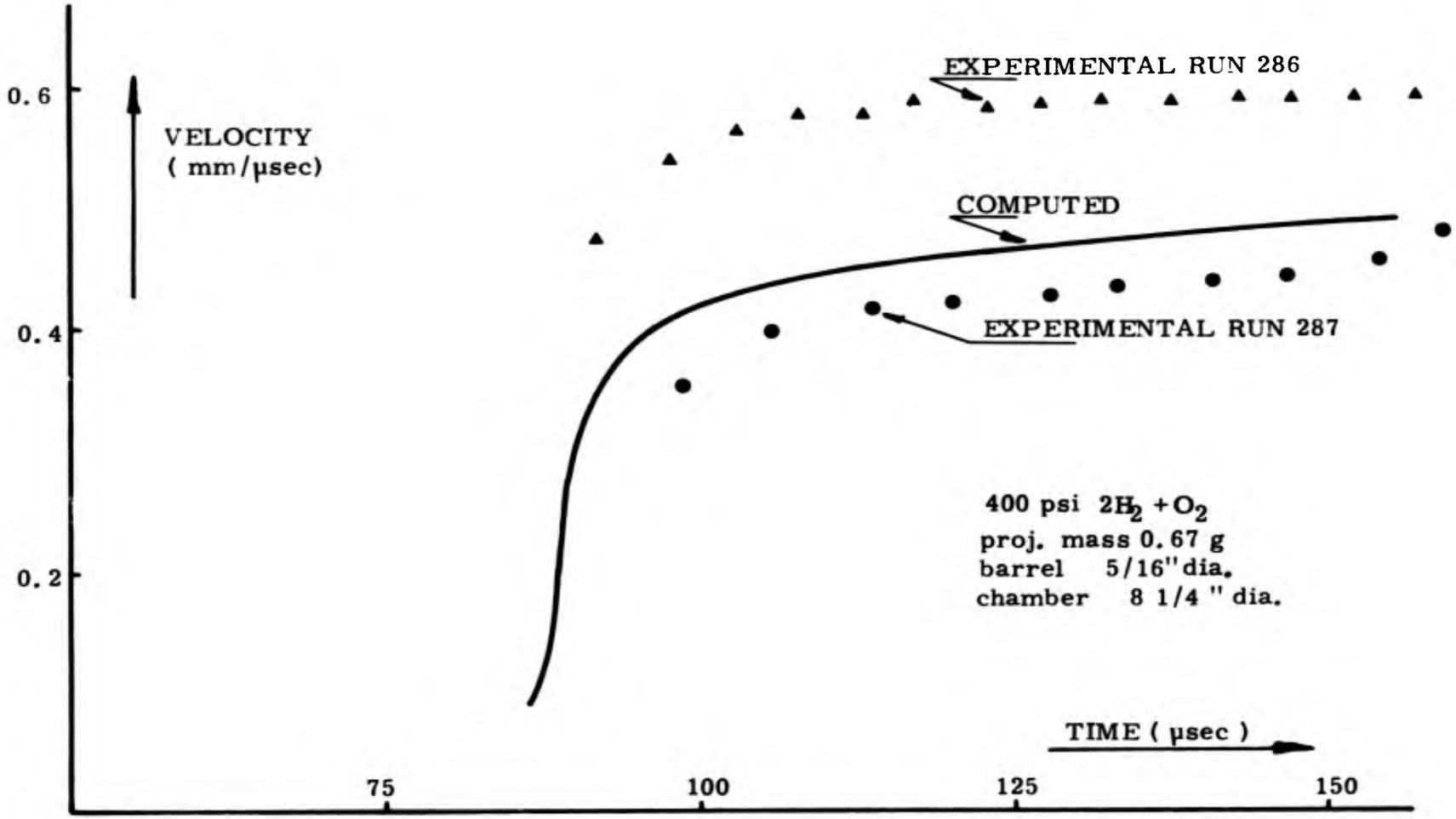

FIG. 24 COMPARISON BETWEEN COMPUTED (REF. 6) AND MEASURED INITIAL VELOCITIES
(400 psi)

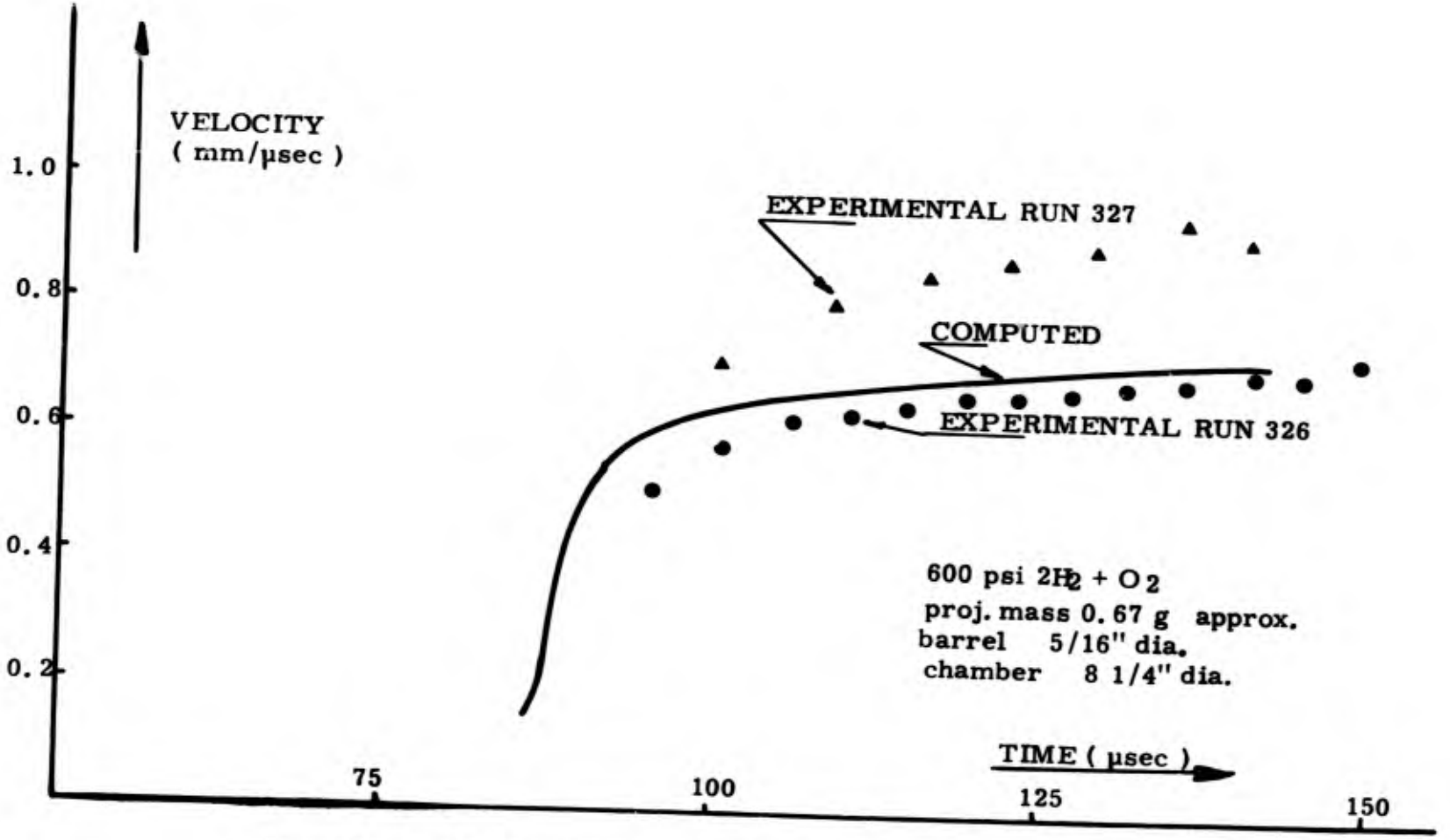

FIG. 25 COMPARISON BETWEEN COMPUTED (REF. 6) AND MEASURED INITIAL VELOCITIES
(600 psi)

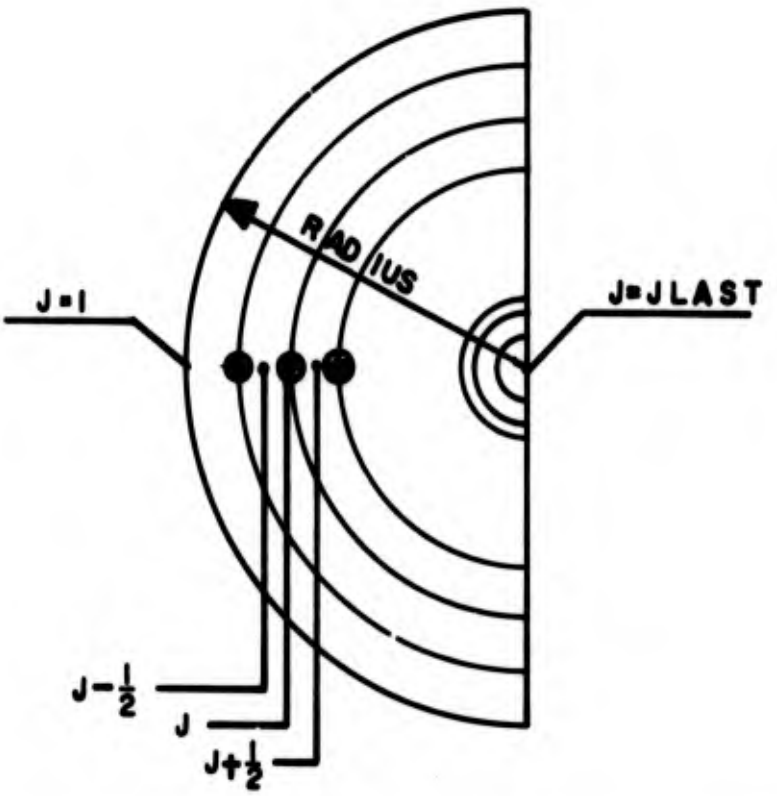

FIGURE A-1 LOCATION OF ZONES AND MASS POINTS IN THE NUMERICAL CALCULATIONS

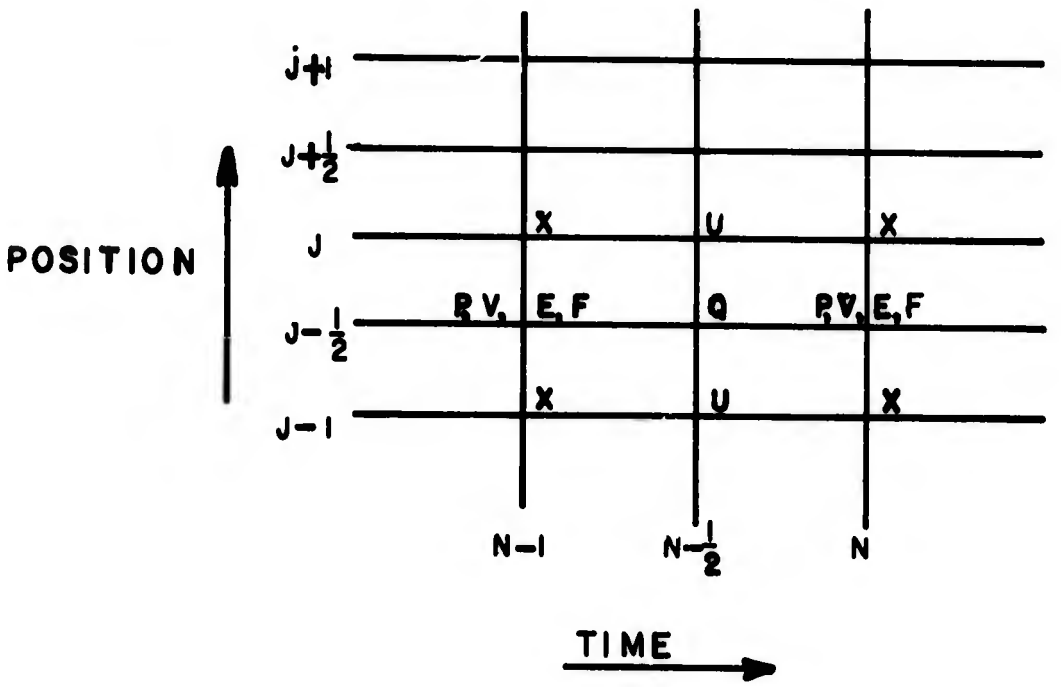

FIGURE A-2 NUMERICAL GRID

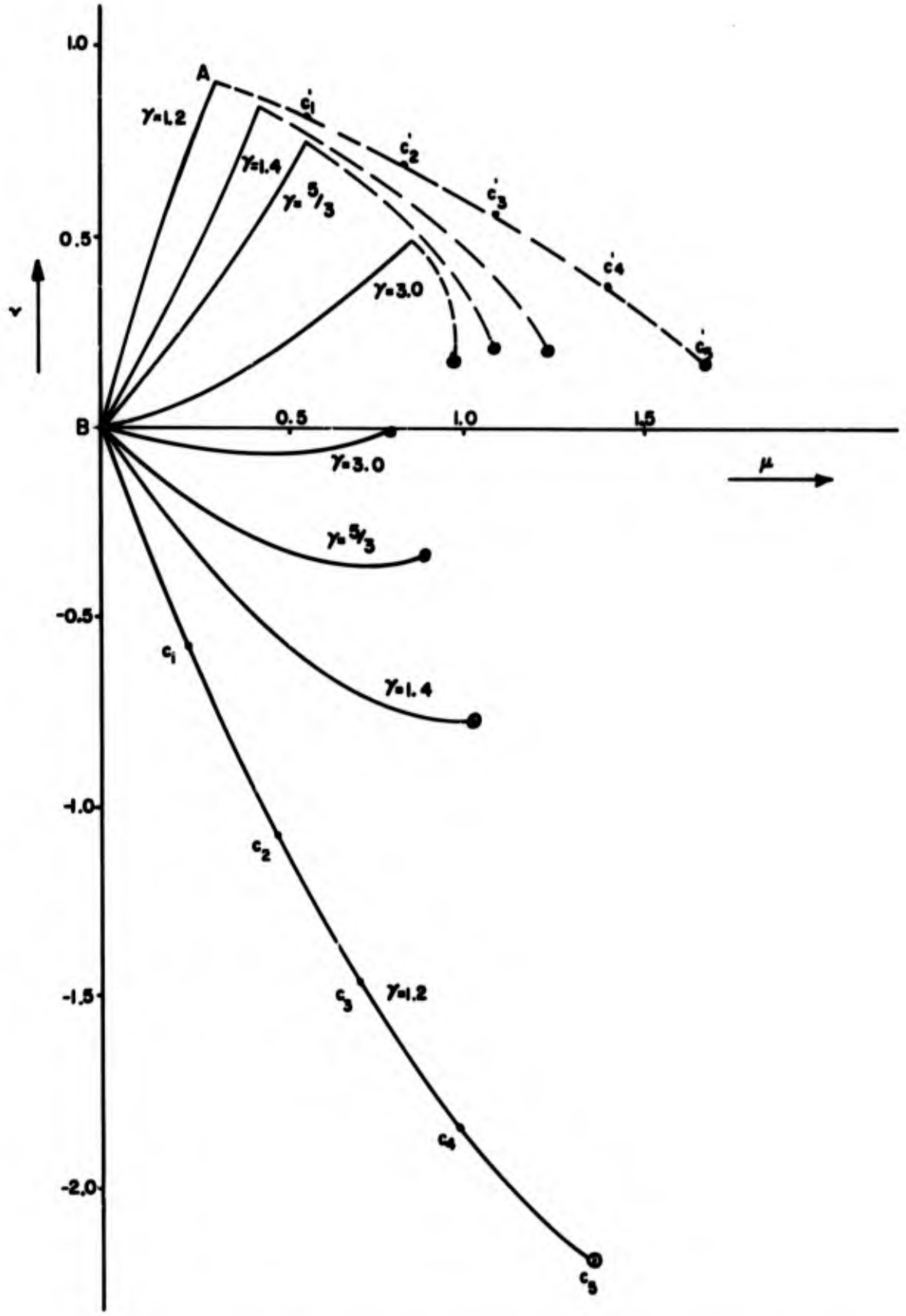

FIGURE D-1 INTEGRAL CURVES FOR THE SPHERICAL SHOCK IN THE μ-ν- PLANE

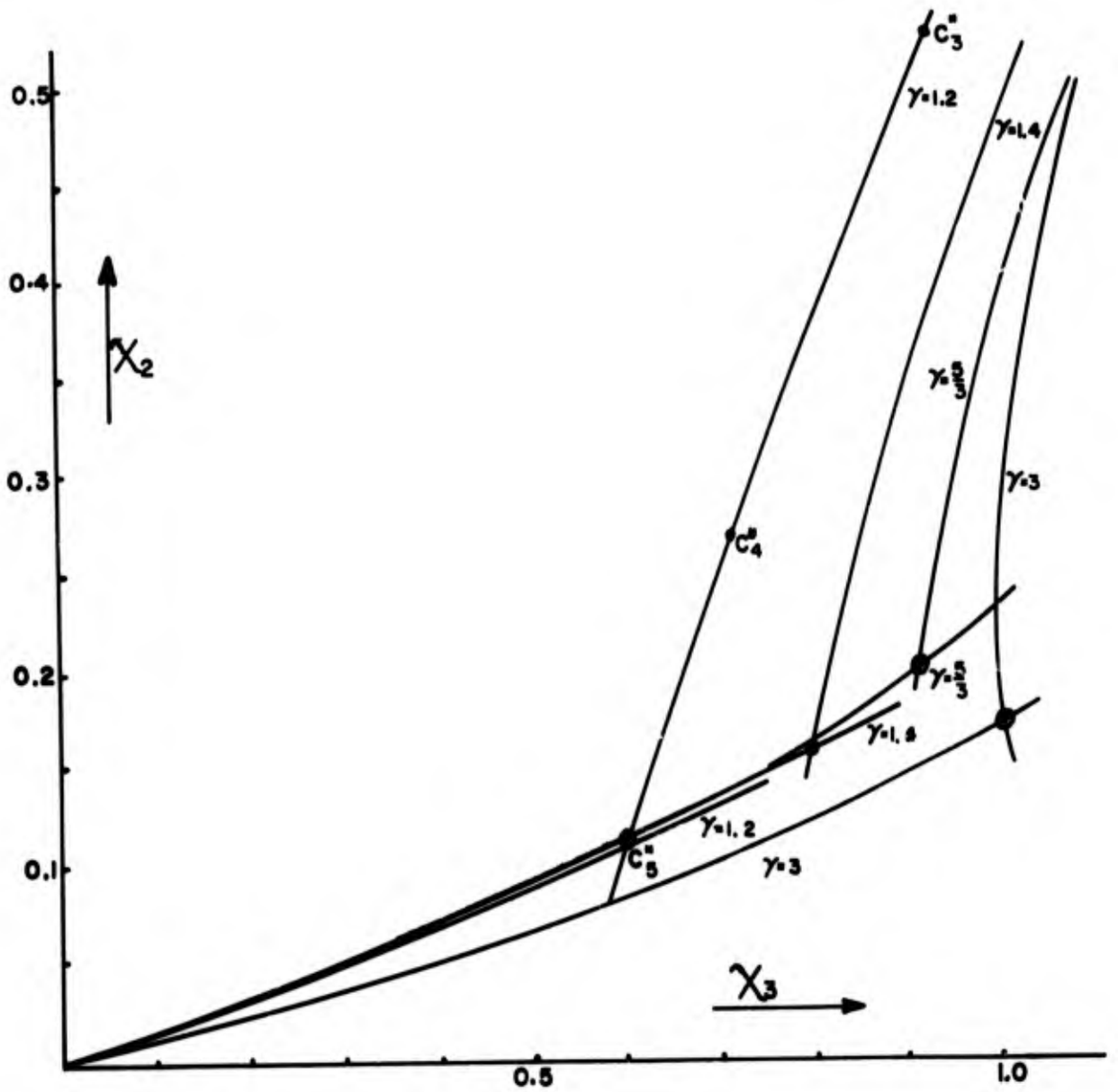

FIGURE D-2 INTEGRAL CURVES FOR THE SPHERICAL SHOCK IN THE χ_2-χ_3-PLANE

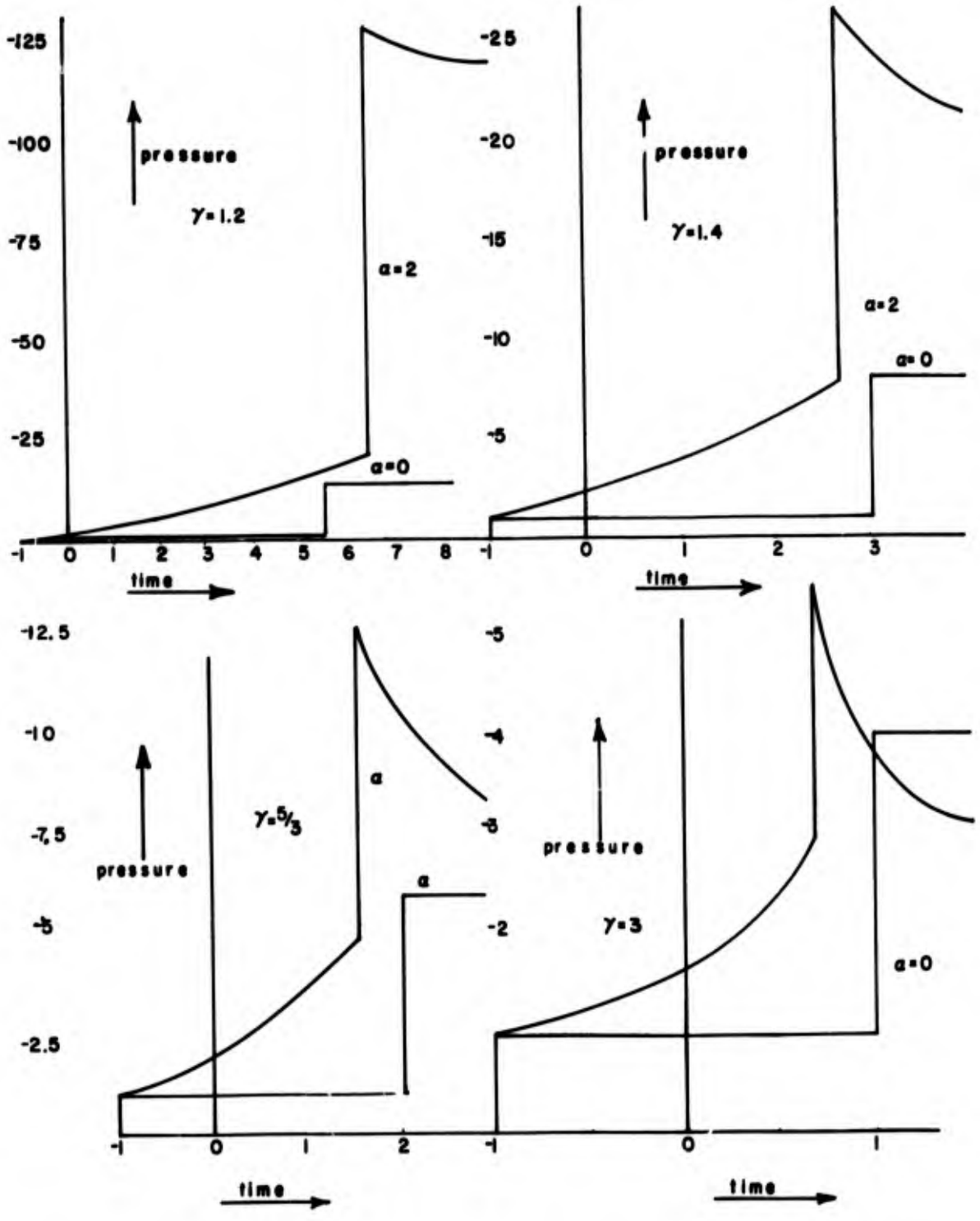

FIGURE D-3 PRESSURE AS FUNCTION OF TIME FOR A SPHERICAL AND PLANAR SHOCK WAVE

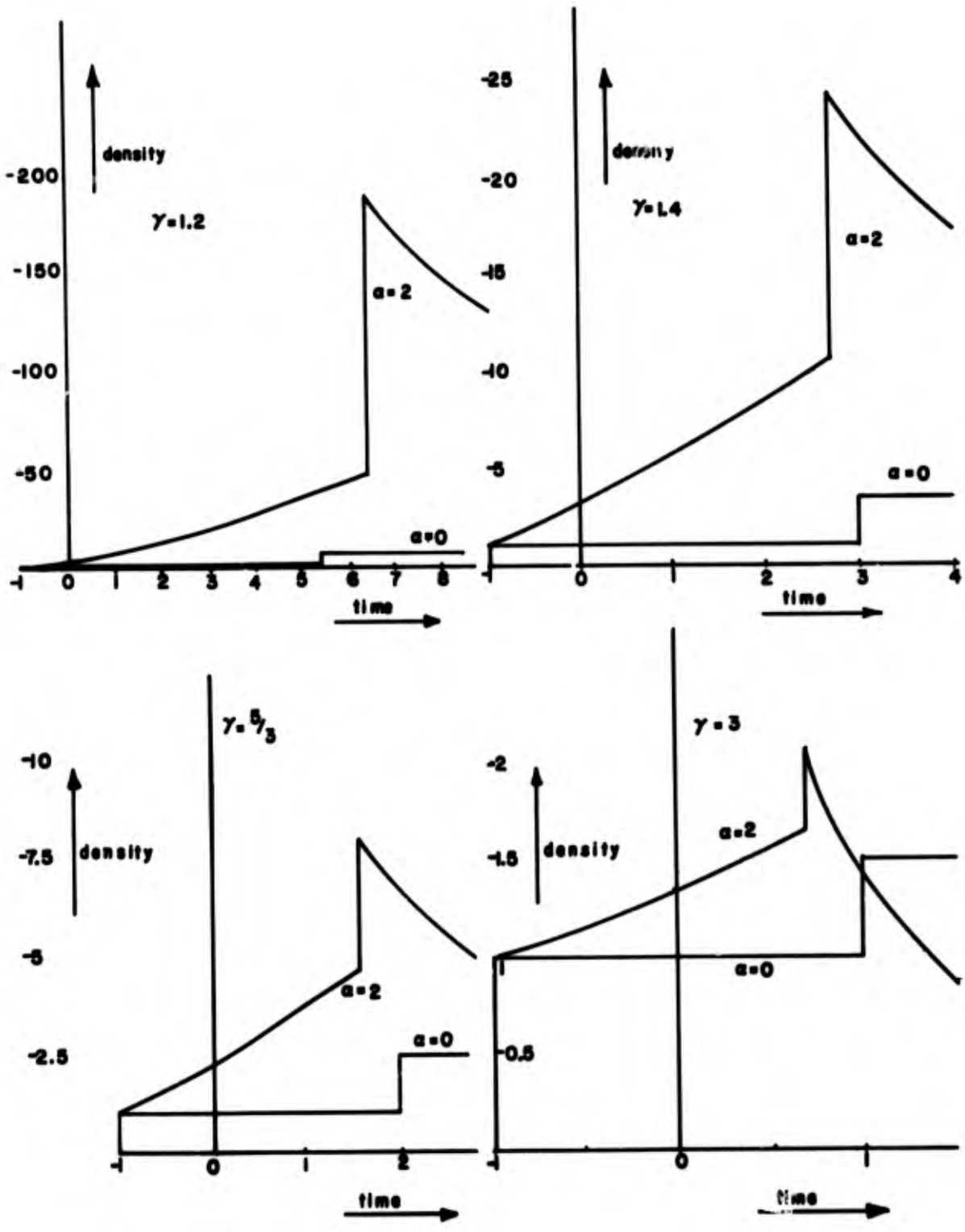

FIGURE D-4 DENSITY AS FUNCTION OF TIME FOR A SPHERICAL AND PLANAR SHOCK WAVE

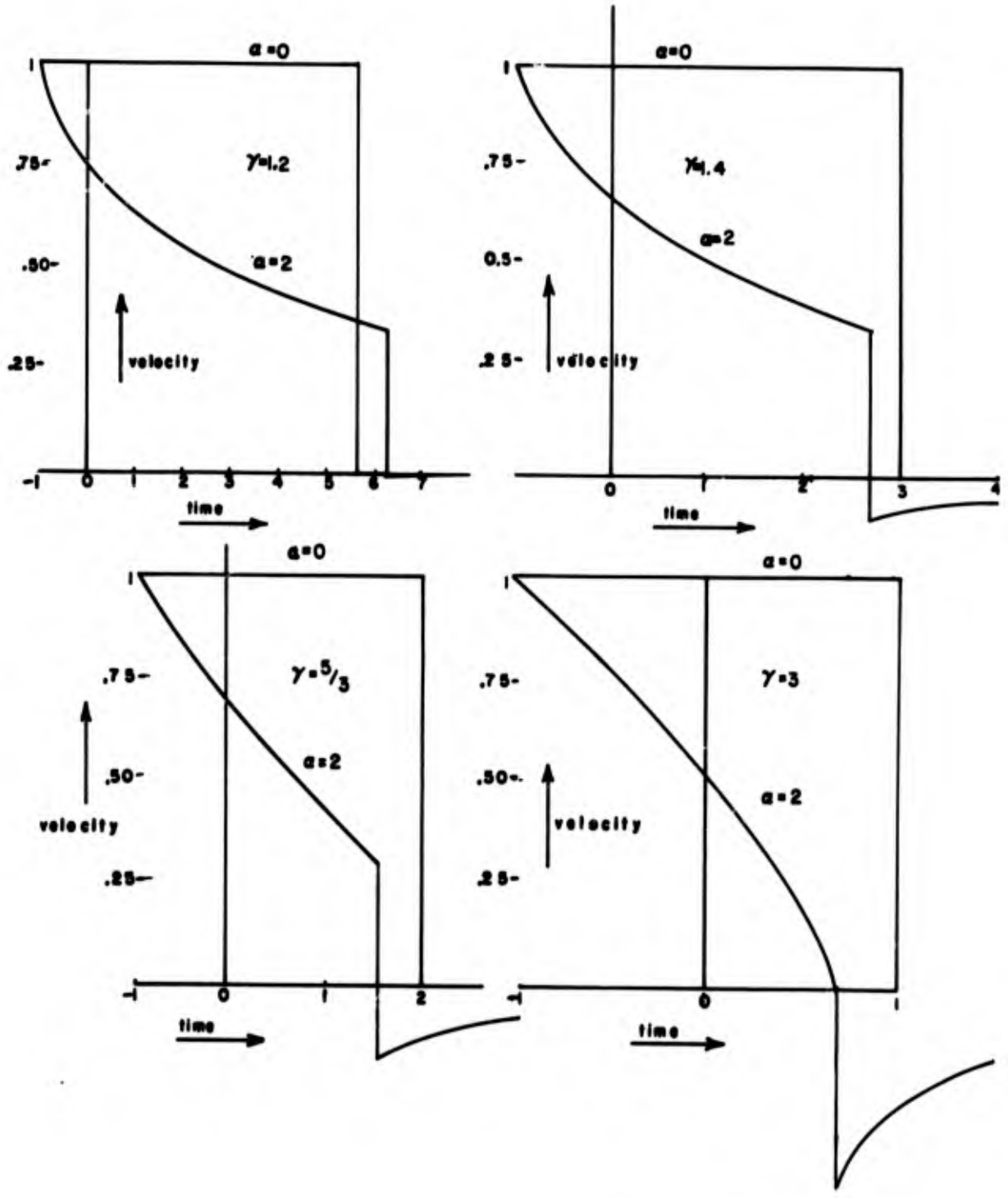

FIGURE D-5 PARTICLE VELOCITY AS FUNCTION OF TIME FOR A SPHERICAL AND PLANAR SHOCK WAVE

LISTING OF THE COMPUTER PROGRAM IN APPENDIX B (9 pages)

```
      COMMON J,JLAST,JLAS1,N,NPLHA,NMNHA,NPLUS,NCYCL,NSTOP,NSTEP,NOUT,
     1NZONE,T,TSTAR,TSTEP,TSTOP,TPROJ,DTPRO,DT1,DT2,PI,RADIU,RBAR,PMASS,
     2XPROJ,UPROJ,ETOT,C,C1,C2,PINIT,PMD,BURNE,ROZER
      COMMON X(99,2),U(99,2),V(99,2),P(99,2),E(99,2),F(99,2),CUBRT(99),
     1Q(99),AREA(99),CSQ(99),HALFM(99),THETA(99),PPLUS(99),T1(99),T2(99)
     2,FORCE(99),TEMP(99)
C                     CONDITIONS FOR THE SET-UP
      N=1
      NMNHA=1
      NPLHA=1
      NCYCL=0
      MSTOP=0
      CALL SETUP
      NPLUS=2
      NPLHA=2
      DT1=0.00005
      DT2=0.00005
      T=0.
      TOUT=TSTAR
      MSTOP=0
C                     START OF THE NEXT CYCLE
  999 T=T+DT1
      NCYCL=NCYCL+1
      MOUT=0
C                     CALCULATION OF NEW POSITIONS AND VELOCITIES
      U(1,NPLHA)=0.
      X(1,NPLUS)=X(1,N)
      CUBRT(1)=RADIU
      AREA(1)=2.*PI*CUBRT(1)**2
      DO 201 J=2,JLAS1
      JMIN1=J-1
      JMNHA=J-1
      JPLHA=J
      DUDT=(PPLUS(JMNHA)-PPLUS(JPLHA))*AREA(J)/(HALFM(JMNHA)+
     1HALFM(JPLHA))
      U(J,NPLHA)=U(J,NMNHA)+DUDT*DT2
      X(J,NPLUS)=X(J,N)+U(J,NPLHA)*DT1
      CUBRT(J)=RADIU-X(J,NPLUS)
      AREA(J)=2.*PI*CUBRT(J)**2
      VOLUM=2.*PI/3.*(CUBRT(JMIN1)**3-CUBRT(J)**3)
      V(JMNHA,NPLUS)=VOLUM*ROZER/2./HALFM(JMNHA)
  201 CONTINUE
      X(JLAST,NPLUS)=RADIU
      U(JLAST,NPLHA)=0.
      CUBRT(JLAST)=0.
      VOLUM=2.*PI/3.*(CUBRT(JLAS1)**3)
      V(JLAS1,NPLUS)=VOLUM*ROZER/HALFM(JLAS1)/2.
C                     CALCULATION OF ARTIFICIAL VISCOSITY
      DO 202 J=2,JLAST
      JMIN1=J-1
      JPLHA=J
      JMNHA=J-1
      IF(U(J,NPLHA)-U(JMIN1,NPLHA)) 203,204,204
  203 IF(BURNE) 250,250,204
  250 VV=0.5*(V(JMNHA,NPLUS)+V(JMNHA,N))
      Q(JMNHA)=C**2*(U(JMIN1,NPLHA)-U(J,NPLHA))**2*ROZER/VV
      GO TO 202
  204 Q(JMNHA)=0.
  202 CONTINUE
      JLAS2=JLAS1-1
      Q(JLAS1)=C1*Q(JLAS1)
```

```
      Q(JLAS2)=C2*Q(JLAS2)
C                     CALCULATION OF PRESSURE AND ENERGY
      CALL STATE
      EINT=0.
      EKIN=0.
      DO 205 J=2,JLAST
      JMNHA=J-1
      JPLHA=J
      EINT=EINT+E(JMNHA,NPLUS)*2.*HALFM(JMNHA)/ROZER
  205 PPLUS(JMNHA)=P(JMNHA,NPLUS)+Q(JMNHA)
      DO 206 J=2,JLAS1
      JMNHA=J-1
      JPLHA=J
  206 EKIN=EKIN+0.5*U(J,NPLHA)**2*(HALFM(JMNHA)+HALFM(JPLHA))
      ETOT=EINT+EKIN
C                     CALCULATION OF ORIGIN CONDITIONS AND PROJECTILE
      CALL PROMO
C                     COMBINED STABILITY CONDITIONS
      TMIN=1.
      DO 207 J=2,JLAST
      JMNHA=J-1
      JMIN1=J-1
      DX=X(J,NPLUS)-X(JMIN1,NPLUS)
      T1(JMNHA)=DX/SQRT(CSQ(JMNHA))
      SV1=V(JMNHA,NPLUS)
      SV2=V(JMNHA,N)
      IF(SV1-SV2) 23,24,24
   23 T2(JMNHA)=(SV1+SV2)*DT1/(4.*C*(SV2-SV1))
      GO TO 25
   24 T2(JMNHA)=1.
   25 TMINR=1./3./SQRT(1./T1(JMNHA)**2+C/T2(JMNHA)**2)
      IF(TMINR-TMIN) 26,207,207
   26 TMIN=TMINR
  207 CONTINUE
      DTOLD=DT1
      DTOL1=DTOLD*1.1
      IF(TMIN-DTOL1) 28,28,29
   28 DT1=TMIN
      GO TO 30
   29 DT1=1.1*DTOLD
   30 DT2=(DT1+DTOLD)/2.
C                     PRINTING OF THE RESULTS
      IF(T-TOUT) 300,301,301
  301 MOUT=1
      TOUT=TSTEP+TOUT
      GO TO 300
  300 IF(NCYCL-NOUT) 302,303,303
  303 MOUT=1
      NOUT=NOUT+NSTEP
      GO TO 302
  302 IF(MOUT-1) 304,305,305
  305 CALL OUT
  304 CONTINUE
C                      TRANSFER TO THE NEXT CYCLE
      NN=N
      N=NPLUS
      NPLUS=NN
      NPLHA=NPLUS
      NMNHA=N
      IF(T-TSTOP) 400,401,401
  401 MSTOP=1
```

```
400 IF(NCYCL-NSTOP) 402,403,403
403 MSTOP=1
402 IF(MSTOP-1) 404,405,405
404 GO TO 999
405 STOP
    END
```

```
      SUBROUTINE SETUP
      COMMON J,JLAST,JLAS1,N,NPLHA,NMNHA,NPLUS,NCYCL,NSTOP,NSTEP,NOUT,
     1NZONE,T,TSTAR,TSTEP,TSTOP,TPROJ,DTPRO,DT1,DT2,PI,RADIU,RBAR,PMASS,
     2XPROJ,UPROJ,ETOT,C,C1,C2,PINIT,PMD,BURNE,ROZER
      COMMON X(99,2),U(99,2),V(99,2),P(99,2),E(99,2),F(99,2),CUBRT(99),
     1Q(99),AREA(99),CSQ(99),HALFM(99),THETA(99),PPLUS(99),T1(99),T2(99)
     2,FORCE(99),TEMP(99)
C                     READING OF INPUT DATA
 2000 FORMAT(3F10.0)
 2001 FORMAT(3I5)
      READ(5,2000) PINIT
      READ(5,2000) RADIU
      READ(5,2001) NZONE
      READ(5,2000) PMD
      READ(5,2000) C
      READ(5,2000) C1,C2
      READ(5,2000) RBAR,PMASS
      READ(5,2000) TPROJ,DTPRO
      READ(5,2000) TSTAR,TSTEP,TSTOP
      READ(5,2001) NOUT,NSTEP,NSTOP
C                     SET-UP OF ZONING AND INITIAL CONDITIONS
      VZERO=1.
      BURNE=1.
      ROZER=12.*PINIT/(14.5*300.*83.70)
      EZERO=1.225*1.E 05*ROZER
      PI=3.14159
      VGAZ=RADIU**3*2./3.*PI
      JLAS1=NZONE
      JLAST=NZONE+1
      VOLA=1.
      DO 100 J=2,JLAS1
  100 VOLA=VOLA+PMD**(J-1)
      X(JLAST,N)=RADIU
      CUBRT(JLAST)=0.
      AREA(JLAST)=0.
      U(1,NMNHA)=0.
      EINIT=0.
      DO 101 J=2,JLAST
      JMNHA=J-1
      JMIN1=J-1
      IF(JMNHA-1) 10,10,11
   10 HALFM(JMNHA)=VGAZ/VOLA*0.5*ROZER
      GO TO 12
   11 HALFM(JMNHA)=VGAZ/VOLA*0.5*ROZER*PMD**(JMNHA-1)
   12 U(J,NMNHA)=0.
      Q(JMNHA)=0.
      V(JMNHA,N)=VZERO
      E(JMNHA,N)=EZERO
      P(JMNHA,N)=0.
      PPLUS(JMNHA)=0.
      F(JMNHA,N)=0.
  101 CONTINUE
      DO 102 J=2,JLAST
      JJ=JLAST-J+1
      JJP1=JJ+1
      VOLUM=2.*HALFM(JJ)/ROZER
      CJ=3./2./PI*VOLUM+CUBRT(JJP1)**3
      Y1=1.
   13 Y2=Y1-(Y1**3-CJ)/(3.*Y1**2)
      IF(ABS((Y1-Y2)/Y2)-1.E-04) 14,14,15
   15 Y1=Y2
```

```
      GO TO 13
   14 CUBRT(JJ)=Y2
      X(JJ,N)=RADIU-CUBRT(JJ)
      AREA(JJ)=2.*PI*CUBRT(JJ)**2
  102 CONTINUE
      TMASS=0.
      DO 103 J=2,JLAST
      JMNHA=J-1
      TMASS=TMASS+2.*HALFM(JMNHA)
  103 EINIT=EINIT+E(JMNHA,N)*2.*HALFM(JMNHA)/ROZER
      UPROJ=0.
      XPROJ=0.
C                     OUTPUT OF  INITIAL CONDITIONS
 1000 FORMAT(1H1)
 1001 FORMAT(2X,18HINITIAL CONDITIONS)
 1002 FORMAT(1H0)
 1003 FORMAT(2X,47H   N  PINIT   RADIU PMD  C    RAD  M    C1    C2)
 1004 FORMAT(2X,I5,2F7.2,6F5.2)
 1005 FORMAT(2X,15HINITIAL ENERGY=,E13.5)
 1006 FORMAT(2X,65H J    R        U       RHO      P        Q        F
     1  E      MASS)
 1007 FORMAT(I3,7F8.3,F8.5)
      WRITE(6,1000)
      WRITE(6,1001)
      WRITE(6,1002)
      WRITE(6,1003)
      WRITE(6,1004)  NZONE,PINIT,RADIU,PMD,C,RBAR,PMASS,C1,C2
      WRITE(6,1002)
      WRITE(6,1005) EINIT
      WRITE(6,1002)
      WRITE(6,1006)
      WRITE(6,1002)
      JR=0
      CUOUT=CUBRT(1)
      UOUT=U(1,N)
      WRITE(6,1007) JR,CUOUT,UOUT
      DO 1100 J=2,JLAST
      JMIN1=J-1
      JMNHA=J-1
      CUOUT=0.5*(CUBRT(JMIN1)+CUBRT(J))
      UOUT=0.5*(U(JMIN1,NMNHA)+U(J,NMNHA))
      VOUT=1./V(JMNHA,N)
      EOUT=E(JMNHA,N)*2.*HALFM(JMNHA)/EINIT/ROZER
      RMOUT=3.*2.*HALFM(JMNHA)/(VGAZ*2.*PI*ROZER)
      WRITE(6,1007) JMIN1,CUOUT,UOUT,VOUT,P(JMNHA,N),Q(JMNHA),
     1F(JMNHA,N),EOUT,RMOUT
 1100 CONTINUE
      WRITE(6,1007) JLAST,CUBRT(JLAST),U(JLAST,NMNHA)
      WRITE(6,1000)
      RETURN
      END
```

```
      SUBROUTINE STATE
      COMMON J,JLAST,JLAS1,N,NPLHA,NMNHA,NPLUS,NCYCL,NSTOP,NSTEP,NOUT,
     1NZONE,T,TSTAR,TSTEP,TSTOP,TPROJ,DTPRO,DT1,DT2,PI,RADIU,RBAR,PMASS,
     2XPROJ,UPROJ,ETOT,C,C1,C2,PINIT,PMD,BURNE,ROZER
      COMMON X(99,2),U(99,2),V(99,2),P(99,2),E(99,2),F(99,2),CUBRT(99),
     1Q(99),AREA(99),CSQ(99),HALFM(99),THETA(99),PPLUS(99),T1(99),T2(99)
     2,FORCE(99),TEMP(99)
C                    DETERMINATION OF F
      IF(BURNE) 100,100,101
  101 FMIN=2.
      F(JLAS1,NPLUS)=0.999
      DO 102 J=2,JLAS1
      JMNHA=J-1
      F(JMNHA,NPLUS)=(1.-V(JMNHA,NPLUS))/0.46
      IF(F(JMNHA,NPLUS)-0.01) 103,104,104
  103 F(JMNHA,NPLUS)=0.
  104 IF(F(JMNHA,NPLUS)-1.) 105,106,107
  105 IF(F(JMNHA,NPLUS)-F(JMNHA,N)) 107,106,106
  107 F(JMNHA,NPLUS)=1.
  106 IF(F(JMNHA,NPLUS)-FMIN) 108,108,102
  108 FMIN=F(JMNHA,NPLUS)
  102 CONTINUE
  109 IF(FMIN-1.) 100,110,110
  110 DO 111 J=2,JLAST
      JMNHA=J-1
      F(JMNHA,N)=1.
      F(JMNHA,NPLUS)=1.
  111 BURNE=0.
  100 CONTINUE
C                    EQUATION OF STATE AND ENERGYEQUATION
      DO 200 J=2,JLAST
      JMNHA=J-1
      IF(F(JMNHA,NPLUS)) 6,6,7
    6 P(JMNHA,NPLUS)=0.
      E(JMNHA,NPLUS)=E(JMNHA,N)
      GO TO 21
    7 E1=(E(JMNHA,N)-((P(JMNHA,N)+Q(JMNHA))*(V(JMNHA,NPLUS)-V(JMNHA,N))
     1))/ROZER/10000.
      VE=V(JMNHA,NPLUS)/ROZER
      NE=0
      IF(F(JMNHA,NPLUS)-1.) 8,9,9
    8 P1=10.
      GO TO 10
    9 P1=P(JMNHA,N)/10000.
   10 P1VE=P1*VE
      P1VE2=P1VE**2
      P1VE4=P1VE2**2
      P1VE5=P1VE*P1VE4
      BRAC1=1140.+P1VE4
      BRAC2=.101E-03*ALOG(ABS(P1/1.013E-03 ))-.2325E-03
      IF(P1VE-1.0465) 11,11,12
   11 ALPHA=0.
      DALFD=0.
      DALFV=0.
      GO TO 15
   12 IF(P1VE-3.488) 13,13,14
   13 ALPHA=8600.*P1VE-9000.
      DALFD=8600.*VE
      DALDV=8600.*P1
      GO TO 15
   14 ALPHA=21.E03
```

```
      DALFD=0.
      DALFV=0.
   15 EF=6.57*P1VE+974.*P1VE2/BRAC1-ALPHA*BRAC2-E1
      EPRIM=6.57*VE+1948.*VE**2*P1/BRAC1-3896.*VE*P1VE5/BRAC1**2-DALFD*
     1BRAC2-ALPHA*0.101E-03/P1
      PNEW=P1-EF/EPRIM
      IF(ABS(PNEW-P1)-0.0001) 17,17,16
   16 P1=PNEW
      GO TO 10
   17 IF(NE) 18,18,19
   18 E1=E1-(.5*(P1*10000.*F(JMNHA,NPLUS)-P(JMNHA,N))*(V(JMNHA,NPLUS)-
     1V(JMNHA,N)))/10000./ROZER
      NE=1
      GO TO 10
   19 E(JMNHA,NPLUS)=E1*10000.*ROZER
      P(JMNHA,NPLUS)=P1*10000.*F(JMNHA,NPLUS)
      DEDP=EPRIM
      DEDV=6.57*P1+1948.*P1VE*P1/BRAC1-3896.*P1VE5*P1/BRAC1**2-DALFV*
     1BRAC2
      IF(F(JMNHA,NPLUS)) 20,21,20
   21 CSQ(JMNHA)=1.
      THETA(JMNHA)=P(JMNHA,NPLUS)*V(JMNHA,NPLUS)/85./ROZER*12.
      GO TO 200
   20 CSQ(JMNHA)=(V(JMNHA,NPLUS)/ROZER)**2*(P1+DEDV)/DEDP*10000.
      THETA(JMNHA)=P(JMNHA,NPLUS)*V(JMNHA,NPLUS)/85./ROZER*12.
  200 CONTINUE
      RETURN
      END
```

```
      SUBROUTINE PROMO
      COMMON J,JLAST,JLAS1,N,NPLHA,NMNHA,NPLUS,NCYCL,NSTOP,NSTEP,NOUT,
     1NZONE,T,TSTAR,TSTEP,TSTOP,TPROJ,DTPRO,DT1,DT2,PI,RADIU,RBAR,PMASS,
     2XPROJ,UPROJ,ETOT,C,C1,C2,PINIT,PMD,BURNE,ROZER
      COMMON X(99,2),U(99,2),V(99,2),P(99,2),E(99,2),F(99,2),CUBRT(99),
     1Q(99),AREA(99),CSQ(99),HALFM(99),THETA(99),PPLUS(99),T1(99),T2(99)
     2,FORCE(99),TEMP(99)
1000  FORMAT(15X,F8.4,F8.1,F8.4,F8.1,5X,I2,2F8.1,F8.3,F8.4,F8.2)
      FPROJ=0.
      TEMP1=0.
      DO 15 J=2,JLAST
      JMNHA=J-1
      JMIN1=J-1
      IF(CUBRT(J)-RBAR) 10,10,11
   11 FORCE(JMNHA)=0.
      TEMP(JMNHA)=0.
      GO TO 14
   10 IF(CUBRT(JMIN1)-RBAR) 13,13,12
   12 NORIG=NZONE-J+2
      FORCE(JMNHA)=PI*(RBAR**2-CUBRT(J)**2)*PPLUS(JMNHA)
      TEMP(JMNHA)=PI*THETA(JMNHA)*(RBAR**2-CUBRT(J)**2)
      GO TO 14
   13 FORCE(JMNHA)=PI*(CUBRT(JMIN1)**2-CUBRT(J)**2)*PPLUS(JMNHA)
      TEMP(JMNHA)=PI*THETA(JMNHA)*(CUBRT(JMIN1)**2-CUBRT(J)**2)
   14 FPROJ=FPROJ+FORCE(JMNHA)
      TEMP1=TEMP1+TEMP(JMNHA)
   15 CONTINUE
      APROJ=FPROJ/PMASS
      UPROJ=UPROJ+APROJ*DT2
      XPROJ=XPROJ+UPROJ*DT1
      PAOUT=FPROJ/(PI*RBAR**2)
      VOUT=1./V(JLAS1,NPLUS)
      ATEMP=TEMP1/(PI*RBAR**2)
      IF(T-TPROJ) 20,21,21
   21 TPROJ=TPROJ+DTPRO
      WRITE(6,1000) T,PPLUS(JLAS1),VOUT,THETA(JLAS1),NORIG,PAOUT,ATEMP,
     1XPROJ,UPROJ,APROJ
   20 RETURN
      END
```

```
      SUBROUTINE OUT
      COMMON J,JLAST,JLAS1,N,NPLHA,NMNHA,NPLUS,NCYCL,NSTOP,NSTEP,NOUT,
     1NZONE,T,TSTAR,TSTEP,TSTOP,TPROJ,DTPRO,DT1,DT2,PI,RADIU,RBAR,PMASS,
     2XPROJ,UPROJ,ETOT,C,C1,C2,PINIT,PMD,BURNE,ROZER
      COMMON X(99,2),U(99,2),V(99,2),P(99,2),E(99,2),F(99,2),CUBRT(99),
     1Q(99),AREA(99),CSQ(99),HALFM(99),THETA(99),PPLUS(99),T1(99),T2(99)
     2,FORCE(99),TEMP(99)
1000  FORMAT(1H1)
1001  FORMAT(2X,5HCYCLE,I5,6H TIME=,F10.6,10HTIME-STEP=,F10.6,3X,7HENERG
     1Y=,E13.5)
1002  FORMAT(1H0)
1003  FORMAT(2X,83H J     X         U        RHO        P         Q         F
     1 E        TEMP    SOUND SP.        )
1004  FORMAT(I3,2F8.2,F8.4,2F8.1,F8.4,F8.5,2F8.2)
1005  FORMAT(17X,32H    T         P        RHO       TEMP   ,3X,42HNO    PBASE
     1TBASE    POS      VEL     ACCEL )
      WRITE(6,1002)
      WRITE(6,1001) NCYCL,T,DT1,ETOT
      WRITE(6,1002)
      WRITE(6,1003)
      WRITE(6,1002)
      JR=0
      CUOUT=CUBRT(1)
      UOUT=U(1,NPLHA)
      WRITE(6,1004) JR,CUOUT,UOUT
      DO 1100 J=2,JLAST
      JMNHA=J-1
      JMIN1=J-1
      CUOUT=(CUBRT(JMIN1)+CUBRT(J))*0.5
      UOUT=(U(JMIN1,NPLHA)+U(J,NPLHA))*0.5
      VOUT=1./V(JMNHA,NPLUS)
      POUT=PPLUS(JMNHA)
      QOUT=Q(JMNHA)
      FOUT=F(JMNHA,NPLUS)
      EOUT=(E(JMNHA,NPLUS)*2.*HALFM(JMNHA)/ROZER+0.5*HALFM(JMNHA)*(0.5*
     1(U(JMIN1,NPLHA)+U(J,NPLHA)))**2)/ETOT
      TEOUT=THETA(JMNHA)
      SOUT=SQRT(CSQ(JMNHA))
1100  WRITE(6,1004) JMIN1,CUOUT,UOUT,VOUT,POUT,QOUT,FOUT,EOUT,TEOUT,SOUT
      J=JLAST
      CUOUT=CUBRT(JLAST)
      UOUT=U(JLAST,NPLHA)
      WRITE(6,1004) J,CUOUT,UOUT
      WRITE(6,1002)
      WRITE(6,1002)
      WRITE(6,1005)
      RETURN
      END
```

UNCLASSIFIED
Security Classification

DOCUMENT CONTROL DATA - R & D

(Security classification of title, body of abstract and indexing annotation must be entered when the overall report is classified)

1. ORIGINATING ACTIVITY *(Corporate author)*
Institute for Aerospace Studies
University of Toronto
Toronto, Canada

2a. REPORT SECURITY CLASSIFICATION
Unclassified

2b. GROUP

3. REPORT TITLE
A NUMERICAL MODEL FOR A COMBUSTION-DRIVEN SPHERICAL IMPLOSION WAVE

4. DESCRIPTIVE NOTES *(Type of report and inclusive dates)*
Scientific. Interim.

5. AUTHOR(S) *(First name, middle initial, last name)*
A. Elsenaar

6. REPORT DATE	7a. TOTAL NO. OF PAGES	7b. NO. OF REFS
April 1970	89	30

8a. CONTRACT OR GRANT NO.
AF 33(615)-5313

b. PROJECT NO.
7065

c. DOD Element 61102F

d. DOD Sub-element 681307

9a. ORIGINATOR'S REPORT NUMBER(S)
UTIAS Technical Note No. 144

9b. OTHER REPORT NO(S) *(Any other numbers that may be assigned this report)*
ARL 70-0074

10. DISTRIBUTION STATEMENT
This document has been approved for public release and sale; its distribution is unlimited.

11. SUPPLEMENTARY NOTES
TECH OTHER

12. SPONSORING MILITARY ACTIVITY
Aerospace Research Laboratories
ARL (ARF)
Wright-Patterson AFB, Ohio 45433

13. ABSTRACT
A study is made of a combustion-driven spherical implosion wave inside a hemispherical cavity, using a finite difference method to integrate the one-dimensional Lagrangian gasdynamic equations, combined with an artificial pressure term to represent the shocks and a realistic equation of state for the stoichiometric hydrogen-oxygen mixture. The application of this technique is studied in some detail.

DD FORM 1 NOV 65 1473

UNCLASSIFIED
Security Classification

14. KEY WORDS	LINK A		LINK B		LINK C	
	ROLE	WT	ROLE	WT	ROLE	WT
Implosions Numerical Techniques Hypervelocity Launchers						